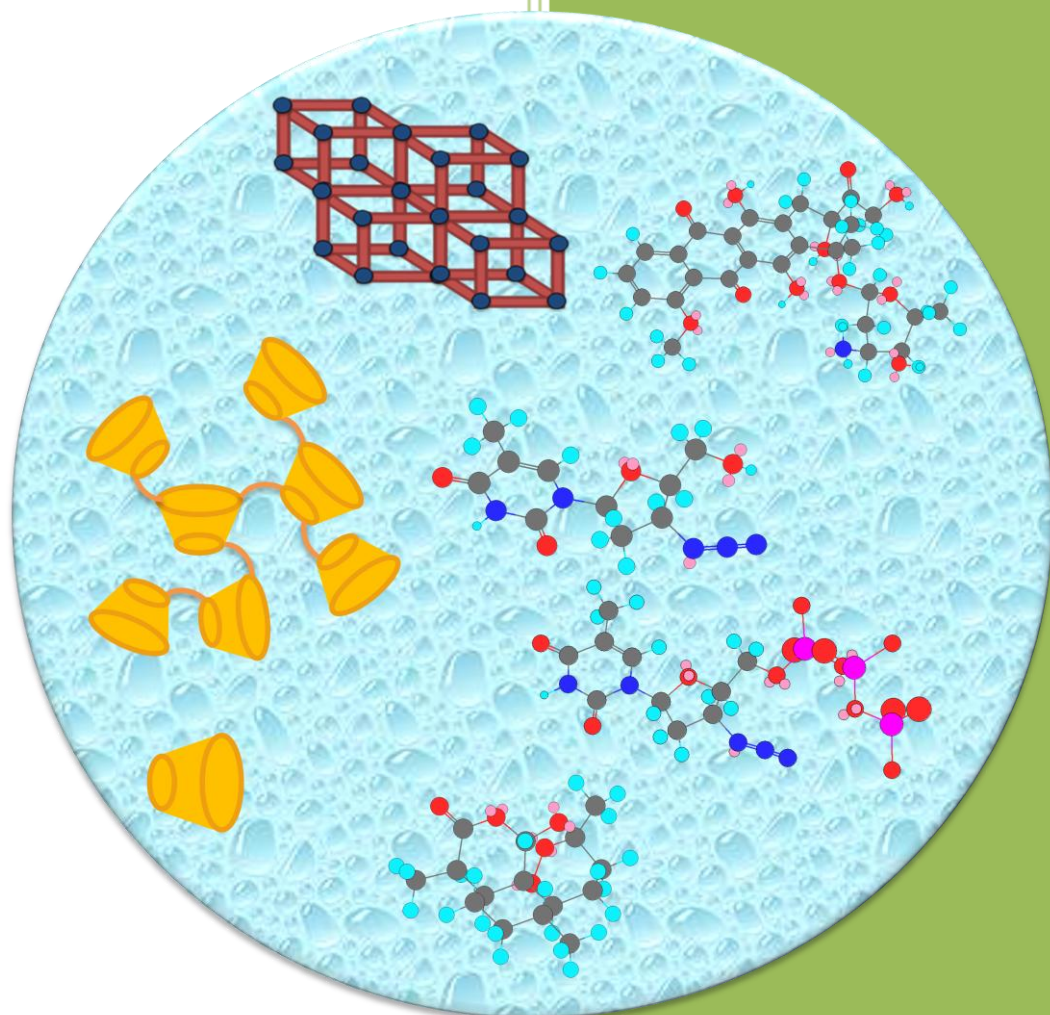# Spectroscopic studies on Cyclodextrin and Metal Organic Framework based potential nanovectors for delivery of Anticancer and Antiviral drugs

Resmi Anand

Alma Mater Studiorum – Università di Bologna

DOTTORATO DI RICERCA IN

Scienze Chimiche

Ciclo XXV

Settore Concorsuale di afferenza: 03/A2 MODELLI E METODOLOGIE PER LE SCIENZE CHIMICA

Settore Scientifico disciplinare: CHIM/02 CHIMICA FISICA

SPECTROSCOPIC STUDIES ON CYCLODEXTRIN AND METAL ORGANIC FRAMEWORK BASED POTENTIAL NANOVECTORS FOR DELIVERY OF ANTICANCER AND ANTIVIRAL DRUGS

Presentata da: Resmi ANAND

Coordinatore Dottorato	**Relatore**
Prof. Adriana Bigi	**Dr. Luca Prodi**
	Correlatore
	Dr. Sandra Monti

Esame finale anno 2013

Zamboni, Roberta Chiodini and Illaria Giuliodori for their assistance and unparallel support in managing official things.

I give my special thanks to John Mohanraj, who was a friend in need and a friend indeed. I thank him for his support and encouragement during my research time.

Thanks to Adina Ciuciu, who has been maintaining a friendly atmosphere in my working environment and also to Filipo Monti, Dr. Yoosaf Karuvath, Joanna Malicka, Eleanora Pavoni, Maria-Pia and Dr. Praveen Vakayil Karthikeyan for their friendship and support.

Thanks to Nadia, Nadege, Zoltan, Ahmet, friends I own from Paris, for their extraordinary care and concern, which turned my stay in France as a pleasant and a memorable one.

A special thanks to the CYCLON team, Dr. Konstantina Yannakopoulou, Prof. Thorsteinn Loftsson, Prof. Salvatore Sortino, Prof. Abderrazzak Douhal, Prof. Marica B. Ericsson, Noufal, Vladimir, Ricardo, Aurore, Linda, Maria who have been supporting me always and have provided a platform to gain experience in presenting scientific results and discussions.

I immensely thank all my teachers, who have transferred their valuable knowledge. Special thanks go to Dr. Jaya Kannan who inspired me to take the research as my carrier and also for his fundamental lessons on research activities.

Last but not least, my special thanks go to my beloved husband, Anand, for allowing me to pursue research even after my marriage that too in Europe. Without his love, concern and support, for sure, these 3 years would have been so difficult to me. I owe him a lot throughout my life. I'm also in debted to my beloved parents and my sister who have been assisting, supporting, and caring me all through these years. It is their love and support that encouraged me to overcome many difficulties during my research period.

Resmi Anand

Table of Contents

ABSTRACT

The aim of this dissertation work is the development of new multifunctional nanocarriers for the enhanced encapsulation and delivery of several anticancer and antiviral drugs. The work focused mainly on water soluble and biocompatible oligosaccharides, the cyclodextrins (CyDs), and a new family of biodegradable nanocarriers made of porous metal-organic frameworks (nanoMOFs) and studied their interaction with several antitumoral agents with various spectroscopic techniques and analysis of association equilibria. The entire thesis is divided into 6 chapters based on the types of carriers and drugs. The content of each chapter is briefly described below.

In **Chapter 1**, as general introduction the main drug carrier systems (DDS), such as polymers, micelles, liposomes, cyclodextrins, metal organic frameworks etc, are briefly overviewed. Following this, a short description about the scope of this thesis work is given.

Chapter 2 is divided into four sections. The first section describes the self-aggreagation and associated pharmacological drawback of the anticancer drug, doxorubicin. Development of carriers able to inhibit self-association is of great relevance to drug delivery optimization. The subsequent sections describe the binding modes of DOX to biocompatible CyD derivatives, showing that β-cyclodextrin polymeric nanoparticles are able to inhibit drug dimerization, whereas the natural β-CyD does not provide very stable complexes and the natural γ–cyclodextrin is unable to disrupt the DOX dimer (collaboration with Dr. Ruxandra Gref, UMR-CNRS, France and with Dr. Stefano Ottani, ISOF-CNR, Bologna). A citric acid crosslinked γ–cyclodextrin polymer, revealed to be very promising, because it is able to form very stable complexes as well as disrupt the doxorubicin dimer (collaboration with Dr. Milo Malanga, CYCLOLAB, Budapest and Prof. Vargas-Berenguel, Univ of Almeria, Spain and Dr. Ruxandra Gref, UMR-CNRS, France).

The studies of metal organic frameworks (MOFs) for biological application is a new field for MOF researchers and recent reports in this area reveal these materials can be very promising as a novel platform for drug delivery applications. In **Chapter 3** the non-covalent interaction with MOF nanoparticles based on iron(III)-trimesate is examined for a series of anticancer and antiviral drugs (Doxorubicin (DOX), 3'-Azido-3'-deoxythymidine (AZT), 3'-Azido-3'-deoxy-thymidine-5'-monophosphate (AZTMP), 3´-Azido-3´- deoxythymidine-5´- triphosphate (AZTTP)) with nanoMOF (collaboration with Dr. Ruxandra Gref, UMR-CNRS, France). The nanoMOF systems were also size separated and characterized by using asymmetric flow filed flow fractionation with multi angle

light scattering (AF4-MALS) technique (collaboration with Prof. P. Reschiglian, Univ. of Bologna). The results of in depth physico-chemical studies on all these systems, involving UV visible absorption, circular dichroism, fluorescence spectroscopies and binding analysis, are presented. It has been established that the interaction of DOX and nanoMOFs is through coordination of dihydroxyanthraquinone deprotonated hydroxyl groups to Fe centers in the pores. Doxorubicin fluorescence is completely quenched in the MOF complex. The spectroscopic study indicates a very weak interaction between AZT and MOF. On the contrary the phosphorilated azidothymidine derivatives show that both the azidothymidine and the phosphate moieties can be involved in the binding to the MOF frame, with the phosphate coordination predominating in the binding of AZTTP. These results allow to envisage this highly versatile and "green" carrier system can be applied to delivery other anti-cancer and anti-viral phosphorylated nucleosides analogues.

Chapter 4 describes the interaction of an important antimalarial drug, artemisinin, with two cyclodextrin-based carriers. This drug is the parent molecule of the most effective class of drugs, nowadays in the clinical practice against multidrug resistant forms of *Plasmodium falciparum*. Scarce solubility in aqueous medium, resulting in poor absorption upon oral administration, is a serious drawback for the use of ART. Cyclodextrins proved to be potentially useful also for ART delivery. It has been shown that the $\beta-$cyclodextrin polymer (pβ-CyD) is able to improve the water solubility of ART by associating it to the β-cyclodextrin cavities embedded within the nanoparticle polymeric frame. Further, a light responsive bis(β-CyD) host with an azobenzene 6-6' linker has been shown to possess a binding affinity controllable by light for ART as guest. This model system let to envisage to use such photoactive hosts as tools for photocontrolled capture and release of guests.

Chapter 5, describes the materials used for the present study and gives a brief description of the instruments and methods used. Moreover a general description of the multivariate global analysis method used by the SPECFIT/32 commercial program to extract binding constants and spectra of components from multiwavelength equilibrium data is given. Finally, some general remarks and conclusion are given in **Chapter 6**.

INTRODUCTION

The steadily growing pharmaceutical industry demands highly efficient and sophisticated system for the delivery of drugs in order to increase bioavailability, improve efficacy, prevent harmful side-effects and reduce treatment cost. The bioavailability of some drugs is limited due to their poor membrane permeability and low water solubility. Around 70% of the human body is made up of water; therefore, a drug must have certain hydrophilicity or polarity to be water soluble. At the same time these drugs must exhibit a certain lipophilicity to be able to cross lipophilic cell membranes. These requirements led to continuous research on different mechanisms to introduce therapeutic agents into the body, called drug delivery systems (DDS).[1]

Conventional drug delivery methods generally depend on oral administration (solid pills and liquids), creams, ointments, eye drops, gels and intravenous solutions. But they exhibit certain limitations in terms of limited therapeutic effects, partial degradation of drugs before reaching the target, requirement of higher dosage, toxicity and adverse side effects. A number of drug delivery systems are currently developed or under investigation, by taking advantage from the world of micro- and nanotechnology, to circumvent these limitations and improve the potential of respective drug. As a result, these new technologies have prompted the old concept of the "magic bullet" proposed by Paul Ehrlich's vision.[2]

1.1 MAIN TYPES OF DRUG CARRIERS

The recent novel drug delivery approaches include drug modification by chemical means, drug entrapment into suitable carriers and inject them into the bloodstream, and drug entrapment within pumps or polymeric materials that are placed in desired bodily compartments etc. These techniques have already led to delivery systems that enhance drug targeting specificity, lowering systemic drug toxicity and improve human health, and continuous research in this area may lead to the improved delivery of several drugs.[3]

Among the various drug delivery approaches, carrier-based drug delivery is the most widely studied one because while improving the bioavailability of drugs (degree to which a drug reaches the desired cite) it provides necessary protection to the drug molecules. Also, the release profile of associated drugs can be tailored to the respective medical needs by choosing an appropriate host material. Some of the most studied carrier systems are soluble polymers,[3-5] biodegradable polymers,[6,7] polymeric micelles,[8-12] hydrogels, [13] dendrimers,[14-16] microsponges, [17,18] , nanosponges, [19,20] liposomes,[21-25] cyclodextrins,[6,26] nanoparticles[27-30] and most recently metal organic frameworks.[6,31-33] Each of these carrier types offers its own advantages and disadvantages; thus, the choice of a certain carrier for a particular drug can be made only by considering the relevant properties of the latter.

1.1.1 Polymer-based carrier systems

The application of polymers for biomedical purposes is growing very fast because of easy workability, low cost and control of physico-chemical properties. For more than 5 decades polymers have been investigated as carriers to control the drug dosage, [34] to deliver drugs to the selective target and thereby increase the efficacy of treatment, to protect the drug from physiological environment, reduce the side effects and increase the bioavailability to the patients. This delivery method becomes important for toxic drugs which induce various systemic side effects. From the drug delivery point of view, polymer-based devices can be classified as diffusion controlled, solvent activated, chemically controlled or externally triggered systems,[3]which are discussed below.

Diffusion controlled drug delivery systems (**Figure 1.1 (A) and (B)**) involve either dispersion of therapeutic agent within a non-degradable polymer matrix (matrix systems) or drug is surrounded by a polymer membrane to form a micro capsule (reservoir systems). The sustained release of therapeutic agents is driven by diffusion and the drug is released either by transmission through the pores or between polymer chains, such processes controlling the release rate. Drugs can also be released by chemical degradation of the polymer matrix or cleavage of the drug from a polymer backbone (**Figure 1.1 (C) and (D))**.[3]

Another classification defines the solvent activated systems (**Figure 1.1 (E) and (F)**); in this kind of systems water is the main agent which controls the release of drug. The drug is incorporated in a hydrophilic polymer that is stiff or glassy when dry, but swells when exposed to

an aqueous environment and this property of the polymer allows the drug to move outward. In some other systems water may permeate into a drug polymer matrix due to osmotic pressure and create some micro pores and which can cause the drug release. A typical oral capsule or pill is usually a swelling-controlled device. These devices are easy to manufacture but the control of the drug release rate is not stable.[35]

Responsive drug delivery systems are another class of delivery systems, already available commercially, which can control the rate of drug release by chemical signals (solvent, pH, and temperature) or external forces (magnetism, ultrasound). Some examples of these kind of systems are poly(N-isopropylacrylamide), copolymers of poly(ethylene glycol) and poly(propylene glycol), copolymers of poly(lactic acid) and poly(glycolic acid).[36]
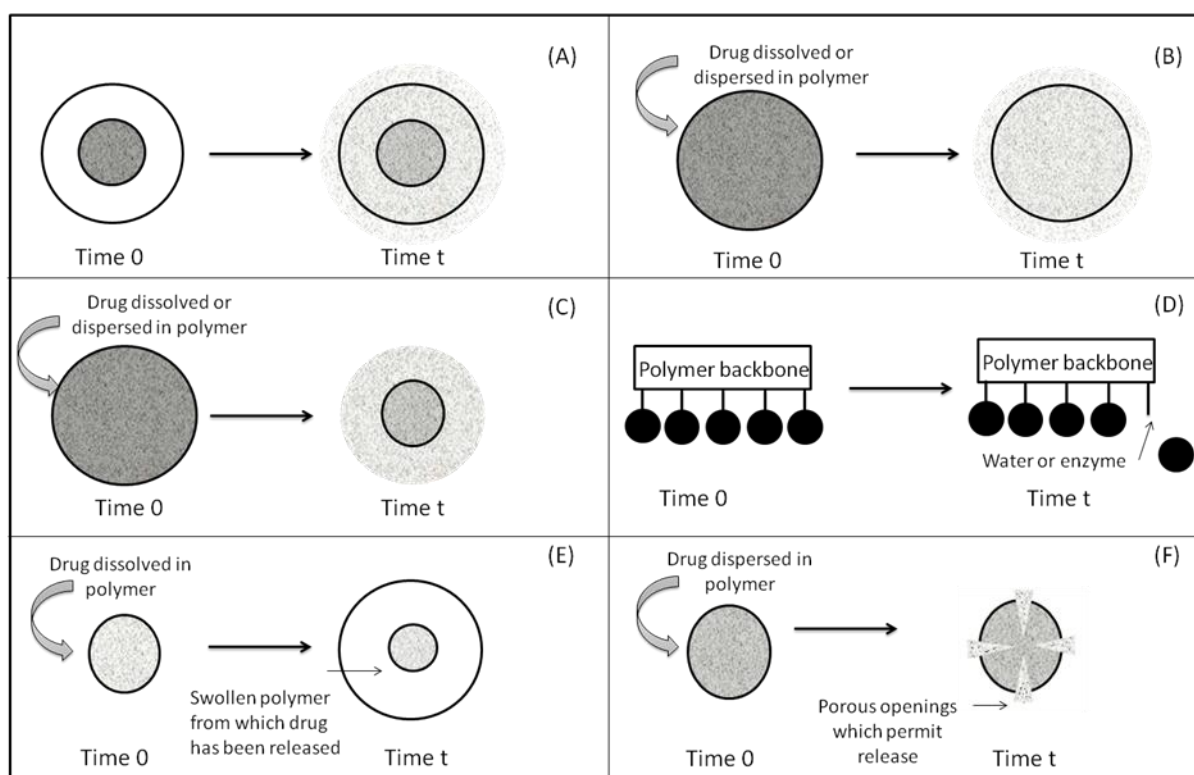
Figure 1.1 Different mechanism for the release of drug from the polymer-drug conjugates, (**A**) diffusion occurs through a reservoir; (**B**) diffusion occurs through a matrix. Drug release due to degradation of (**C**) polymer matrix or (**D**) polymer backbone, (**E**) swelling and (**F**) osmotic pressure

Biodegradable polymers are another important class of polymeric drug delivery systems, most commonly favored to target specific areas of the body such as inflammation or tumors. The biodegradable polymers when exposed to chemicals (water, enzymes, or microbial) disintegrate into biocompatible compounds which subsequently release the incorporated therapeutic agent due to erosion either in bulk or at the polymer's surface. The degradation process basically

involves the breakdown of polymers into biologically acceptable compounds which are further reduced by the Kreb's cycle to carbondioxide and water. Additionally, the biodegradability of these polymers can be easily manipulated by incorporating a variety of labile groups such as ester, amide, anhydride, carbonate, urea, and urethane in their backbone. Examples of such polymers include poly(caprolactone), poly(lactic acid), polyacrylic acids, polyanhydrides, polyesters, poly(methyl methacrylates), and polyurethanes.[37]

1.1.2 Polymeric micelles

Polymeric micelles (**Figure 1.2**) are supramolecular networks, composed of cross-linked combinations of hydrophilic and hydrophobic monomers. They form spontaneously by self-assembly in water, with their hydrophilic and hydrophobic ligands aligned on opposing sides, when the concentration of the amphiphilic block copolymer is above the critical micellar concentration (CMC).

The polymeric micelles are 10-50 nm in diameter (similar size of viruses, lipoproteins and other naturally transporting systems) with a narrow size distribution and can retain the loaded drug for longer period of time. The size of the micelle is generally determined by thermodynamic parameters, but partial control over the size is possible by varying the block length of the polymer.

Further, their hydrophilic outer shells help to protect the cores and the encapsulated drug from chemical attack by the aqueous medium. The spontaneous formation of core-shell architecture is further controlled by the polarity and functionality of each block copolymer. The terminal functionalities on the outer block (the shell) control biocompatibility and may incorporate potential targeting properties; the inner block (core) of such nanocarriers can be used to complex or covalently couple the active drug molecules.[4] Finally, drug release is achieved via common polymer degradation mechanisms, with the specificity of the delivery controlled by the synthetic design.
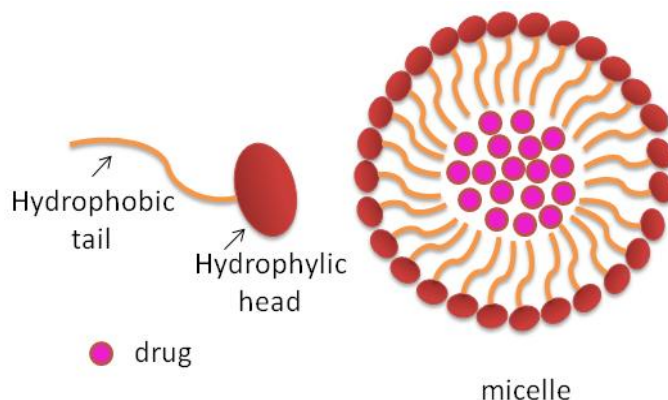
Figure 1.2 Formation and architecture of a block-copolymer micelle

Recently, Japanese researchers have developed a doxorubicin copolymer conjugate which can form micelles in water, and exhibits in vitro cytotoxicity against human small-cell lung cancer cell line (SBC-3). This is the first example of an antitumor drug formulation based on polymeric micelles which has entered into phase1 clinical trial.[10]

Table 1.1 Examples of polymeric micelles used in drug delivery application
(Adapted from Reference 12)

Block copolymers	Drug
Pluronics	Doxorubicin, cisplatin, haloperidol
Polycaprolactone-b-PEG	FK506, L-685, 818
Polycaprolactone-b-methoxy-PEG	Indomethacin
Poly(aspartic acid)-b-PEG	Doxorubicin, cisplatin, lysozyme
Poly(g-benzyl-L-glutamate)-b-PEG	Clonazepam
Poly(D,L-lactide)-b-methoxy-PEG	Paclitaxel, testosterone
Poly(b-benzyl-L-aspartate)-b-PEG	Indomethacin, amphotericin B
Poly(L-lysine)-b-PEG	DNA

1.1.3 Liposomes

Liposomes are tiny vesicles consisting of an aqueous core entrapped within one or more natural phospholipids forming closed bilayered structures. Initially liposomes were utilized as model systems for biological membranes. Phospholipids and other amphiphilic molecules self-assemble in water to form bilayer lipid membranes, separating the aqueous inner core of the liposome from the bulk aqueous phase (**Figure 1.3**). This lipid bilayer structure mimics the barrier properties of

biomembranes and, therefore, offers the possibility of modeling the behavior of these membranes.
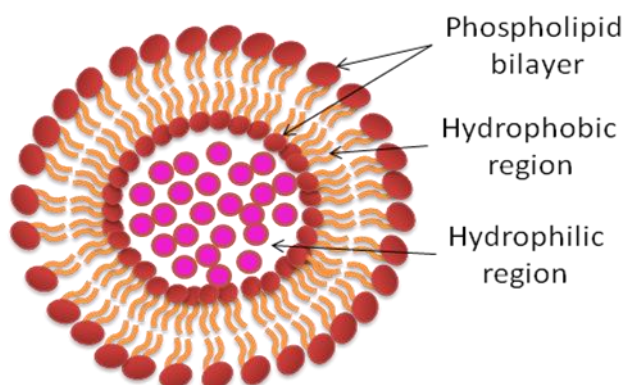
Figure 1.3 Formation and architecture of liposome

Liposomes have been extensively used as potential delivery systems for a variety of compounds primarily due to their high degree of biocompatibility and the enormous diversity of structures and compositions. Liposomes are biphasic, i.e., they have the ability to act as carriers for both lipophilic and hydrophilic drugs. The lipophilic drug molecules can locate in the lipid bilayers of liposomes while hydrophilic drugs may either be entrapped inside the aqueous cores of liposomes or be located in the external water phase. The percentage of hydrophilic drug encapsulation in the liposomes strongly depends on the bilayer composition and preparation procedure of the liposomes

Table 1.2 Examples of liposome formulation used in drug delivery application[38]

Trade name	Drug Class
Epaxal Berna	Vaccine
AmBisome	Amphotericin B
ABELCET	Amphotericin B
DaunoXome	Daunorubicin
Doxil	Doxorubicin
Myocet	Doxorubicin
Visudyne	Verteporfin

1.1.4 Cyclodextrin based carriers

Cyclodextrins (CyDs) are a family of biocompatible cyclic oligosaccharides, derived from starch, consisting of six or more α-D-glucopyranose units joined by α(1-4) glucosidic bonds that form a macrocycle with a hydrophilic exterior and a hydrophobic cavity)(**Figure 1.4**). [39-41] Natural CyDs, α-, β-, γ- CyDs contains 6, 7, or 8 glucose units respectively, differ in their ring diameter (**Table 1.3**) and solubility but each have a height of ca. 7.8 Å. CyDs with less than 6 units cannot be formed due to steric hindrance, and those with 9 or more glucose units are difficult to purify. But recently there are some reports for the isolation and purification of large ring cyclodextrins.[42]

Table 1.3 Characteristics of α-, β-, and γ-CyD[39]

Type of CyD	Cavity Diameter (Å)	Molecular Weight	Solubility (g/100 mL)
α-CyD	4.7 - 5.3	972	14.5
β-CyD	6.0 - 6.5	1135	1.85
γ-CyD	7.5 - 8.3	1297	23.2

Due to the $^4C_1$ conformation of the glucopyranose units, the 3D structure of CyD exhibiting all primary hydroxyl groups on one rim and the secondary hydroxyl groups on the other rim. [41] The ring of CyD has a conical cylinder shape and the cavity is lined by the the glycosidic oxygen bridges and hydrogen atoms. The nonbonding electron pairs of the glycosidic oxygen bridges are directed toward the inside of the cavity, producing a high electron density there and leading it to some Lewis-base character.[41]

The cavity of the torus-shaped CyD is capable of interacting with a wide variety of guest molecules to form noncovalent inclusion complexes. The driving forces for the formation of inclusion complex between CyD cavity and the guest molecule include geometric compatibility, van der Waals forces, London, Debye and hydrophobic interactions. The stability of the inclusion complex may depend on the formation of hydrogen bonding between the CyD and the guest molecule and between the hydroxyl groups on the rims of neighboring CyDs. Due to their highly polar exteriors and less polar interiors, CyDs are best known for their ability to increase the solubility of low polarity guest molecules in water as the encapsulated molecule is shielded from

the aqueous solvent. CyDs are used to encapsulate hydrophobic drugs in drug delivery systems, to enhance the efficiency of low polarity volatile organic compounds, and to mask toxic substances by converting them into nontoxic inclusion complexes.
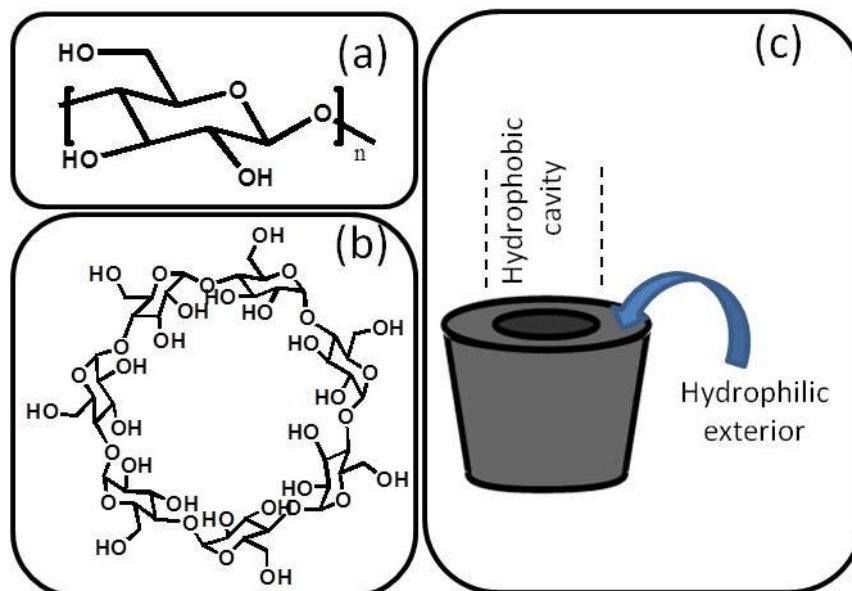
Figure 1.4 Chemical structure of (a) α-D-glucopyranose unit (b) and β-cyclodextrin (c) toroidal shape of a cyclodextrin molecule

Numerous cyclodextrin derivatives have been synthesized for a number of purposes, including increasing aqueous solubility, increasing selectivity of host/guest combinations or controlling the release rate and bioavailability of a drug. For example, modification of hydroxyl groups to hydroxylpropyl, sulfopropyl, carboxymethyl or silyl groups increases the water solubility of natural cyclodextrins[39]. Another possible approach is the production of CyD polymeric nanoparticles and these systems can increase the local concentration of CyD units. Crosslinkers such as epichlorohydrin, citric acid, hexamethylene diisocyanate etc have been used to prepare β-CyD and γ-CyD based polymers.[43,44]

Each year CyDs are the subject of more than 1000 research articles, and most of them deal with drugs and drug-related products. In addition numerous inventions have been described which include CyDs (over 1000 patents or patent applications in the past 5 years). Some examples of approved and marketed drug/CyD formulations are shown in **Table 1.4.**

Table 1.4 Some examples of approved and marketed drug/CyD formulations *(Adapted from Reference 41)*

Drug/cyclodextrin	Trade name	Indication	Formulation	Company/country
PGE_2/βCD	**Prostarmon E**	Induction of labor	Sublingual tablet	Ono, Japan
PGE_1/αCD 20 μg/amp.	**Prostavasin** **Edex**	Chronic arterial occlusive disease, erectile disfunction	Intraarterial inj. Intracavern inj.	Ono, Japan Schwarz, Germany
PGE_1/αCD 500 μg/amp.	**Prostandin 500**	Controlled hypotension during surgery	Infusion	Ono, Japan
OP-1206/γCD	**Opalmon**	Buerger's disease	Tablet	Ono, Japan
Piroxicam/βCD	**Cicladol,** **Brexin**	Anti-inflammatory, analgesic	Tablet, sachet, and suppository	Masterpharma, Chiesi, Italy
Garlic oil/βCD	**Xund, Tegra,** **Allidex,** **Garlessence**	Antiartherosclerotic	Dragees	Bipharm, Hermes, Germany Pharmafontana, H, CTD, USA
Benexate/βCD	**Ulgut, Lonmiel**	Antiulcerant	Capsules	Teikoku, Japan Shionogi, Japan
Iodine/βCD	**Mena-Gargle**	Throat disinfectant	Gargling	Kyushin, Japan
Dexamethasone, Glyteer/βCD	**Glymesason**	Analgesic, anti-inflammatory	Ointment	Fujinaga, Japan
Nitroglycerin/βCD	**Nitropen**	Coronary dilator	Sublingual tablet	Nippon Kayaku, Japan
Cefotiam-hexetil/αCD	**Pansporin T**	Antibiotics	Tablet	Takeda, Japan
Cephalosporin (ME 1207)/βCD	**Meiact**	Antibiotics	Tablet	Meiji Seika, Japan
Tiaprofenic acid/βCD	**Surgamyl**	Analgesic	Tablet	Roussel-Maestrelli, Italy
Diphenhydramine.HCl chlortheophylline+βCD	**Stada-Travel**	Travel sickness	Chewing tablet	Stada, Germany
Chlordiazepoxide/βCD	**Transillium**	Tranquilizer	Tablet	Gador, Argentina
Piroxicam/βCD	**Flogene**	Anti-inflammatory, analgesic for pediatric use	Liquid	Aché, Brasil
Hydrocortisone/HPβCD	**Dexacort**	Mouth wash against aphta, gingivitis, etc.	Liquid	Island
Itraconazole/HPβCD	**Sporanox**	Esophageal candidiosis	Liquid	Janssen, Belgium
Cloramphenicol/ methyl βCD	**Clorocil**	Eye drop, antibiotic agent	Liquid	Oftalder, Portugal
Cisapride/βCD	**Coordinax** **Prepulsid**	Gastrointestinal mobility stimulant	Rectal suppository	Janssen, Belgium
Nimesulide/βCD	**Mesulid Fast** **Nimedex**	Nonsteroid anti-inflammatory	Oral sachet	Novartis (LPB), Italy
Nicotine/βCD	**Nicorette** **Nicogum**		Sublingual tablet chewing gum	Pharmacia Upjohn, Sveden, Pierre Fabre, France
Dextromethorphan/βCD	**Rynathisol**	Antitussive		Synthelabo, Italy
Omeprazole/βCD	**Omebeta**	Proton pump	Tablet inhibitor	Betapharm, Germany
Mitomycin/HPβCD	**MitoExtra** **Mitozytrex**	Anti-inflammatory	Infusion	Novartis, Switzerland
Diclofenac Na/HPγCD	**Voltaren ophtha**	Nonsteroid anti-inflammatory	Eye drop	Novartis, Switzerland
Cetirizine/βCD	**Cetirizin**	Antiallergic		Losan Pharma, Germany
Ziprasidone mesylate/ sulphobutyl βCD	**Zeldox, Geodon**	Antischizophenic	i.m. inj.	Pfizer, USA
Voriconazole/ sulfobutyl-βCD	**VFEND®**	Antimycotic	i.v. inj.	Pfizer, USA

1.1.5 Metal Organic Frameworks

Metal Organic Frameworks (MOFs)[45] are a class of crystalline hybrid materials which are constructed by metal or metal oxide "nodes" connected by organic "linker" compounds forming supramolecular structures with ultrahigh porosity and enormous internal surface areas. The metal nodes serve as connecting points and the organic ligands serve as bridging molecules to coordinatively connect metal nodes forming a two- or three-dimensional framework (**Figure 5**). The enormous possibility to choose the metal nodes and the organic linkers help to tune the physicochemical properties and biodegradable character of the material.
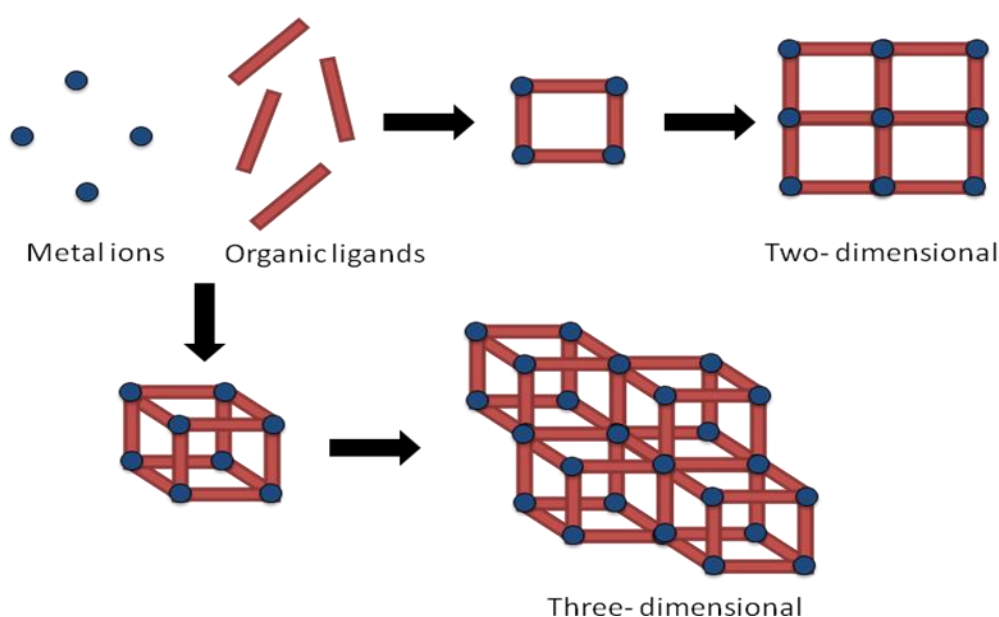
Figure 1.5 A schematic representation of Metal Organic Framework

The most important properties of MOFs is their ultra high porosity (up to 90% of the crystal volume) and high internal surface area. However, the use of these porous materials for biomedical application requires a biologically friendly composition. So it is important to do the toxicity evaluation of the metal ions and linkers individually. At first glance, most appropriate metals are Ca, Mg, Zn, Fe, Ti and Zr, whose toxicity is determined by their oral lethal dose 50 (LD$_{50}$) and metal daily dose (**Table 1.4**).

The most commonly used linkers are exogenous compounds. They can be either synthetic or derived from natural compounds which do not interfere in the body cycles. Some examples of exogenous MOFs for bioapplications are magnesium 2, 5 dihydroxoterephthalate CPO-27 (Mg) (CPO stands for Coordination Polymer from Oslo), iron (III)polycarboxylates, such as MIL-

100(Fe)(MIL stands for Material from Institut Lavoisier) and zinc adeninate-4,4' biphenyldicarboxylate BioMOF-1.

Table 1.4 Oral LD_{50} (Rats) and Daily requirements (Humans) of Selected Metals *(Adapted from Ref 48)*

Metal	LD_{50} (g/kg)	Daily dose (mg)
Zr	4.1	0.05
Ti	25	0.8
Cu	0.025	2
Mn	1.5	5
Fe	0.45	15
Fe^0	30	-
Zn	0.35	15
Mg	8.1	350
Ca	1	1000

Another possible choice for the linkers is the endogenous organic ligands, i.e. molecules that are constitutive part of the body composition. This is the best option for the biomedical applications of MOFs, because one can strongly decrease the risk of adverse effects due to the possibility of re-use of the linker when administered in the body. . A significant number of MOFs based on endogenous linkers have been reported so far. For example, the iron(III)gallate, fumarate or muconate MOFs exhibit either a rigid small pores structure or a highly flexible porous matrix. A porous zinc aminoacid based MOF has also been reported that exhibit a flexible framework. Cyclodextrin based MOFs with rather large pore volumes have also been synthesized.[46,47] Finally, only a few of them are really porous and/or stable, i.e. capable of loading biological molecules of interest and there is still a need to develop new synthetic methods to produce endogenous porous and stable MOFs in near future.

1.2 SCOPE OF THIS Ph.D DISSERTATION

The ultimate goal of the research work presented in this thesis is to develop new multifunctional nanocarriers for drug encapsulation and delivery, as a strategy to overcome current therapeutic drawbacks of anticancer/antiviral drugs. The research work mainly focused on nanocarriers like (i) water soluble and biocompatible oligosaccharides, cyclodextrins (CyDs) and their derivatives

and (ii) a new family of biodegradable nanocarriers made of porous metal-organic frameworks (nanoMOFs). It was examined in particular the non covalent binding of an antitumoral (doxorubicin) and several antiviral (phosphorilated azidothymidines) agents with the nanocarriers, characterizing the host-guest systems with spectroscopic techniques and addressing the association equilibria and the nature of the interactions. Some attention was dedicated also to the antimalarial and antitumoral artemisinin.

The thesis is divided into two main chapters based on the type of drug-carrier system, doxorubicin-cyclodextrin-based conjugates (Ch. 2) and phosphorilated azidothymidine-MOF and doxorubicin-MOF conjugates (Ch. 3). A further chapter (Ch.4) is dedicated to other drug-cyclodextrin carrier systems.

REFERENCES

1. Donatella Paolino, M. F.; Sinha, P.; Ferrari, M. Drug Delivery Systems. In *Encyclopedia of Medical Devices and Instrumentation*, 2 ed.; Webster, J. G., Ed. John Wiley & Sons, Inc.: 2006; pp 437-495.

2. Strebhardt, K.; Ullrich, A. Paul Ehrlich's Magic Bullet Concept: 100 Years of Progress. *Nat. Rev. Cancer* **2008,** *8*, 473-480.

3. Langer, R. New Methods of Drug Delivery. *Science* **1990,** *249*, 1527-1533.

4. Haag, R.; Kratz, F. Polymer Therapeutics: Concepts and Applications. *Angew. Chem. Int. Ed.* **2006,** *45*, 1198-1215.

5. Pillai, O.; Panchagnula, R. Polymers in Drug Delivery. *Curr. Opin. Chem. Biol.* **2001,** *5*, 447-451.

6. Baati, T.; Horcajada, P.; David, O.; Gref, R.; Couvreur, P.; Serre, C. Quantification of Tetramethyl-Terephthalic Acid in Rat Liver, Spleen and Urine Matrices by Liquid-Liquid Phase Extraction and Hplc-Photodiode Array Detection. *J. Pharm. Biomed. Anal.* **2012,** *67-68*, 98-103.

7. Uhrich, K. E.; Cannizzaro, S. M.; Langer, R. S.; Shakesheff, K. M. Polymeric Systems for Controlled Drug Release. *Chem. Rev.* **1999,** *99*, 3181-3198.

8. Ding, H.; Wang, X. J.; Zhang, S.; Liu, X. L. Applications of Polymeric Micelles with Tumor Targeted in Chemotherapy. *Journal of Nanoparticle Research* **2012,** *14*.

9. Nishiyama, N.; Kataoka, K. Current State, Achievements, and Future Prospects of Polymeric Micelles as Nanocarriers for Drug and Gene Delivery. *Pharmacol. Ther.* **2006,** *112*, 630-648.

10. Nakanishi, T.; Fukushima, S.; Okamoto, K.; Suzuki, M.; Matsumura, Y.; Yokoyama, M.; Okano, T.; Sakurai, Y.; Kataoka, K. Development of the Polymer Micelle Carrier System for Doxorubicin. *J. Controlled Release* **2001,** *74*, 295-302.

11. Yokoyama, M.; Okano, T.; Sakurai, Y.; Fukushima, S.; Okamoto, K.; Kataoka, K. Selective Delivery of Adiramycin to a Solid Tumor Using a Polymeric Micelle Carrier System. *J. Drug Targeting* **1999,** *7*, 171-186.

12. Torchilin, V. P. Structure and Design of Polymeric Surfactant-Based Drug Delivery Systems. *J. Controlled Release* **2001,** *73*, 137-172.

13. Ulbrich, K.; Subr, V.; Podperova, P.; Buresova, M. Synthesis of Novel Hydrolytically Degradable Hydrogels for Controlled Drug-Release. *J. Controlled Release* **1995,** *34*, 155-165.

14. Aulenta, F.; Hayes, W.; Rannard, S. Dendrimers: A New Class of Nanoscopic Containers and Delivery Devices. *Eur. Polym. J.* **2003,** *39*, 1741-1771.

15. Boas, U.; Heegaard, P. M. H. Dendrimers in Drug Research. *Chem. Soc. Rev.* **2004,** *33*, 43-63.

16. Cheng, Y. Y.; Zhao, L. B.; Li, Y. W.; Xu, T. W. Design of Biocompatible Dendrimers for Cancer Diagnosis and Therapy: Current Status and Future Perspectives. *Chem. Soc. Rev.* **2011,** *40*, 2673-2703.

17. Kawashima, Y.; Niwa, T.; Takeuchi, H.; Hino, T.; Ito, Y. Control of Prolonged Drug Release and Compression Properties of Ibuprofen Microsponges with Acrylic Polymer, Eudragit-Rs, by Changing Their Intraparticle Porosity. *Chem. Pharm. Bull.* **1992,** *40*, 196-201.

18. Srivastava, R.; Pathak, K. Microsponges: A Futuristic Approach for Oral Drug Delivery. *Expert Opinion on Drug Delivery* **2012,** *9*, 863-878.

19. Trotta, F.; Zanetti, M.; Cavalli, R. Cyclodextrin-Based Nanosponges as Drug Carriers. *Beilstein J. Org. Chem.* **2012,** *8*, 2091-2099.

20. Subramanian, S.; Singireddy, A.; Krishnamoorthy, K.; Rajappan, M. Nanosponges: A Novel Class of Drug Delivery System - Review. *Journal of Pharmacy and Pharmaceutical Sciences* **2012,** *15*, 103-111.

21. Barratt, G. Colloidal Drug Carriers: Achievements and Perspectives. *Cell. Mol. Life Sci.* **2003,** *60*, 21-37.

22. Gabizon, A.; Goren, D.; Horowitz, A. T.; Tzemach, D.; Lossos, A.; Siegal, T. Long-Circulating Liposomes for Drug Delivery in Cancer Therapy: A Review of Biodistribution Studies in Tumor-Bearing Animals. *Adv. Drug Delivery Rev.* **1997,** *24*, 337-344.

23. Gabizon, A. A. Liposome Circulation Time and Tumor Targeting - Implications for Cancer-Chemotherapy. *Adv. Drug Delivery Rev.* **1995,** *16*, 285-294.

24. Gabizon, A. A. Liposomal Drug Carrier Systems in Cancer Chemotherapy: Current Status and Future Prospects. *J. Drug Targeting* **2002,** *10*, 535-538.

25. Kozubek, A.; Gubernator, J.; Przeworska, E.; Stasiuk, M. Liposomal Drug Delivery, a Novel Approach: Plarosomes. *Acta Biochim. Pol.* **2000,** *47*, 639-649.

26. Barreto, L. C. L. S.; Cunha, M. S. S. Cyclodextrin: Important Pharmaceutical Functional Excipient. *Latin American Journal of Pharmacy* **2008,** *27*, 629-636.

27. Bapat, N.; Boroujerdi, M. Uptake Capacity and Adsorption-Isotherms of Doxorubicin on Polymeric Nanoparticles - Effect of Methods of Preparation. *Drug Dev. Ind. Pharm.* **1992,** *18*, 65-77.

28. Bapat, N.; Boroujerdi, M. Effect of Colloidal Carriers on the Disposition and Tissue Uptake of Doxorubicin .2. Conjugation with Isobutylcyanoacrylate Nanoparticles. *Drug Dev. Ind. Pharm.* **1993,** *19*, 2667-2678.

29. Molpeceres, J.; Aberturas, M. R.; Guzman, M. Biodegradable Nanoparticles as a Delivery System for Cyclosporine: Preparation and Characterization. *J. Microencapsulation* **2000,** *17*, 599-614.

30. Chauvierre, C.; Vauthier, C.; Labarre, D.; Couvreur, P.; Marden, M. C.; Leclerc, L. A New Generation of Polymer Nanoparticles for Drug Delivery. *Cell. Mol. Biol.* **2004,** *50*, 233-239.

31. Baati, T.; Horcajada, P.; Gref, R.; Couvreur, P.; Serre, C. Quantification of Fumaric Acid in Liver, Spleen and Urine by High-Performance Liquid Chromatography Coupled to Photodiode-Array Detection. *J. Pharm. Biomed. Anal.* **2011,** *56*, 758-762.

32. Chalati, T.; Horcajada, P.; Couvreur, P.; Serre, C.; Ben Yahia, M.; Maurin, G.; Gref, R. Porous Metal Organic Framework Nanoparticles to Address the Challenges Related to Busulfan Encapsulation. *Nanomedicine* **2011,** *6*, 1683-1695.

33. Horcajada, P.; Chalati, T.; Serre, C.; Gillet, B.; Sebrie, C.; Baati, T.; Eubank, J. F.; Heurtaux, D.; Clayette, P.; Kreuz, C.; Chang, J. S.; Hwang, Y. K.; Marsaud, V.; Bories, P. N.; Cynober, L.; Gil, S.; Ferey, G.; Couvreur, P.; Gref, R. Porous Metal-Organic-Framework Nanoscale Carriers as a Potential Platform for Drug Delivery and Imaging. *Nat. Mater.* **2010,** *9*, 172-178.

34. Ranade, V. V. Drug Delivery Systems .3a. Role of Polymers in Drug Delivery. *Journal of Clinical Pharmacology* **1990,** *30*, 10-23.

35. Hoffman, A. S. Hydrogels for Biomedical Applications. *Adv. Drug Delivery Rev.* **2012,** *64*, 18-23.

36. Kost, J.; Langer, R. Responsive Polymeric Delivery Systems. *Adv. Drug Delivery Rev.* **2012,** *64*, 327-341.

37. Langer, R. Polymer-Controlled Drug-Delivery Systems. *Acc. Chem. Res.* **1993,** *26*, 537-542.

38. Svenson, S. Carrier-Based Drug Delivery. *ACS Symp. Ser.* **2004**, 2-23.

39. Szejtli, J. Introduction and General Overview of Cyclodextrin Chemistry. *Chem. Rev.* **1998,** *98*, 1743-1753.

40. Uekama, K.; Hirayama, F.; Irie, T. Cyclodextrin Drug Carrier Systems. *Chem. Rev.* **1998,** *98*, 2045-2076.

41. Szejtli, J. Past, Present, and Future of Cyclodextrin Research. *Pure Appl. Chem.* **2004,** *76*, 1825-1845.

42. Taira, H.; Nagase, H.; Endo, T.; Ueda, H. Isolation, Purification and Characterization of Large-Ring Cyclodextrins (Cd36 Similar to Cd39). *J. Inclusion Phenom. Macrocyclic Chem.* **2006,** *56*, 23-28.

43.   Shown, I.; Baek-Ko, W.; Murthy, C. N. Cyclodextrin-Based Low Molecular Weight Polymers as Encapsulates for Nonpolar Drug Molecules. *Polymer Bulletin* **2012,** *69*, 1-13.

44.   Wintgens, V.; Amiel, C. Water-Soluble Gamma-Cyclodextrin Polymers with High Molecular Weight and Their Complex Forming Properties. *Eur. Polym. J.* **2010,** *46*, 1915-1922.

45.   Yaghi, O. M.; Li, H. L. Hydrothermal Synthesis of a Metal-Organic Framework Containing Large Rectangular Channels. *J. Am. Chem. Soc.* **1995,** *117*, 10401-10402.

46.   Forgan, R. S.; Smaldone, R. A.; Gassensmith, J. J.; Furukawa, H.; Cordes, D. B.; Li, Q. W.; Wilmer, C. E.; Botros, Y. Y.; Snurr, R. Q.; Slawin, A. M. Z.; Stoddart, J. F. Nanoporous Carbohydrate Metal-Organic Frameworks. *J. Am. Chem. Soc.* **2012,** *134*, 406-417.

47.   Gassensmith, J. J.; Furukawa, H.; Smaldone, R. A.; Forgan, R. S.; Botros, Y. Y.; Yaghi, O. M.; Stoddart, J. F. Strong and Reversible Binding of Carbon Dioxide in a Green Metal-Organic Framework. *J. Am. Chem. Soc.* **2011,** *133*, 15312-15315.

48.   Horcajada, P.; Gref, R.; Baati, T.; Allan, P.K.; Maurin, G.; Couvreur, P.; Ferey, G.; Morris, R.E.; Serre, C. Metal-Organic Frameworks in Biomedicine. *Chem. Rev.* **2012,** *112*, 1232-1268.

SPECTROSCOPIC STUDIES ON DOXORUBICIN ASSOCIATION TO CYCLODEXTRIN BASED SYSTEMS

Anthracyclines represent an extremely important class of anticancer drugs, ranking top among the most potent ones ever developed.[1] They are usually employed in the treatment of leukaemia, aggressive lymphomas and various solid tumors, in particular breast cancer and soft tissue sarcoma.[2] The mechanism of action of these drugs mainly consists in the inhibition of topoisomerase II activity. Topoisomerase II enzymes bind to DNA and allow its cleavage managing and controlling its topological state during transcription and replication. This covalent complex is trapped in the presence of anthracycline drugs so that DNA re-ligation is inhibited, and consequently transcription and replication are blocked.[3-5] The first anthracyclines were isolated from a pigment producing bacterium, called *Streptomyces peucetius* in the 1960s and were named doxorubicin (DOX, also known as Adriamycin, **Scheme 2.1**) and daunorubicin (DNR, also known as daunomycin). These two derivatives have been continuously used in the clinical practice due to their high efficacy, but they have been manifesting serious drawbacks such as development of resistance by cancer cells, severe side effects related to low cardiac tolerability and necrotic action at the injection site.[6] In the last two decades, more than 2000 anthracycline analogs were developed but only a few of them (eg. Epirubicin, idarubicin)[7] have reached the clinical stage.[8] Also numerous studies have focused on the development of improved delivery techniques for existing drugs such as DOX and DNR based on the employment of biocompatible carriers, like micelles, liposomes,[9] polymeric architectures,[10-12] and nanoparticles.[13-16] An example of such formulation is Doxil, a pegylated liposome encapsulated form of DOX.[17]
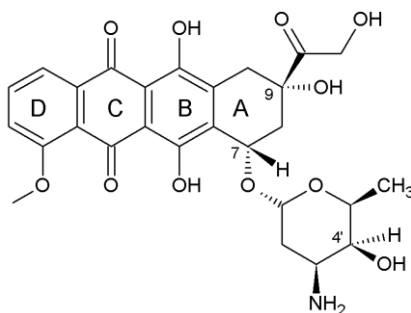
Scheme 2.1 Chemical structure of doxorubicin (DOX)

Such strategy may help to face problems related to drug aggregation, solubility, multi drug resistance and drug toxicity.

In this chapter, we first analyse the self-association behaviour of DOX in aqueous solution (**Chapter 2.1**), which is very important from the pharmacological point of view. The subsequent sections (**Chapter 2.2, 2.3 and 2.4**) are dedicated to the study of the association of DOX to various CyD-based systems such as γ-cyclodextrin, and two CyD-based polymers (an epichlorohydrin crosslinked β-cyclodextrin polymer (p-βCyD) and a citric acid crosslinked γ-cyclodextrin (p-γCyD) polymer) which could represent the starting point for the development of new carriers for anthracyclines.

2.1 SELF ASSOCIATION OF DOXORUBICIN

One of the problems in the application of DOX is self-aggregation in aqueous media. The process, that was evidenced by UV-vis absorption,[18] circular dichroism (CD)[18] and NMR spectroscopy, [18] mainly consists in formation of the DOX dimer at typical clinical concentrations, and represents a serious drawback because it may effectively compete with DNA binding , thereby limiting the drug pharmacological activity.[19] It has been recently suggested by Agrawal et al.[18] on the basis of 2D NOESY spectra that the geometrical arrangement of the two DOX units in the DOX dimer consists in the stacking of the aglycone moieties in either parallel or antiparallel orientation, with the methoxy substituent of D ring pointing toward the exterior or the interior of the interplanar space, respectively (**Scheme 2.2**).
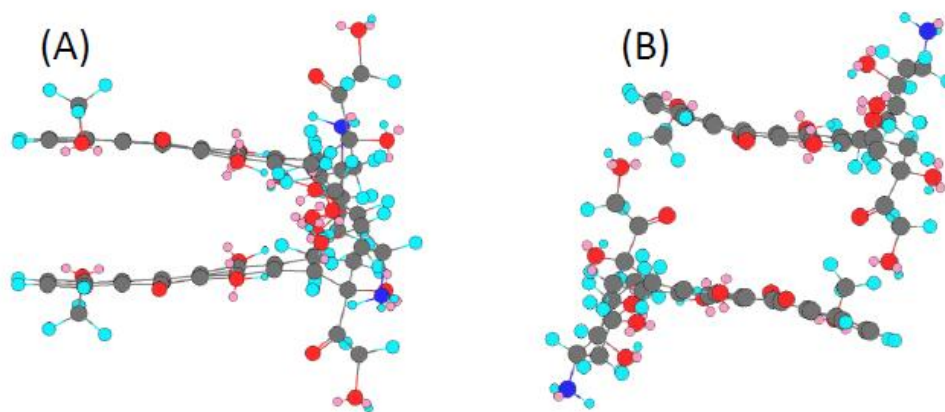
Scheme 2.2 Self association of DOX in aqueous solution: **(A)** DOX parallel and **(B)** DOX antiparallel units[18]

The knowledge of the dimerization constant (K_d) and of the spectroscopic features of DOX monomer and dimer is a prerequisite for the investigation of the drug association to carrier systems. Values for K_d reported in literature somewhat depend on the medium.[20] Its value was therefore redetermined from the dependence of the UV-Visible absorption spectrum on the concentration in the conditions of our spectroscopic experiments.

2.1.1 UV-Visible absorption studies

The UV-visible absorption (**see Experimental section, Chapter 5**) spectrum of DOX in phosphate buffer (**Figure 2.1**) at pH 7.4 displays bands at 288 and 480-500 nm relevant to the two allowed $^1A \rightarrow {^1L_a}$ and $^1A \rightarrow {^1L_b}$ π-π* transitions, polarized along the short and long axis, respectively.[21] A shoulder around 320-380 nm is associated to n-π* transitions of the three C=O groups in the molecule, partially forbidden by electric dipole.[22] Self-aggregation of DOX affects the band shapes and the molar absorption coefficients that tend to decrease at increasing drug concentrations. The spectral profile in the visible region is strongly influenced by the protonation state of the aglycone moiety, but is practically insensitive to the protonation of the daunosamine moiety. At pH 7.4 the aglycone part is neutral, whereas the daunosamine is protonated.[21,22] The absorption bands at 252 and 233 nm are stemming from aglycone moiety,[23] with some contribution of the daunosamine unit.[18] At concentration below 5×10^{-3} M a simple dimerization model is sufficient to describe DOX aggregation.[18] A set of absorption spectra obtained upon DOX dilution in the range 5.0×10^{-5} M – 1.0×10^{-7} M (**Figure 2.1**) was analysed adopting a dimerization equilibrium model with a global analysis method (SPECFIT/32 program) based on Singular Value Decomposition (SVD) and nonlinear regression methods (**see Experimental Section, Chapter 5**). According to the literature[18,24] the experimental absorption spectrum at concentration ~1 x 10^{-6} M (λ_{max} = 500 nm,

$\varepsilon \sim 12000$ M^{-1} cm^{-1}) was assigned to the monomer. This spectrum was fixed in the calculation. A dimerization constant with $\log(K_d/M^{-1})$ = 4.8±0.1 was determined, which is in reasonable agreement with literature data.[20,24,25] The spectrum of the DOX dimer in solution was also extracted and is reported together with that of monomer in the inset of **Figure 2.1**
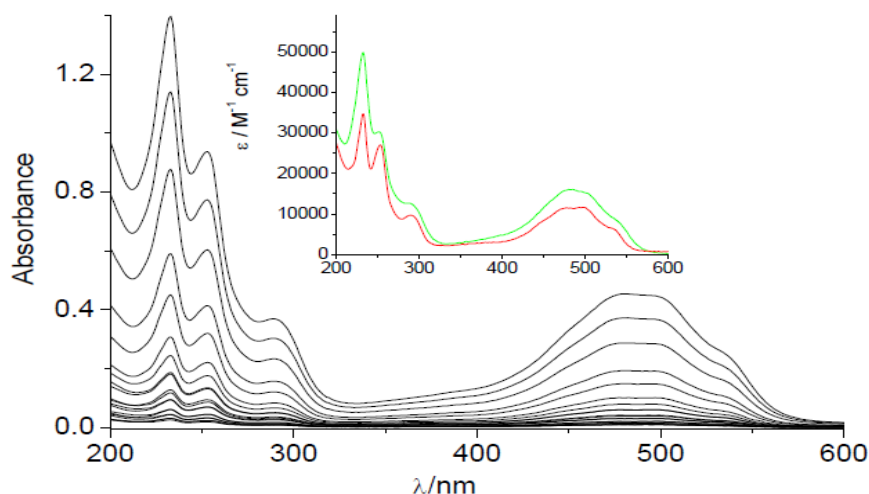
Figure 2.1 Absorption spectra of DOX upon dilution in the range of 5.0×10^{-5}M^{-1} – 1.0×10^{-7}M in 0.01M phosphate buffer at pH 7.4 at 22°C. Cells of different paths were used to register the spectra that are represented after being normalized to cell path of 1 cm. Inset: absolute spectra of DOX monomer (red) and dimer (green).

2.1.2 Circular dichroism studies

The circular dichroism (CD) of DOX also depends on the concentration. Anthracyclines are endowed with an intrinsic CD (**see Experimental Section, Chapter 5**) due to several asymmetric carbon centers. The C7 and C9 configuration are of particular importance in the explored wavelength region (**Scheme 2.1**).[21,22] The CD spectrum of DOX 1.6×10^{-4} M (**Figure 2.2A**) is characterized by negative bands at 293 nm and 516-547 nm and positive bands at 252 nm, 352 nm and 453 nm. The positive-negative split dichroic signal at 420-580 nm region is due to the presence of DOX in dimeric form . The presence of the amino sugar affects the $\Delta\varepsilon$ for the band corresponding to the $\pi-\pi^*$ transition polarized along the long axis, due to the enhancement of the DOX molecular dissymmetry.[21] At DOX concentration $\leq 1.0\times10^{-5}$ M (**Figure 2.2B**) the CD spectrum does not exhibit a prominent negative signal at 530-550 nm and thus suggests the predominance of the monomer over the dimer.
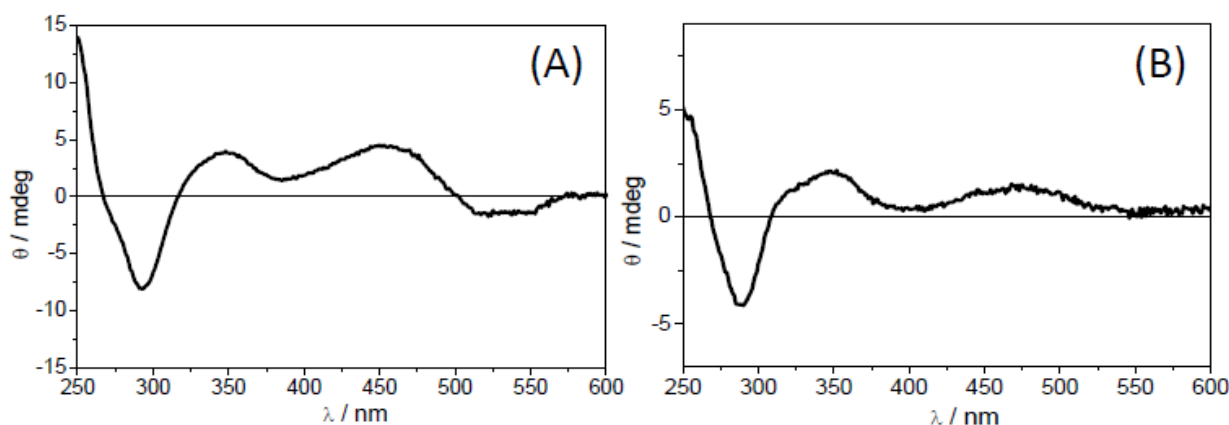
Figure 2.2 (A)CD spectrum of DOX 1.6 x 10^{-4} M, cell pathlength 0.5 cm **(B)** CD spectrum of DOX 1 x 10^{-5}M, cell pathlength 4 cm, in 0.01 M phosphate buffer at pH 7.4 and 22 °C

2.1.3 Summary

In this section, the formation of DOX dimer was analyzed by spectroscopic techniques such as UV-vis absortion and circular dichroism. Global analysis of equilibrium spectroscopic data provided the absolute spectrum of DOX monomer, DOX dimer and a dimerization constant of $\log(K_d/M^{-1}) =$ 4.8±0.1, which is in reasonable agreement with literature data. The CD features of DOX monomer and DOX dimer were also examined by comparing ellipticity profiles at "low" and "high" DOX concentrations.

2.2 ASSOCIATION OF DOXORUBICIN TO γ–CYCLODEXTRIN

As we described in Chapter 1 cyclodextrins (CyDs) are biocompatible cyclic oligosaccharides, made of α-D-glucopyranose units joined by α(1-4) linkages (**Figure 1.4**), that possess a hydrophilic exterior surface and a hydrophobic cavity, able to host lipophilic guests. Natural α-, β-, γ- CyDs contain 6, 7, 8 glucose units, respectively. Since long time they have received considerable attention as drug complexing agents .[26]

The binding of DOX to CyDs has been addressed since the 1990's. At that time it was reported that methyl-β-CyD enhances the activity of DOX on both sensitive and multidrug-resistant cell lines.[27-31] Since then, the interest for this topic has been continuously growing. Self-aggregation of DOX (evidenced in aqueous solution by UV-vis absorption,[20] circular dichroism (CD)[21] and NMR spectroscopy[18]) is likely perturbed by inclusion of the drug in a CyD cavity or a CyD nanoassembly. Therefore, gaining insights into the binding modes of DOX to CyD systems is of direct relevance to the optimization of the use of this drug.

Among the *natural* CyDs, DOX binds significantly to γ-CyD, whereas it possesses lower affinity for β-CyD and α-CyD.[32-35] Formation of a γ-CyD-DOX complex with 1:1 stoichiometry is known since a long time.[32-36] This chapter contains the results of a detailed study of the complexation of DOX with γ-CyD in aqueous medium, performed *via* accurate titrations at different DOX concentrations with circular dichroism (CD), UV-vis absorption and fluorescence monitoring. CD in particular yielded valuable information about the influence of complexation on the monomer-dimer equilibrium, thanks to the markedly different shape of the dichroic signal of DOX monomer and dimer in the 500 nm absorption region, and the sensitivity of this technique to the interaction of DOX with chiral receptors.[22,37] The presence of several CyD complexes was evidenced. Stability constants and spectroscopic characterization of them were obtained. Laser flash photolysis afforded information on the environment experienced by DOX in the complexes. We also studied the association of DOX with γ-CyD in the 1:1 stoichiometry from the structural point of view by Molecular Dynamics Simulations, with explicit solvent and examined the interaction of either the aglycone or the daunosamine moiety with the CyD cavity.

2.2.1 UV-Visible absorption and circular dichroism titrations

"High" DOX concentration. A solution of DOX 1.6×10^{-4} M in phosphate buffer at pH 7.4 was prepared. In these conditions ca. 81% of DOX exists as dimer. Increasing concentrations of γ-CyD in the range 2.0×10^{-4} M - 1.6×10^{-2} M induced rather small UV-Vis absorption variations: a 2-3 nm blue-shift of the visible band, small increase of absorbance at 288 nm and 233 nm and decrease at 252 nm **(Figure 2.3)**. Differently, the presence of the chiral CyD host greatly increased the optical asymmetry of the drug electronic transitions. In fact, the CD changes were very large: i) an overall increase of the signal accompanied by a red shift of ca. 5-7 nm, ii) formation of a new intense negative band at 264 nm, concomitant with a blue shift of the peak at 293 nm to 288 nm and appearance of a shoulder at 306 nm and iii) a small shift of the positive peak from 352 to 362 nm, the only one not displaying an intensity increase (**Figure 2.4A and 2.4B**). The persistence of the positive-negative splitting in the visible region indicated that γ-CyD is not able to disrupt the DOX dimer, the predominant form at this DOX concentration, but associates with it as such.[18,20,24]
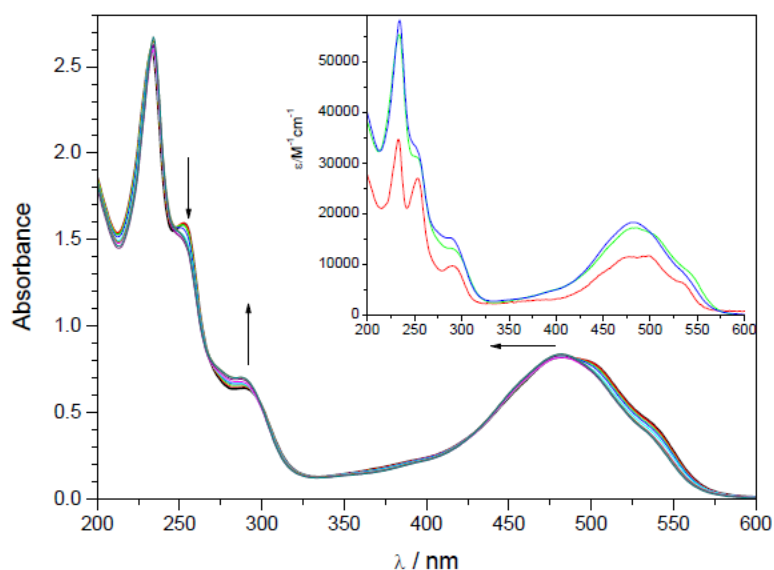
Figure 2.3 Absorption spectra of DOX 1.6×10^{-4} M in phosphate buffer at pH 7.4 at 22 °C upon titration with γ-CyD from 2.0×10^{-4} M up to 1.6×10^{-2} M. Cell path 0.5 cm. Inset: absolute spectra of DOX monomer (red); dimer (green); 2:2 γ-CyD:DOX complex (blue).

The sets of spectra of **Figure 2.4A and 2.4B** were globally analyzed with the SPECFIT/32 program. Several complexation models, involving 1:1, 2:1, 1:2 and 2:2 γ-CyD:DOX complexes in various combinations were tried. The DOX dimerization equilibrium with a fixed constant of log (K_d /M^{-1}) = 4.8 was included. The CD spectrum of DOX alone at concentration 5×10^{-6} M was measured in a 10 cm cell and was assigned to the DOX monomer and also fixed in the calculation. A good fit over the whole 200-600 nm range was found for a model with a single 2:2 CyD:DOX complex with association constant $\log(K_{22}/M^{-3})$ = 10.8 ± 0.2, Durbin Watson (DW) factor of 1.5 (relative error of fit 3.1%) in the 200-280 nm range and DW =1.9 (relative error of fit 6.2%) in the 250-600 nm range. Global analysis of the set of absorption spectra shown in **Figure 2.3** with the same model afforded $\log(K_{22}/M^{-3})$=10.8±0.1 (Durbin Watson factor 2.0) in excellent agreement with the CD result. The individual absolute absorption spectra of all the components are reported in the inset of **Figure 2.3.**

To confirm the stoichiometry of complexation a continuous variation experiment[38] was performed at 1.0×10^{-3} M total γ-CyD + DOX concentration, a compromise between the drug limited solubility/aggregation tendency and the need to have distinctive signals from complexes in the 10^{-4}-10^{-3} M γ-CyD concentration range. The absolute value of the ellipticity at 264 nm associated to the complexation progression (**Figure 2.4B**) was corrected subtracting the DOX intrinsic signal, ($|\Delta\theta_{264}|$) and was plotted against the DOX molar fraction (**Figure 2.4E**).
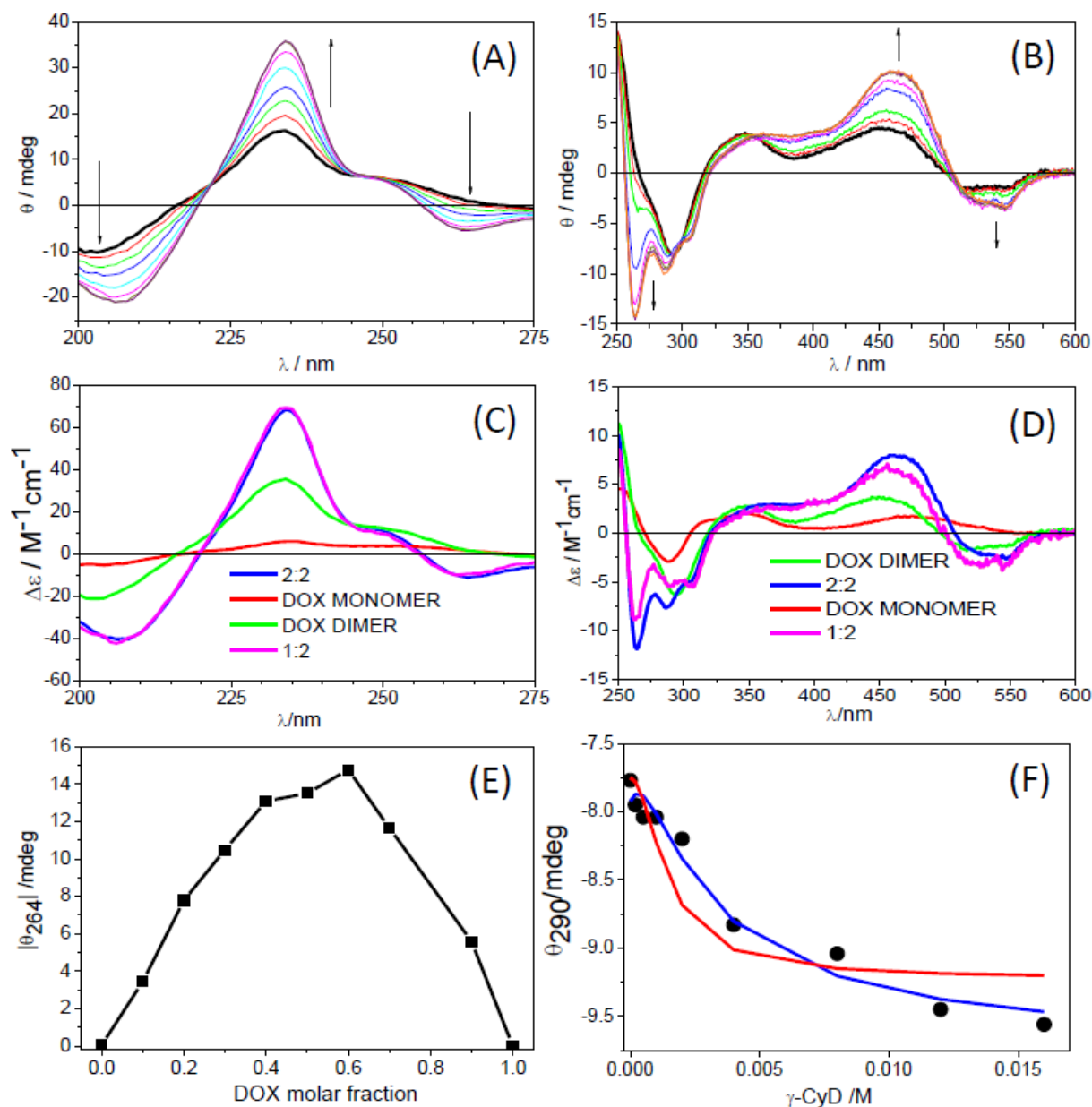
Figure 2.4 Ellipticity changes of DOX 1.6×10^{-4} M in 0.01 M phosphate buffer at pH 7.4 and 22 °C, titrated with γ-CyD in the concentration range 2.0×10^{-4} M - 1.6×10^{-2} M: **(A)** cell path 0.2 cm; **(B)** cell path 0.5 cm. The signal of γ-CyD alone was subtracted. **(C), (D)** Absolute CD spectra of DOX dimer (green), 1:2 γ-CyD:DOX complex (magenta) and 2:2 γ-CyD:DOX complex (blue) for log K_d/M^{-1}= 4.8 and $\log(K_{12}/M^{-2}) = 7.80$ and $\log(K_{22}/M^{-3}) = 10.48$. The spectrum of free DOX monomer (red) was fixed in the calculations. **(E)** Modified Job plot of absolute value of ellipticity of γ-CyD–DOX mixtures at 264 nm, ($|\Delta\theta_{264}|$), subtracting the signal of DOX alone *vs.* DOX molar fraction, total concentration of DOX and γ-CyD =10^{-3} M. **(F)** Comparison of experimental (•) and calculated (line) ellipticity at 290 nm for the model with 2:2 complex only (red, $\log(K_{22}/M^{-3}) = 10.8$) and 1:2+2:2 complexes (blue).

The plot is characterized by a broad asymmetric bell-shape profile with a maximum at ca. 0.6 molar fraction. This indicates a significant, but not exclusive, presence of 1:2 complexes in the equilibrium mixture (exclusive presence of 1:2 stoichiometry would give a maximum at 0.7 molar fraction). Likely the contemporary presence of both 1:2 and 2:2 stoichiometries is the best model

to describe the γ-CyD complexation at "high" DOX concentrations. Indeed assuming such model the global analysis of the data of **Figure 2.4A** and **2.4B** afforded satisfactory fits with log (K_{12}/M^{-2}) = 7.80 ± 0.04 and log (K_{22}/M^{-3}) = 10.48 ± 0.21 (DW = 1.8 and relative error of fit 1.04 % in the UV and DW = 2.4 and error of fit 5.42% in the UV-vis). The extracted spectra of the 1:2 and 2:2 complexes are represented in **Figure 2.4C** and **2.4D**. In the UV region the spectra appear similar to each other, both being characterized by negative peaks at 207 and 264 nm with $\Delta\varepsilon \approx$ -40 and -10 $M^{-1}cm^{-1}$, respectively, and an intense positive peak at 234 nm of $\Delta\varepsilon \approx$ 70 $M^{-1}cm^{-1}$. Also in the UV-vis range the CD spectra of the 1:2 and 2:2 complexes are similar to each other with positive/negative splitting of the lowest energy band and negative peaks of different relative size at 264, 288, 306 nm. In **Figure 2.4F** the comparison between experimental and calculated ellipticity values is shown at 290 nm a wavelength in a critical region, for the model with a 2:2 complex only and the model with both 1:2 and 2:2 complexes. On the basis of the above analysis of the complexation equilibrium we can safely conclude that γ-CyD is not able to disrupt the DOX dimer when the latter is the predominant DOX form in solution, rather forming complexes of 1:2 and 2:2 stoichiometry.

pH titration. In order to gain information about which moiety (either the aglycone or the daunosamine) interact with the γ-CyD macrocycle, an acid-base titration monitoring the absorption of DOX in the pH 6-11 interval was carried out. Deprotonation of the daunosamine-NH_3^+ and of one of the phenolic OH groups of the aglycone ring B in aqueous medium occurs with pKa values of ca. 8.15 and 10.16, respectively[39,40] and produces large changes in both UV (252 and 233 nm bands) and visible regions (**Figure 2.5A**). Encapsulation of the sugar or the aglycone moieties in the CyD cavity was expected to perturb the relevant deprotonation process. Actually in the presence of γ-CyD 1.2 $\times 10^{-2}$ M (ca. 99 % DOX complexed in either 1:2 or 2:2 stoichiometry with a large predominance of the latter one) the pH induced spectral modifications were much smaller over the whole 230-600 nm spectral range. This indicates higher pKa's in the CyD environment for both the deprotonation steps and suggested the likely interaction of both the aglycone and the daunosamine moieties with the γ-CyD cavity.
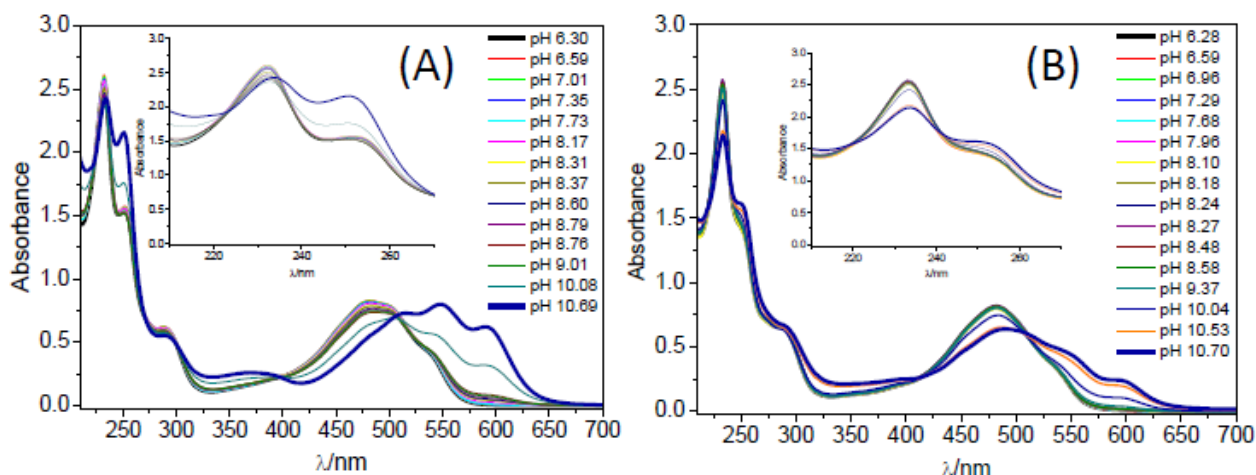
Figure 2.5 (A) Absorption spectra of DOX 1.7×10^{-4} M in 0.01 M phosphate buffer in the range of pH 6-11, reference water, 22 °C; **(B)** The same in presence of γ-CyD 1.2×10^{-2} M; reference γ-CyD solutions. Cell 0.5 cm. Insets: detail of the 210-270 nm range.

"Low" DOX concentration. The complexation of the DOX monomer was investigated at drug concentration of 1.0×10^{-5} M, with γ−CyD concentration varying from 5.0×10^{-5} M to 1.2×10^{-2} M (**Figure 2.6A** and **2.6B**). In these conditions the monomer:dimer concentration ratio is ca. 3:1 in the absence of γ−CyD (58 % of DOX is present in monomeric form). Increasing γ−CyD concentrations induced intensity increase of both the positive band at 470 nm and the negative one at 288 nm; the signals at 252 nm, 233 nm and 202-205 nm also gained intensity but no new bands appeared in the visible region. The sets of CD spectra in **Figure 2.6A** and **2.6B** were analysed again with various complexation models with 1:1, 2:1, 1:2 and 2:2 γ−CyD:DOX complexes in various combinations, all including the DOX monomer-dimer equilibrium. In no case the calculation attained convergence; to attain convergence we neglected the DOX monomer-dimer equilibrium. The best model over the whole spectral window (200 - 600 nm) was that involving contemporary presence of 1:1 and 2:1 γ−CyD:DOX complexes. The relevant optimized binding constants were log (K_{11}/M^{-1}) = 2.7 ± 0.2 and log (K_{21}/M^{-2}) = 4.4 ± 0.5, with DW parameters in the 1.7-2.4 range. The individual spectra of the various species are reported in **Figure 2.6C** and **2.6D** and the agreement between experimental and calculated ellipticity in **Figure 2.6 E**. The calculated binding constant for the 1:1 complex is in good agreement with values previously reported in literature[35,36] and the extracted spectrum for the free DOX monomer is very close to that experimentally measured at 5×10^{-6} M. Global analysis of the UV-vis absorption titration data performed upon fixing the 1:1 association constant confirmed the magnitude of the 2:1

association constant (**Table 2.1**) and afforded the absolute absorption spectra of the 1:1 and 2:1 complexes (**Figure 2.6 F**).
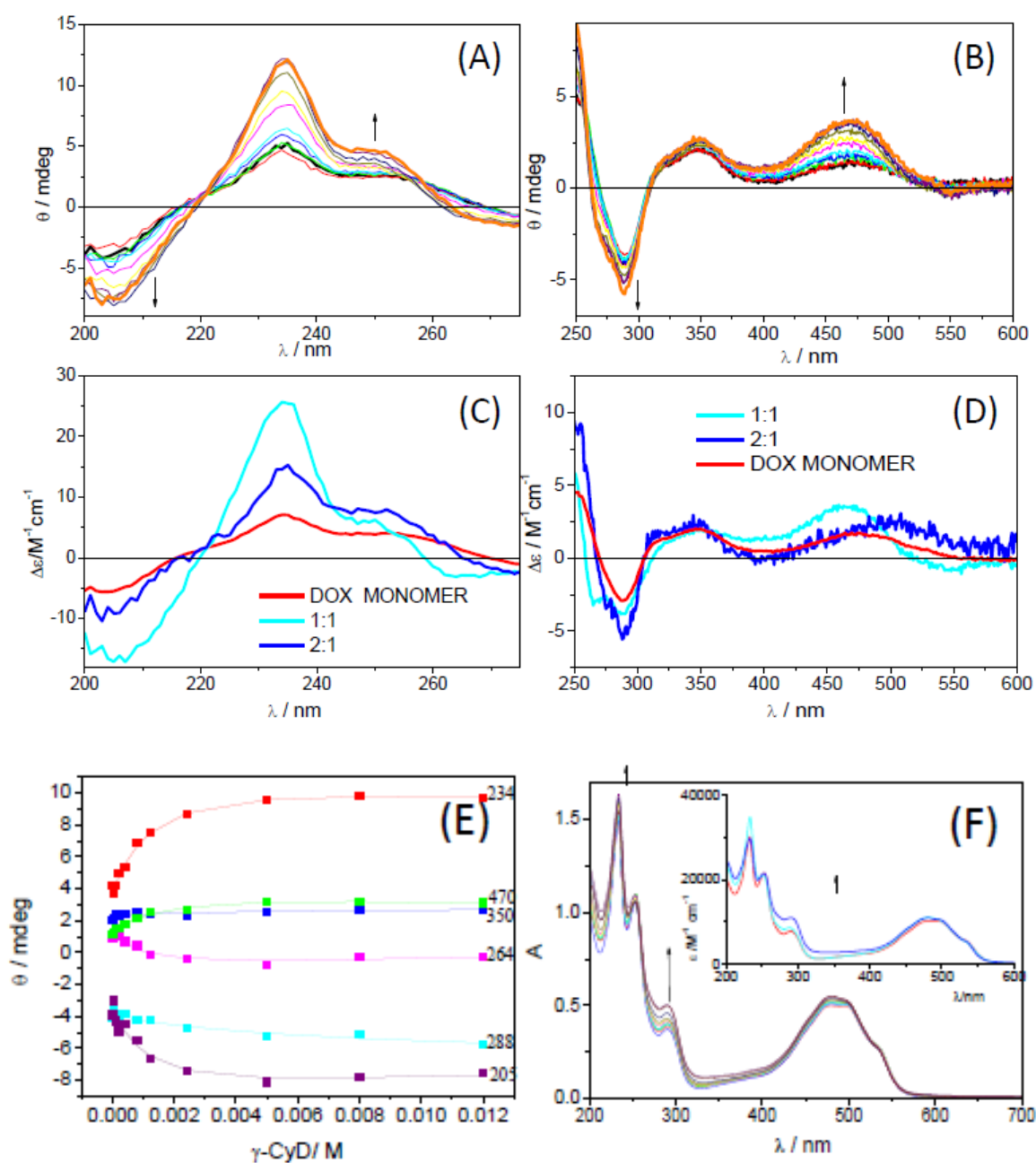
Figure 2.6 Ellipticity changes of DOX 1.0×10^{-5} M in 0.01 M phosphate buffer at pH 7.4 and 22 °C, titrated with γ–CyD in the concentration range 5.0×10^{-5} M - 1.2×10^{-2} M: **(A)** cell path 2 cm; **(B)** cell path 4 cm. The signal of γ–CyD alone was subtracted. **(C)**, **(D)** Absolute spectra of DOX monomer (red), 1:1 (cyano) and 2:1 (blue) γ–CyD:DOX complexes, for log (K_{11}/M^{-1}) = 2.7 ± 0.2 and log (K_{21}/M^{-2}) = 4.4 ± 0.5; (E) ellipticity (θ) at key wavelengths. (F) Absorption spectra of DOX 1.0×10^{-5} M in phosphate buffer at pH 7.4 at 22 °C upon titration with γ-CyD from 5.0×10^{-5} M up to 1.2×10^{-2} M. Cell path 5 cm. Inset: absolute absorption spectra of 1:1 (cyano) and 2:1 (blue) γ-CyD:DOX complexes and DOX monomer (red).

2.2.2 Fluorescence studies

The complexation process was also investigated by detecting the emission of DOX. The method which has to be applied at low DOX concentrations, afforded information on the monomer complexation, because a recent study of the time resolved fluorescence of DOX by fs- techniques, showed the DOX dimer has an ultrashort lifetime and a very low emission quantum yield and does not practically contribute to the steady state fluorescence intensity.[18,41]

A DOX 1.0×10^{-5} M solution in phosphate buffer at pH 7.4 exhibited a structured fluorescence spectrum with λ_{max} = 590 nm. In the presence of increasing concentrations of γ–CyD from 1.0×10^{-4} to 1.6×10^{-2} M, for λ_{exc} = 510 nm both a progressive increase of the main peak at 590 nm and a modification of the vibronic features of the spectrum were observed (**Figure 2.7A**). Global analysis of the whole set of emission spectra confirmed the binding model of the CD and UV-Vis analysis and afforded the 1:1 and 2:1 complexes log (K_{11}/M^{-1}) = 2.3 ± 0.3 and log(K_{21}/M^{-2}) = 4.9 ± 0.1 (Durbin Watson parameter 2.2). The individual fluorescence contribution of each species in solution is reported in **Figure 2.7B**.
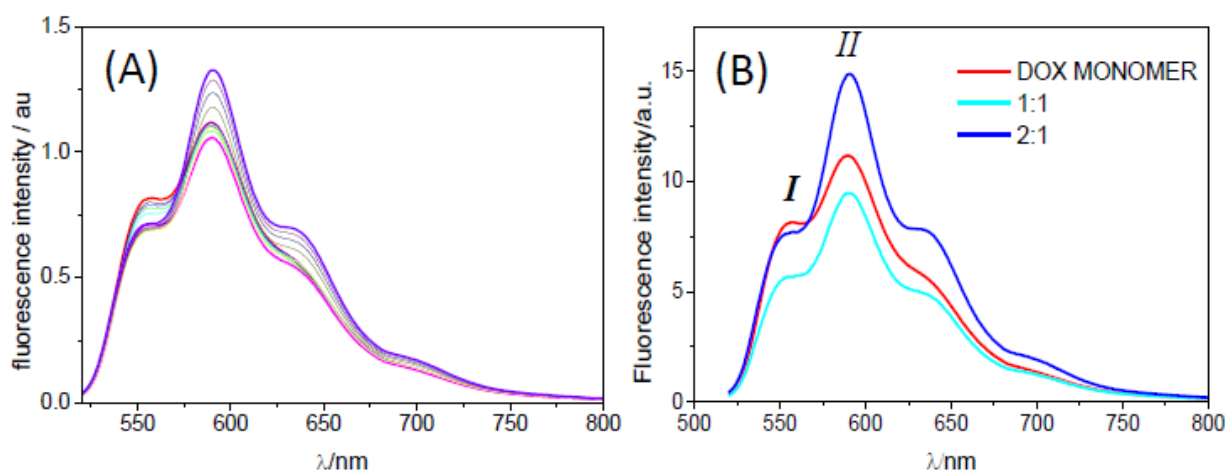
Figure 2.7 (A)-Fluorescence intensity changes of DOX 1.0×10^{-5} M in 0.01 M phosphate buffer at pH 7.4 and 22 °C, upon titration with γ-CyD in the range 1.0×10^{-4} M - 1.6×10^{-2} M; **(B)**- Separated emission spectra of DOX monomer (red); 1:1 (cyano); 2:1 (blue) γ-CyD:DOX complexes, corresponding to log (K_{11}/M^{-1}) = 2.3 ± 0.3 and log (K_{21}/M^{-2}) = 4.9 ± 0.1

The area under each of the spectral profiles of **Figure 2.7B** is proportional to the corresponding emission quantum yield (Φ_f). Using for the DOX monomer the value of Φ_f = 0.039 for DOX 1.0×10^{-5} M in phosphate buffer at 22° C (**Chapter 5, Experimental**), we obtained a value of Φ_f^{11}= 0.032 for the 1:1 and Φ_f^{21}= 0.048 for the 2:1 complex. *(Note: these values maybe somewhat underestimated because a fraction of the excitation light is absorbed by the dimer, which does not contribute to the steady state emission spectra).* The 550 nm/590 nm intensity ratio *(I/II)* in the

emission spectrum of DOX is a parameter probing the environment of the dihydroxyanthraquinone–centered emitting state, because from a value of ca. 0.80 for water, the ratio progressively diminishes in protic solvents of decreasing polarity (e.g. 0.57 in ethanol, 0.51 in 1-heptanol).[42] In the spectra of **Figure 2.7B** *I/II* changes from 0.73 in pure buffer to 0.60 in the 1:1 complex and 0.51 in the 2:1 complex. Thus the *I/II* values in the complexes tend to those of DOX in alcoholic solvents, indicating the excited state of the drug experiences close proximity with the hydroxyl groups of the CyD rim and feels a decrease in the environmental polarity.

The DOX fluorescence decay was detected by time correlated single photon counting (**Chapter 5, Experimental**). It was little affected by the presence of γ–CyD. The decay kinetics was monoexponential with τ_f = 1.02 ns in buffer and 1.13 ns in presence of γ–CyD 5.0×10^{-3} M (DOX $\geq$ 80 % complexed in 1:1 or 2:1 γ–CyD:DOX stoichiometries).[43] Considering the relation of Φ_f and τ_f with the radiative (k_r) and non radiative (k_{nr}) rate constants (**Eqn 2.1**):

$$\Phi_f = k_r\, \tau_f = k_r / (\, k_r + k_{nr}\,) \qquad\qquad \textbf{(2.1)}$$

We observed that k_r and k_{nr} do not substantially change in the γ–CyD complexes compared to buffer (kr $\approx$ 3-4$\times 10^7$ s^{-1} and $k_{nr} \approx 9\times 10^8$ s^{-1}).

We collect in **Table 2.1** the binding constants of the various DOX complexes and in **Table 2.2** their photophysical parameters compared to those in aqueous buffer and in ethanol.

Table 2.1 Association constants of DOX:CyD complexes in aqueous media at pH 7.4, determined with various spectroscopic techniques at 22 °C by global analysis of titration experiments with the SPECFIT/32 program.

DOX complexes	Binding constants	Technique
DOX$_2$ (DOX dimerization) γ-CyD:DOX 2:2	$\log(K_d/M^{-1}) = 4.8 \pm 0.1$	UV-vis absorption
	$\log(K_{22}/M^{-3}) = 10.48 \pm 0.21$	CD
γ-CyD:DOX 1:2	$\log(K_{12}/M^{-2}) = 7.80 \pm 0.04$	CD
γ-CyD:DOX 1:1	$\log(K_{11}/M^{-1}) = 2.7 \pm 0.2$ $\log(K_{11}/M^{-1}) = 2.3 \pm 0.3$	CD Fluorescence
γ-CyD:DOX 2:1	$\log(K_{21}/M^{-2}) = 4.4 \pm 0.5$ $\log(K_{21}/M^{-2}) = 4.9 \pm 0.1$ $\log(K_{21}/M^{-2}) = 4.9 \pm 0.4$	CD Fluorescence UV-vis absorption

Table 2.2 Photophysical parameters of DOX in various media at pH 7.4, 22 °C

	Photophysical parameters				
	$\tau_T/10^{-6}$ s	$\tau_f/10^{-9}$ s	Φ_f	$k_r/10^7 s^{-1}$	$k_{nr}/10^8 s^{-1}$
DOX in buffer	1.7	1.0	0.039	3.9	9.6
DOX in EtOH	3.9	1.4	0.069	4.8	6.5
γ-CyD:DOX 1:2 or 2:2 complex	4.1	–	–	–	–
γ-CyD:DOX 1:1 complex		$\cong 1.1$	0.032	$\cong 2.9$	$\cong 8.8$
γ-CyD:DOX 2:1 complex			0.048	$\cong 4.4$	$\cong 8.7$

2.2.3 Triplet state of CyD:DOX complexes

The triplet state properties are generally useful to gain information on drug environment in CyD complexes.[44] Flash photolysis of a $1.6{\times}10^{-4}$ M DOX solution in Ar-saturated phosphate buffer of pH 7.4 in the presence of $1.6{\times}10^{-2}$ M γ–CyD was therefore carried out with 532 nm laser excitation. In these conditions > 96 % of DOX is associated in 1:2 or 2:2 stoichiometry. A weak differential absorption with bands at 350, 420 and 480 nm was observed **(Figure 2.8A).** Its decay appeared as monoexponential with time constant $\tau = 4.1{\pm}0.1$ µs. It was assigned to the population of the DOX triplet state.[45] Given the adopted experimental conditions the actual assignment was to the triplet of the DOX dimer in the γ–CyD complex(es). Unfortunately, detection of the triplet absorption at DOX concentrations $\approx 1{\times}\,10^{-5}$ M was not possible in our laser flash photolysis apparatus. Thus we could not directly reveal the triplet features of monomeric DOX in the γ–CyD complexes. However, the spectral profile and the lifetime of the transient species shown in **Figure 2.8A** are similar to those observed in EtOH (see **Figure 2.8B**), where the drug is monomeric. Thus, it can be inferred that the triplet state absorption is not significantly affected by the DOX pairing in the dimer (at least in its qualitative features) and probes an alcoholic environment, as expected on the basis of the excited singlet properties of the monomeric DOX complexes. It is worth noticing that the triplet lifetime of DOX in water is sensibly shorter ($\tau = 1.7$ µs) than that in EtOH and in γ–CyD, see also **Table 2.2** [45]
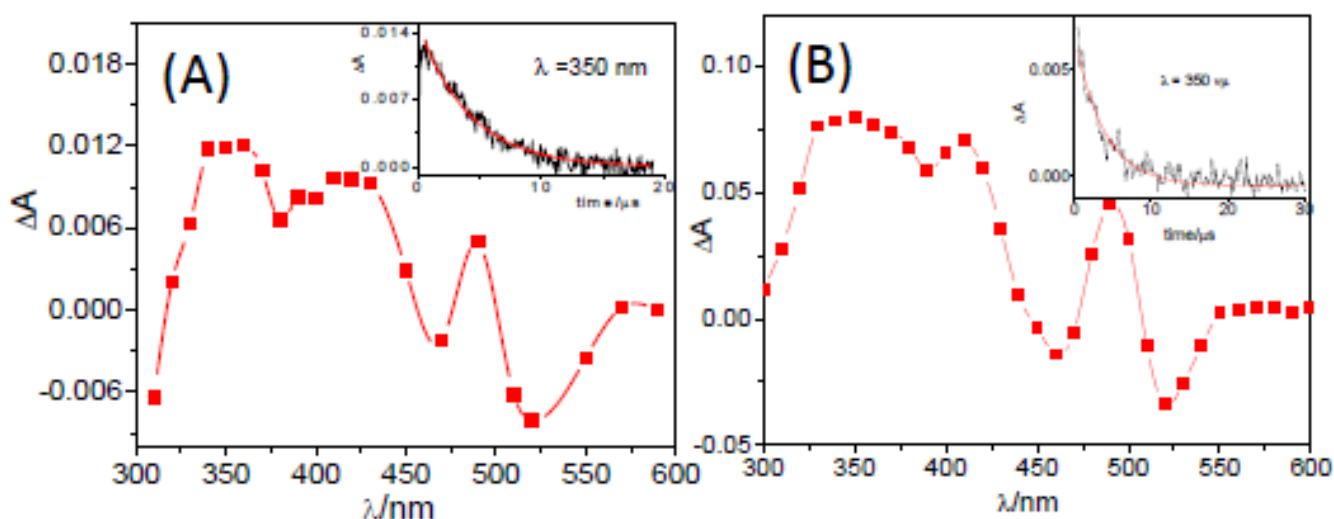
Figure 2.8 Difference absorption spectra observed 300 ns after excitation with a 20 ns laser pulse, cell path 1 cm, at 22 °C: (**A**) $1.6{\times}10^{-4}$ M DOX in Ar-saturated 0.01 M phosphate buffer at pH 7.4 in the presence of $1.6{\times}10^{-2}$ M γ-CyD, laser pulse 532 nm, 3 mJ. (**B**) $7.0 {\times}10^{-5}$ M DOX in EtOH, laser pulse 266 nm, 2 mJ. Insets: decay profiles at 350 nm.

2.2.4 Analysis of Molecular Dynamics trajectories for γ–CyD:DOX 1:1 association

(by Stefano Ottani, CNR-ISOF)

This part is included for the sake of completeness. The interaction between γ-CyD and DOX was also studied by MM and MD modelling. The main purpose of this study was to investigate the ability of the DOX molecule to interact with the γ-CyD cavity with different molecular portion, (A, B, C, D)-rings and the sugar moiety. Some tentative MD runs showed that, in a water box of appropriate size, the γ-CyD/DOX complex forms rather rapidly and, under constant pressure and temperature, the reciprocal arrangements of the partners are quite persistent in their main geometrical parameters, even for long MD runs. **Table 2.3** reports some relevant data obtained from the analysis of the MD trajectories. All the averages in this table are computed by the values obtained at fixed time intervals along the trajectories. Average values of the total energies are all negative and their standard deviations are less than 1%. The mass-weighted radius of gyration, r_{gyr}, has been obtained for the γ-CyD, the DOX and the complex by the **Eqn 2.2**

$$r_{gyr} = \sqrt{\left(\sum_{i=1}^{i=n} w_i (r_i - r_{mean})^2\right) \Big/ \left(\sum_{i=1}^{i=n} w_i\right)} \qquad (2.2)$$

where w_i is the mass of atom i, r_i its position and r_{mean} is the position of the center of mass. Moreover, the visual inspection of the results obtained from MD simulation shows that all the initial geometries reported in **Scheme 2.3** lead to stable complexes. As reported in **Table 2.3**, after the equilibration stage, for the given temperature, pressure and number of molecules of the MD runs, values of energies and geometrical parameters display small standard deviations from their average values. The same trend applies to values of the Root Mean Square Deviations (RMSD) of the complex conformation from a common reference frame, after a simulation run-time > 2ns. Thus, after the equilibration stage, the γ-CyD and DOX molecules reach rapidly a stable reciprocal structural arrangement. The relative placements of the DOX aglycone and daunosamine moieties with respect to the γ-CyD cavity are substantially preserved for MD runs of 10 ns, while the γ-CyD and DOX molecules undergo minor conformational rearrangements. The degree of interpenetration of the two components can be estimated by the values of r_{gyr} of the complex,

which is systematically lower than the sum of the two components and quite similar to the corresponding r_{gyr} of the γ-CyD molecule.
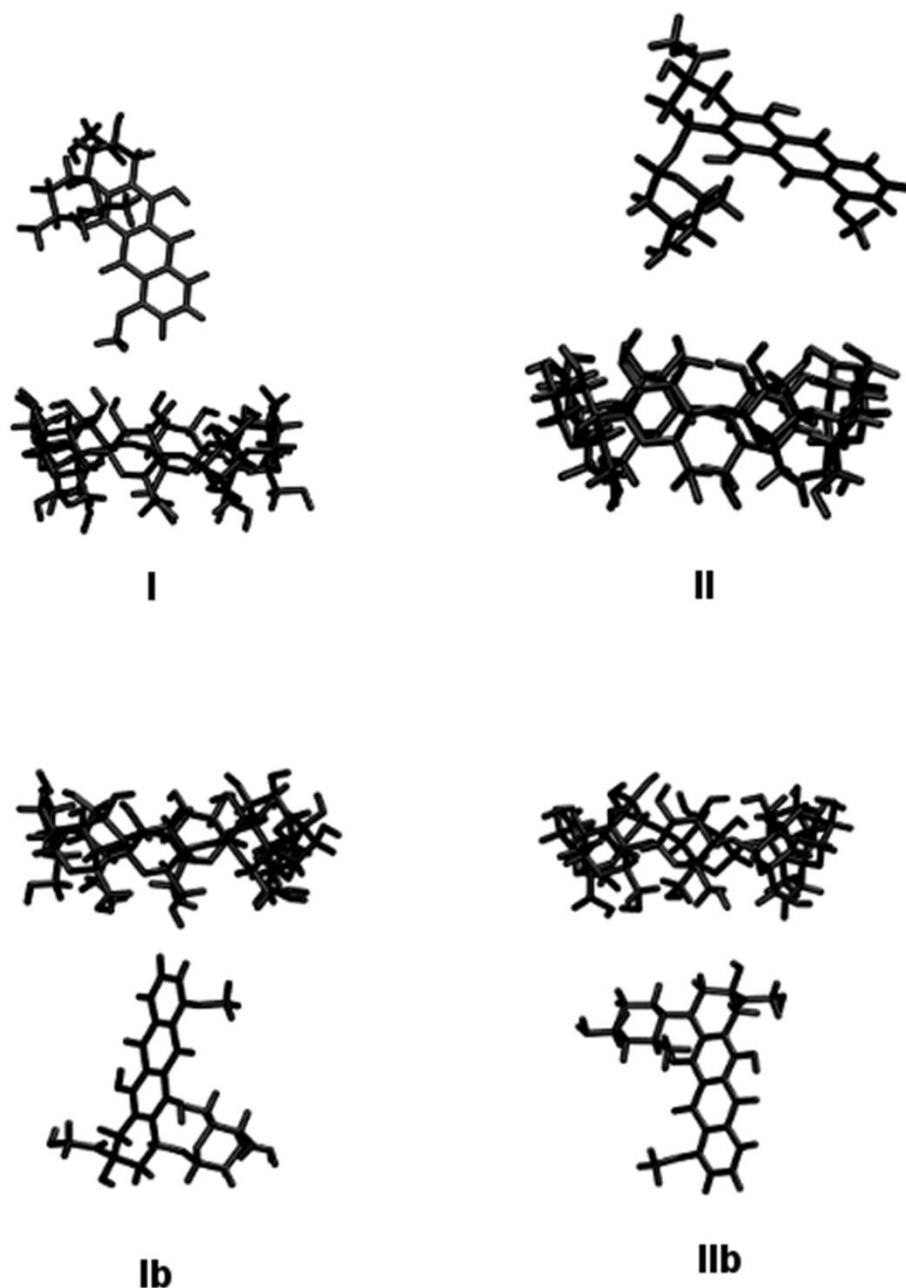
Scheme 2.3 Initial geometries for γ-CyD/DOX system assumed for Molecular Mechanics (MM) and Molecular Dynamics (MD) calculations: I and II, aglycone and daunosamine units facing secondary γ-CyD rim, respectively; Ib and IIb, aglycone and daunosamine units facing the primary γ-CyD rim, respectively.

The stability of the complexes along the trajectories is consistently confirmed by their negative interaction energies and by the small standard deviations in the values of energy and radius of gyration. **Figure 2.9** reports some relevant structures extracted from the MD trajectories.

The labels correspond to the initial geometries of the complexes in **Scheme 2.3** As far as simulation conditions are concerned, these geometries should be regarded as illustrative of stable structures, since temperature fluctuations and collisions with solvent molecules are not able to separate molecules and convert to different complexes. Comparison of geometries in **Figure 2.9** with data in **Table 2.3** shows that the Ib+ initial setting leads to the more stable complex, as confirmed by the lowest values of the Energy, Interaction Energy and r_{gyr}. This final geometry corresponds to the one reported in the literature[33]and it is achieved quite early (< 1ns) in the MD trajectory, by insertion of the D-ring into the γ-CyD cavity through the primary (narrow) rim. **Table 2.3** shows that interaction of DOX with the γ-CyD primary rim is energetically more favored, probably by stabilization with the solvent molecules since the interaction energies are not consistently lower as compared to complexes interacting on the secondary (large) rim.

Table 2.3 Average values of energies and mass-weighted radius of gyration computed from the Molecular Dynamics trajectories for the starting geometries in **Scheme 2**.3

Initial Geometry	Energy Average [kcal mol^{-1}]	Interaction Energy Average [kcal mol^{-1}]	r_{gyr} (complex) Average [Å]	r_{gyr} (γ-CyD) Average [Å]	r_{gyr} (DOX) Average [Å]
I	-16347 ± 114	-38 ± 5	6.17 ± 0.08	6.00 ± 0.08	4.75 ± 0.08
II	-15129 ± 110	-41 ± 6	6.26 ± 0.08	6.55 ± 0.22	4.36 ± 0.07
I+	-17365 ± 118	-46 ± 7	6.12 ± 0.08	6.00 ± 0.07	4.77 ± 0.07
II+	-15623 ± 111	-31 ± 5	6.44 ± 0.17	6.24 ± 0.13	4.56 ± 0.06
Ib	-17586 ± 120	-28 ± 3	6.32 ± 0.14	5.93 ± 0.20	4.78 ± 0.06
IIb	-17671 ± 120	-28 ± 3	6.37 ± 0.10	6.09 ± 0.09	4.78 ± 0.10
Ib+	-19962 ± 122	-47 ± 3	6.14 ± 0.05	6.51 ± 0.09	4.82 ± 0.04
IIb+	-17787 ± 118	-22 ± 4	6.80 ± 0.17	6.08 ± 0.07	4.77 ± 0.07

Actually, r_{gyr} of the I and I+ complexes show that a good packing can be achieved even by interaction on the secondary rim and that especially the I+ structure can be of significance in the complex formation. Inspection of **Figure 2.9** suggests that hydroxyl groups on the γ-CyD rims interact preferably with the conjugated ring system of the DOX, particularly with rings B and C. This is confirmed by comparing the distribution of distances between the γ-CyD center of mass and the B or D-ring, respectively. The B-ring is consistently closer to the γ-CyD center of mass than

the peripheral D-ring, a trend which is even more pronounced in the Ib+ complex. **Figure 2.9** shows that insertion of the DOX daunosamine moiety into the γ-CyD cavity gives rise to stable complexes too. The $-NH_2$ group can cross from the secondary to the primary rim in complex II, while the positively charged $-NH_3^+$ is confined outside the secondary rim in complex II+. NOESY experiments performed by Bekers *et al.* [33] showed that the distance between hydrogen atoms H_2 of the γ-CyD and $H_{4'}$ of the daunosamine is about 3Å for a stable complex. However, the same investigators couldn't obtain optimized molecular models consistent with this result. This point has been investigated in the present work by computing the radial pair distribution function, *g(r)*, for all possible pairs of the DOX $H_{4'}$ atom with the H_2 atoms of the γ-CyD along the trajectories of the eight studied complexes. The pair distribution function is defined as the probability of finding a second particle as a function of distance from an initial particle and its values for the investigated complexes are reported in **Figure 2.10.** Data in this figure show that only complex II+, with the daunosamine moiety into the γ-CyD cavity, comes close to the NOESY experimental constraint. All other complexes, even the most stable Ib+, display probabilities that become significant only at larger distances. Results in **Figure 2.10** are also consistent with the distance of 5.7 Å for the neutral DOX-(S)-isomer obtained previously by molecular modelling. [33] According to the geometries in **Figure 2.9** and data in **Figure 2.10**, it can be concluded that a distance of 3Å is not compatible with the daunosamine $H_{4'}$ atom interacting with the exterior of the γ-CyD molecule[33], which would correspond to larger distances. Instead, it should stem from contributions of structures similar to complex II+, where the daunosamine moiety is inside the γ-CyD cavity. The structure of these complexes suggests a possible rationale for the interaction of the DOX molecule with two γ-CyD units (2:1 complex) as well as for the interaction of the DOX dimer with two γ-CyD units (2:2 complex). Higher order complexes will be the object of further molecular modelling investigations.
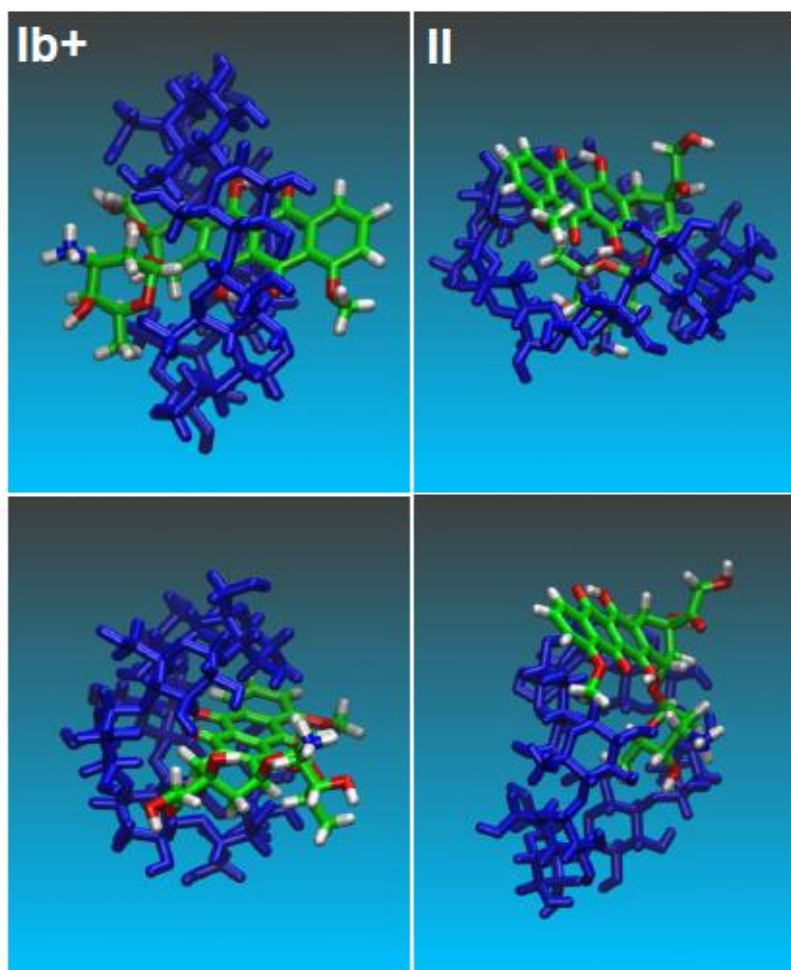
Figure 2.9 Typical geometric arrangements obtained in the MD simulations. The labels correspond to the initial settings in **Scheme 2.3**
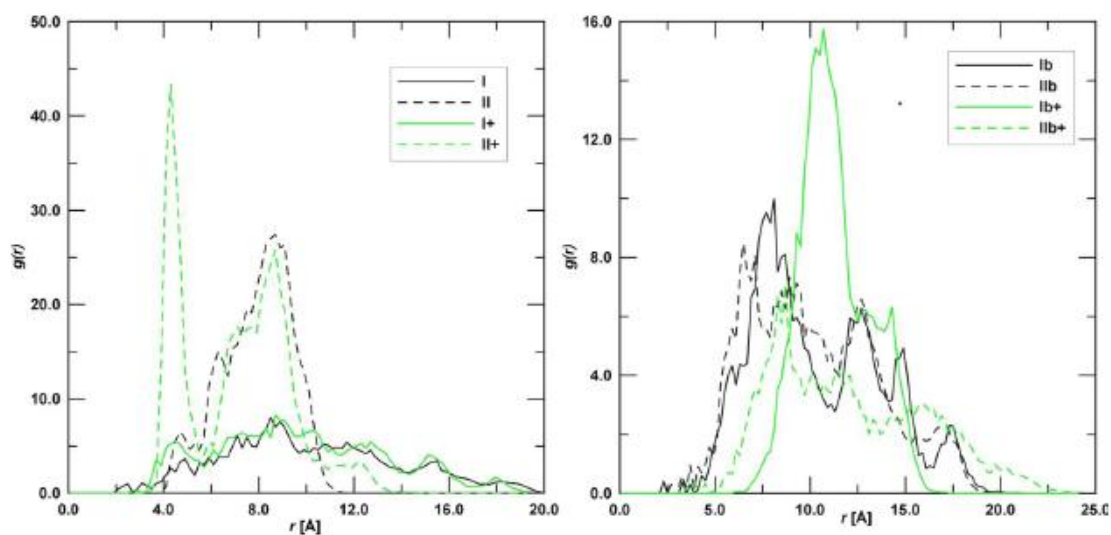
Figure 2.10 Radial pair distribution function, g(r), of the possible pairs between the DOX $H_{4'}$ atom with the H_2 atoms of the γ-CyD. Values corresponding to interactions with the secondary and the primary rim of the γ-CyD are reported in the left and right plot, respectively.

2.2.5 Concluding remarks

The γ–CyD-DOX complexation in aqueous buffer is a process characterized by a great intrinsic complexity, mainly due to the DOX self-aggregation. In the present study the complexation equilibria were analysed by taking into account the DOX monomer-dimer equilibrium, but did not consider the existence of DOX dimer as *parallel* or *antiparallel* stacked structures, each of them expected to have a peculiar affinity for γ–CyD. So, our analysis yields a single spectrum for a given stoichiometry even though it may represent different conformations. In spite of this approximation, UV-vis absorption, CD and fluorescence measurements clearly proved the formation of multiple γ–CyD:DOX complexes. 1:1, 2:1, 1:2 and 2:2 association stoichiometries were evidenced for γ-CyD $\leq 1.6{\times}10^{-2}$ M. The accurate study of the CD allowed to demonstrate that the complexes of monomeric DOX with one (1:1) or two CyD units (2:1) prevail at DOX concentrations $\leq 10^{-5}$ M, whereas complexes of dimeric DOX with one (1:2) or two γ–CyD units (2:2) dominate at DOX concentrations $> 10^{-4}$ M. The formation of higher order γ–CyD:DOX complexes was not reported in the earlier study.[33] The stability constants of all the complexes, determined by global analysis of titration data from several spectroscopic techniques, showed good self-consistency (**Table 2.1**), which reinforces the reliability of the individual CD, fluorescence and UV-Vis absorption spectra for a given stoichiometry

The CD spectra of the 1:1 and 2:1 complexes in the UV region, when compared to each other, point to opposite dichroic contributions for the association of the first and the second γ–CyD unit to monomeric DOX; the corresponding profiles in the visible indicate that the CD feature is increased in intensity and blue shifted in the 1:1 complex and somewhat decreased in intensity and red-shifted in the 2:1 complex. These changes suggest that the aglycone moiety interacts with γ–CyD in the first complexation step while the daunosamine unit interacts in the second one.[46]

The MM and MD trajectories support the CD interpretation. Geometries in **Figure 2.9** (Ib+) and data in **Table 2.3** show that the most favourable interaction is that with DOX aglycone part approaching the γ–CyD primary rim. The complex geometry is characterized by the dihydroxy-anthraquinone core (ring C and B) embedded in the cavity with long axis parallel to the γ–CyD axis and ring D protruding out of the CyD secondary rim. A further possible complex geometry is that

represented in **Figure 2.9** (I+) where the flexible γ−CyD macrocycle folds to embrace the aglycone part. The shape of the fluorescence spectra (**Figure 2.7B**) is consistent with both Ib+ and I+ structures. The quantum yields and the lifetimes in both 1:1 and 2:1 complexes appear to be little modified with respect to those of the free molecule in agreement with the existence of structures with a large exposure of the dihydroxy-anthraquinone part to solvent. MM and MD simulations evidence the daunosamine moiety can also interact favourably with the γ−CyD macrocycle from the secondary rim side. The sugar unit penetrates more deeply into the cavity when the amino group is not protonated (compare structure II and II+ in **Figure 2.9**). Thus the calculations support that two γ−CyD units can be associated to the aglycone and the daunosamine moieties in the 2:1 complex.

The positive-negative split dichroic signal in the 420-580 nm region, due to π−π∗ transitions of the DOX dimer, is maintained in the 1:2 and 2:2 complexes, indicating γ−CyD is not capable of disrupting the stacking interaction of the aromatic chromophores of DOX in either parallel or antiparallel arrangement. The pH effects on the UV-Vis absorption spectrum (**Figure 2.5**) demonstrate that the γ−CyD strongly perturbs the acid–base equilibria of DOX in the "dimer" concentration regime, both those of the aglycone moiety more clearly reflected in the spectral changes at λ > 500 nm, and likely also that of the daunosamine. Considering the experimental conditions, where the 2:2 complex largely predominates, and the geometries proposed for the DOX dimer (**Scheme 2.3**)[18] γ−CyD might access both the aglycone pair and the amino sugar tails. The possibility for the latter complexation mode is supported by the structures II and II+ in **Figure 2.9.**

Finally, CD spectra of the higher order γ−CyD complexes, molecular modeling results and pH effects on electronic absorption consistently support the conclusion that primary binding involves the aglycone part whereas secondary binding involves the daunosamine moiety.

2.3 ASSOCIATION OF DOX TO β−CYCLODEXTRIN POLYMER (pβ−CyD)

In the last section we have seen that γ-CyD is able to form stable inclusion complexes with both DOX monomer and dimer but failed to disrupt the dimer when it is the predominant form in solution. In this context, we analyzed the complexation behavior of DOX with a β-CyD polymer (pβ-CyD), that can spontaneously form nanoparticles of ca. 15 nm diameter in aqueous solution.[47-51] These kind of CyD derivatives are capable of dramatically enhancing the apparent solubility of several guests, compared to natural cyclodextrins. For the evaluation of pβ-CyD as delivery

platform for DOX the incorporation of the drug within the polymer nanoparticles was investigated, performing accurate CD and UV-vis absorption titrations, and fluorescence measurements.

2.3.1 Synthesis of pβ-CyD

β-Cyclodextrin polymer (pβ-CyD) was prepared by reacting β-cyclodextrin (β-CyD) with epichlorohydrin (EP) under strong alkaline conditions (**Scheme 2.4**) [52,53]. Synthetic procedure is as follows: 100 g of anhydrous β-CyD were dissolved in 160 mL aqueous NaOH (33% w/w) solution and kept under mechanical stirring for overnight. Then, 81.52 g of EP (molar ratio β-CyD/ EP = 10) were rapidly added to the solution heated to 30°C. In order to obtain a high molecular weight polymer, the reaction was stopped in the vicinity of the gelation point by addition of acetone. The aqueous phase was heated to 50°C overnight, neutralized with 6N HCl and ultrafiltered using membranes with a cut-off of 30,000 g/mol. The pβ-CyD, which has a branched structure as shown in **Scheme 2.4**, was finally recovered by freeze-drying.

The pβ-CyD was characterized by a β-CyD weight ratio of ~70% (w/w), which was determined by ^{1}H NMR spectroscopy. The average molecular weight of the polymer, 2.1×10^5 g/mol, was determined by size exclusion chromatography.
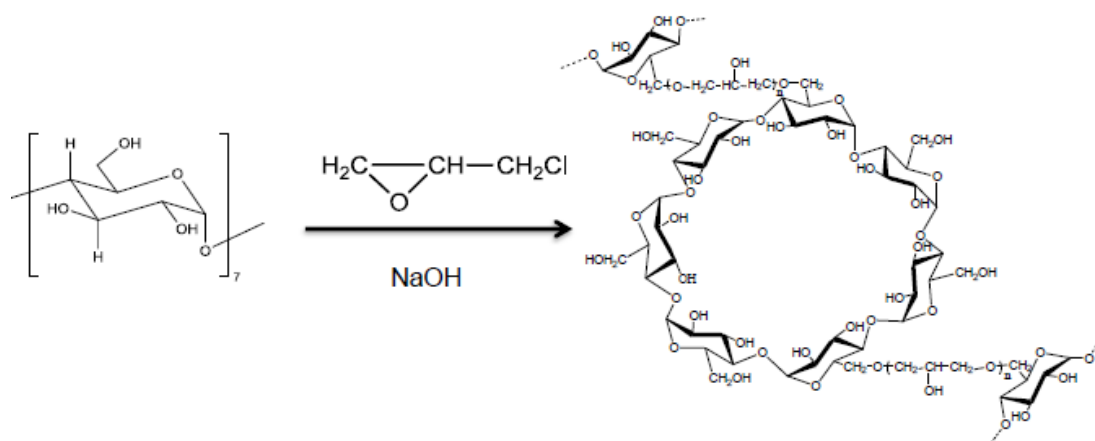
Scheme 2.4 Synthesis of pβ-CyD

2.3.2 UV-visible absorption and circular dichroism

The entrapment of DOX into pβ-CyD was studied by titrating DOX with the polymer (maximum used polymer conc. is 50 mg/ml ie., 2.4×10^{-4} M pβ-CyD which corresponds to a concentration 3.1×10^{-2} M in terms of CyD units). The addition of pβ-CyD (conc. 5 - 50 mg/ml) into DOX solution

(1.7 x 10^{-4} M) causes negligible change in the UV-vis absorption spectra (**Figure 2.11F**), whereas the changes were well evidenced by circular dichroism spectroscopy. The positive-negative CD splitting corresponding to the DOX $\pi-\pi*$ longer wavelength transition tends to cancel with increasing polymer concentration (**Figure 2.11A** and **2.11B**). The sets of CD profiles from 200 to 275 nm and from 250 to 600 nm were globally analyzed with the SPECFIT/32 program for the determination of the equilibrium constant. A simplified approach was used in which the host concentration is expressed in β-CyD units, according to the known β-CyD/pβ-CyD content of 70 % w/w. The DOX dimerization equilibrium, log (K_d/M^{-1}) = 4.8 was included in the analysis and a 1:1 complexation stoichiometry was assumed. The best fit was found for an apparent association constant log(K_{11}/M^{-1}) = 2.2 ± 0.1 (Durbin Watson factor 2.2 and 2.5, relative error of fit 2.3 % and 2.7 % over the data of **Figure 2.11A** and **2.11B**, respectively). A fair agreement between experimental and calculated data can be appreciated in **Figure 2.11E** and is testified also by the fair statistical parameters of the fit. Thus the assumed equilibrium model appears to be acceptable.

The absolute CD spectrum of the complex, extracted in the analysis and reported in **Figure 2.11C** and **2.11D**, does not exhibit any exciton splitting of the visible band and is very similar to that of the DOX monomer in aqueous solution, measured at 5×10^{-6} M DOX concentration and fixed in the calculations. These results support the effective disruption of the DOX dimer on drug association to the polymer nanoparticles.

In the previous section it was shown that γ-CyD up to 1.6×10^{-2} M is not able to disrupt the DOX dimer at DOX concentration of 1.7×10^{-4} M at 22 °C, but forms 1:2 and 2:2 γ-CyD:DOX complexes (log(K_{12}/M^{-2}) = 7.80 and log (K_{22}/M^{-3}) = 10.48). In addition, a 1:1 complex was evidenced at a lower DOX concentration (~10^{-5} M) with a constant log(K_{11}/M^{-1}) = 2.3-2.7, slightly higher than that of pβ-CyD. The question arises: why the β-CyD polymer is able to disrupt the DOX dimer whereas γ-CyD is not, when DOX is present mainly in its dimeric form? A rationale can be found considering various factors.
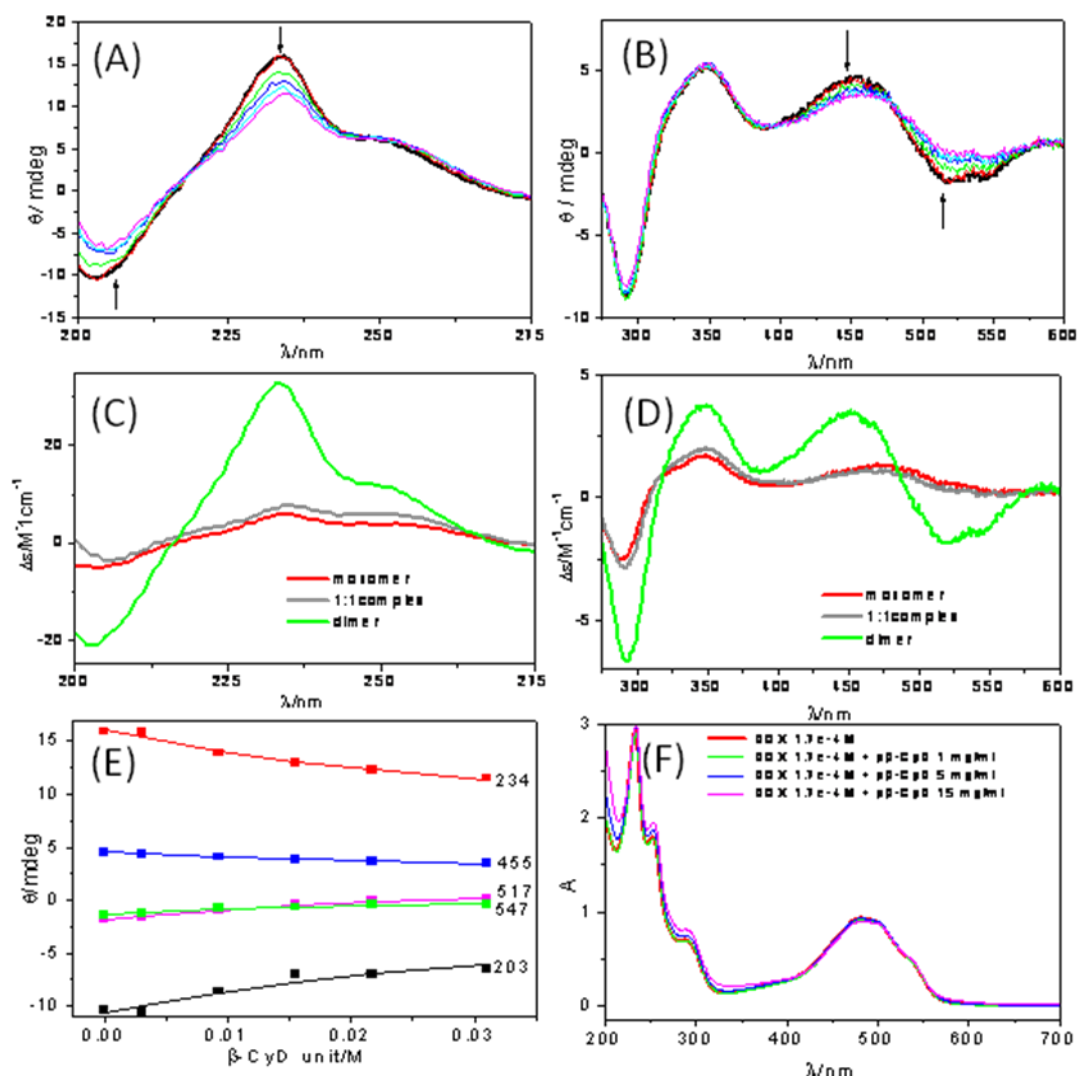
Figure 2.11 Ellipticity changes of DOX 1.7×10^{-4} M in 0.01 M Tris Buffer at pH 7.4 and 22 °C, titrated with pβ-CyD from 5 mg/mL up to 50 mg/mL. (**A**) Cell pathlength 0.2 cm; (**B**) Cell pathlength 0.5 cm. (**C** and **D**) Absolute spectra of DOX dimer (green) and 1:1 β-CyD:DOX complex (grey), corresponding to $\log(K_{11}/M^{-3}) = 2.2 \pm 0.1$. In the calculation the spectrum of free DOX monomer (red) was fixed and the titrant concentrations were expressed in β-CyD units. (**E**) Comparison of experimental (squared symbols) and calculated (lines) ellipticities at key wavelengths of spectra **A** and **B**.

The binding constants with γ-CyD and pβ-CyD cannot be compared to each other, because the first one is based on the actual concentration of host in solution, while the second one is based on the *average* β-CyD-unit concentration and neglects the actual organization of the β-CyD-units in nanoparticles. Moreover the binding constant for the β-CyD unit within the nanoparticle may be underestimated since not all the β-CyD units (for example those in the core of the nanoparticle) are equally accessible to DOX. This possibility has been already highlighted in the case of pβ-CyD loaded with other molecules of interest in the biomedical or cosmetic fields. [47-51] The local concentration of β-CyD in the nanoparticles may be much higher than the average concentration

in solution and the close vicinity of β-CyD units may facilitate cooperative effects in DOX complexation. In these conditions monomeric DOX may be preferentially complexed since penetration of the DOX dimer into the particle frame may be prevented by steric hindrance. All these facts can favour the binding of DOX as monomer, despite the apparently low stability constant of the complex. Finally it is worth observing that the CD spectrum for DOX in the pβ-CyD frame is almost identical to the one observed in homogeneous solution and no significant CyD-induced circular dichroism (ICD) contributions adding to the intrinsic signal are observed. It is likely that DOX is not deeply inserted in the cavity of the β-CyD unit of the polymer.

2.3.3 Fluorescence

As already pointed out in the previous section, DOX in aqueous buffer exhibits a structured fluorescence spectrum with λ_{max} = 590 nm (see **Figure 2.12**); the emission decay, monitored at 590 nm with excitation at 465 nm, is mono-exponential with τ_1 = 1.0 ns ($\chi 2$ = 1.02); the kinetics and the lifetime do not depend on the DOX concentration. These features are consistent with fluorescence being mainly contributed by the DOX monomer.[18,41] Addition of pβ-CyD in various amounts determines an increase of the fluorescence intensity with no change in the spectral shape (see **Figure 2.12**) and a modification of the decay kinetics. Bi-exponential decay analysis applies fairly well. With one lifetime fixed as τ_1 = 1.0 ns for DOX in buffer, the second lifetime is τ_2 = 1.5 ns ($\chi 2$ = 0.8). The relative amplitudes (**Eqn 2.3**) of the two components are reasonably consistent with the binding progression, with f_1 = 58% and f_2=42% at 15 mg/ml and f_1 = 36% and f_2 =64% at 50 mg/ml polymer content. The τ_2 component was therefore attributed to DOX embedded in the pβ-CyD nanoparticle.

$$f_i = (a_i \times \tau_i)/ \Sigma_j(a_j \times \tau_j) \qquad\qquad (2.3)$$

The approximate quantum yield Φ_2 of complexed DOX was estimated from the integrated fluorescence spectra of DOX (5×10^{-5}M) in the absence and in the presence of pβ-CyD at different concentrations, obtained with excitations at 550 nm in an isosbetic region of the absorption (see **Figure 2.11F**). A value of $\Phi_2 \cong 0.13$ was calculated upon subtraction of the background and consideration of the fractions of free and bound DOX for either 15 mg/ml (0.61 and 0.39, respectively) or 50 mg/ml (0.25 and 0.75, respectively), assuming DOX in buffer as reference with quantum yield Φ_1 = 0.039. Good consistency between the two polymer concentrations was found.

Considering the relation between Φ and τ (**Eqn 2.4**):

$$\Phi = k_r\tau = k_r/(k_r+k_{nr}) \qquad\qquad \textbf{(2.4)}$$

The radiative (k_r) and nonradiative (k_{nr}) rate constants were derived and compared in different media (**Table 2.5**). Interestingly, the photophysical parameters of DOX in the nanoparticles differ from those in the γ-CyD environment and in protic solvents. A substantial increase of the radiative rate is observed in the pβ−CyD complexed DOX. This effect might be correlated to changes in the H-bonding features of the DOX excited state within the nanoparticle frame, where intramolecular quinone-hydroquinone H-bonded conformations could be favoured, leading to emission from a more extended conjugated system.[54]
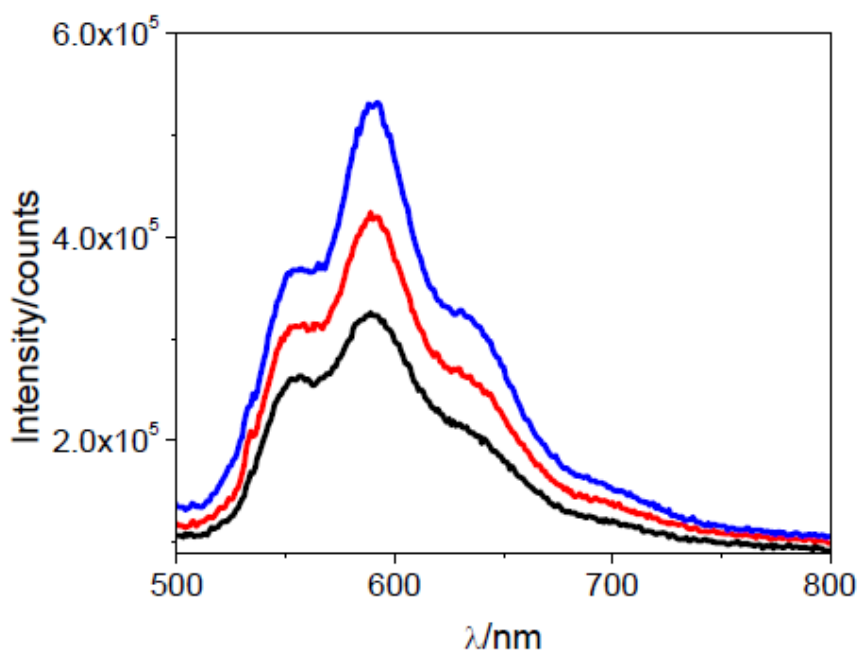
Figure 2.12 Fluorescence intensity of DOX 5×10^{-5} M in 0.01 M phosphate buffer at pH 7.4 and 22 °C, alone (black) and in presence of pβ−CyD 15 mg/mL (red) and 50 mg/mL (blue), excitation was at 465 nm with 45° incidence onto a triangular cell and the detection was at right angle.

Interestingly the photophysical parameters of DOX in the polymer differ from those in the γ-CyD cavity and in buffer and are similar to those in ethanol. This fact indicates that pβ−CyD offers a hydrophobic alcohol-like environment to DOX.

Table 2.4 Dimerization constant of DOX and association constants of DOX:CyD 1:1 complexes in aqueous media at pH 7.4, determined with various spectroscopic techniques at 22 °C.

DOX complexes	Binding constants at 22 °C	Technique
DOX$_2$ (DOX dimerization)	log (K$_d$/M^{-1}) = 4.8± 0.1	*UV-vis absorption*
γ-CyD:DOX 1:1 complex	log (K$_{11}$/M^{-1}) = 2.3/2.7	*Fluorescence/CD*
β-CyD unit:DOX 1:1 in pβ-CyD nanoparticles	*log (K$_{11}$/M^{-1}) = 2.2 ± 0.1*	*CD*

Table 2.5 Photophysical parameters of DOX singlet excited state S1 in various media at pH 7.4 , at 22 °C.

Samples	S_1 photophysical parameters			
	Φ	$\tau/10^{-9}$ s	$k_r/10^7 s^{-1}$	$k_{nr}/10^8 s^{-1}$
DOX in buffer	0.039	1.0[a]	3.9	*9.6*
DOX in EtOH	0.069	1.4[a]	4.8	*6.5*
γ-CyD:DOX 1:1 complex	0.032	$\cong$ 1.1[b]	$\cong$ 2.9	$\cong$ 8.8
γ-CyD:DOX 2:1 complex	0.048	$\cong$ 1.1[b]	$\cong$ 4.4	$\cong$ 8.7
DOX within pβ-CyD nanoparticles	$\cong$ 0.13	1.5[c]	$\cong$ 8.7	$\cong$ 5.8

[a] Monoexponential decay. [b] Decays remain mono-exponential in presence of γ-CyD. The apparent lifetime was assigned to the complex. [c] Lifetime τ_2 in the bi-exponential decay analysis performed in presence of p$\beta-$CyD at various concentrations.

2.3.4 Summary

This study highlights the interest of using highly water soluble CyD polymers as carriers for drugs such as DOX. In particular the study evidenced the ability of the p$\beta-$CyD nanoparticles to disrupt the DOX dimers in solution, a fact relevant to the optimal administration of this important drug. The photophysical parameters point to a modification of the inherent emission ability in the

hydrophobic interior of the polymer nanoparticles. The apparent binding constant is rather low, but this is most likely a consequence of the neglect of actual nanostructured organization of the polymer and of the inherently low binding ability of the β-CyD cavity for the large DOX molecule. Crosslinked γ−CyD polymers proved to be more effective in including DOX inside the CyD cavity. The next section of this chapter will address the interaction of a γ-CyD-based polymer system with DOX.

2.4 ASSOCIATION OF DOXORUBICIN TO γ−CYCLODEXTRIN POLYMER (pγ−CyD)

Considering the results on the interaction of DOX to γ−CyD and pβ−CyD (**Chapter 2.2** and **2.3**) it was envisaged that crosslinked γ−CyD polymers may promote monomerization through the polymer spatial organization as well as effective binding of the drug by inclusion in the large γ−CyD cavities. In this context, a citric acid- γ−CyD crosslinked polymer (pγ−CyD, see **Scheme 2.5**) has been synthesized and its interaction with DOX in neutral TRIS buffer, has been investigated by means of various spectroscopic techniques. Binding and stability constants have been explored in the DOX concentration range 1×10^{-5}-2×10^{-4}M with both DOX monomer and dimer existing in solution. The uptake and biodistribution of the pγ−CyD-DOX conjugate within breast tumor cell line (MCF-7) was studied by confocal fluorescence microscopy.

2.4.1 Synthesis of pγ−CyD

To a solution of 9.6 g citric acid (50 mmol) and 2.1 g of NaH_2PO_4 ·$2H_2O$ (13 mmol) in 100 mL distilled water, 12.97 g of γ-CyD (10 mmol) were dissolved and the obtained solution was evaporated under reduced pressure at 90°C till complete dryness. The powdered mixture was then put in a paraffin oil bath pre-heated at 140°C for 30 min. To the yellowish material 50 mL of distilled water were added and an insoluble gel-like structure immediately formed. The crude was filtered to separate the insoluble fraction from the soluble one. The water phase was neutralized with 0.5 N HCl, concentrated under reduced pressure and then dialyzed overnight (12 kDa cellulosic membrane). The solution was finally dried under reduced pressure to yield 13.5 g of slightly yellow powder.
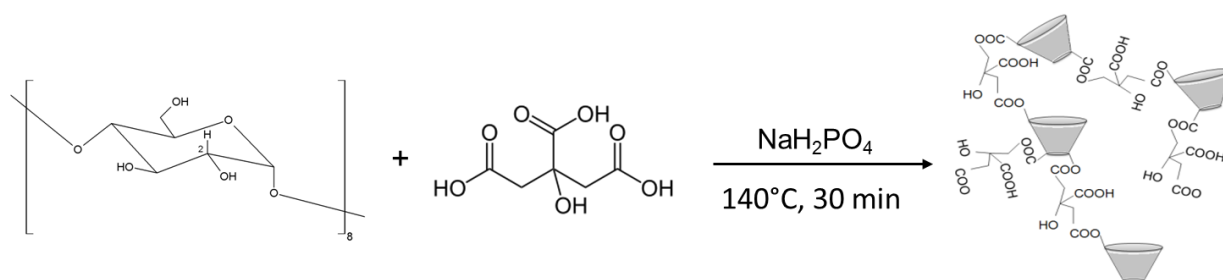
Scheme 2.5 Synthesis of pγ-CyD

2.4.2 UV-vis absorption and circular dichroism

The UV-vis absorption spectra of DOX 1.6×10^{-4} M alone and in the presence of increasing concentration of pγ–CyD in TRIS buffer (0.01M at pH 7.4) are shown in **Figure 2.13A**. pγ–CyD does not show any characteristic absorption band in the visible region. The intense tail observed at high polymer concentrations (pγ–CyD > 10^{-3}M) is likely due to a contribution of scattering. Assuming the dimerization constant measured in phosphate buffer (log K_d/M^{-1} = 4.8) 81% of DOX exist as dimer. Upon addition of pγ–CyD at low concentration (< 4.8×10^{-5} M) the absorption band at 480 nm shows a decrease in intensity with red shift in the maximum (~10 nm). Increase in the polymer concentration causes a progressive increment of the absorption intensity accompanied by a blue shift of the whole band. A fairly good isosbestic region can be recognized at ca. 530 nm.

Further insight into the association of DOX to pγ–CyD was gained from circular dichroism. The ellipticity of DOX 1.6×10^{-4} M in neutral TRIS buffer exhibits a negative band at 293 nm, a positive band at 352 nm and a positive-negative splitting in the visible band (positive component at ca. 460 nm and weaker negative component in the 510-540 nm region). The latter feature indicates the presence of dimers in solution. [21] Indeed no negative component in the visible region is present at concentrations of DOX < 1.0×10^{-5} M, in agreement with the predominance of the monomer. The ellipticity of the DOX solution modifies upon titration with pγ-CyD in the polymer concentration range from 6.1×10^{-6} M to 3.6×10^{-3} M (**Figure 2.13B**). At low polymer concentration the spectral profile appears to be very different from that of DOX alone in both the UV and the visible region: the positive band at 460 nm increases in intensity and shifts to the red of ca. 6 nm; below 380 nm a negative band with minimum at 310 nm appears, instead of the positive one at 352 nm observed in the absence of polymer. At polymer concentrations ≥ 4.8×10^{-5} M the positive CD band in the visible region tends to decrease, further shifting to the red, and the dimer negative CD component at 510-540 nm tends to disappear; below 380 nm a re-shaping of the signal toward

the initial profile occurs. Along with the titration two quasi-isoelliptic points are maintained at 493 nm and 365 nm. These features reasonably point to (i) formation of DOX multimolecular aggregates associated to pγ-CyD at low polymer concentration and (ii) establishment of an equilibrium of different DOX complexes, likely with lower stoichiometries, at higher polymer concentrations. Global analysis of the CD titration data of **Figure 2.15B** actually demonstrated a progressive monomerization of DOX at increasing pγ–CyD concentrations **(see section 2.4.4)**.
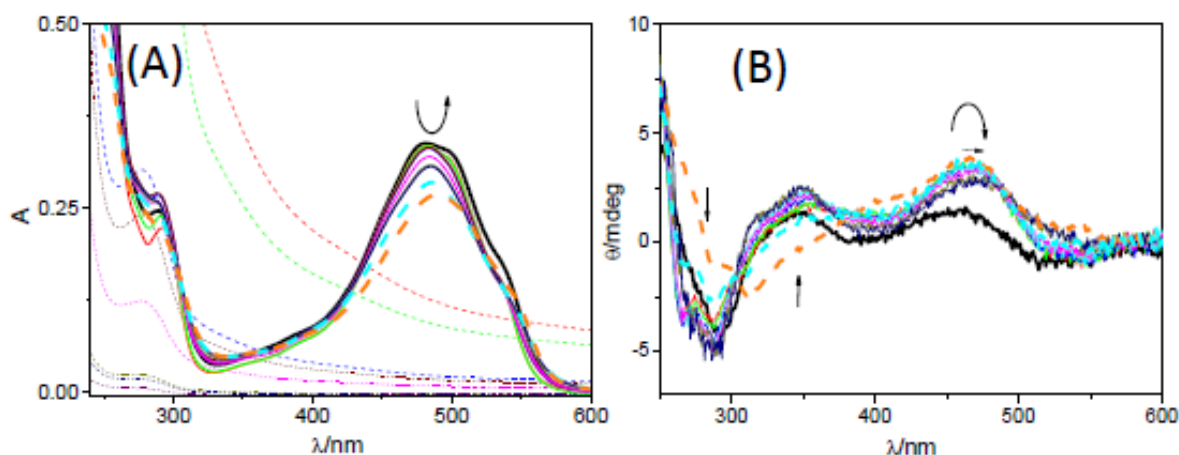
Figure 2.13 DOX 1.6×10^{-4} M in TRIS buffer 0.01M, pH7.4, in presence of pγ–CyD from 6.1×10^{-6} M to 3.6×10^{-3} M (concentrations in pγ-CyD_unit from 8.8×10^{-5} M to 5.3×10^{-2} M). Cell pathlength 0.2 cm, T= 295 K. (**A**) UV-Vis absorption spectra of pγ–CyD solutions (short-dashed thin lines) and DOX- pγ-CyD mixtures (solid lines and dashed thick lines) (**B**) CD spectra. References are pγ–CyD solutions in TRIS buffer for the spectra of the mixtures, TRIS buffer for the spectra of DOX alone and pγ–CyD alone.

2.4.3 Fluorescence

Figure 2.14 shows the fluorescence spectra of DOX 1×10^{-5} M in neutral TRIS buffer at 22°C in the absence and presence of different concentrations of the pγ–CyD polymer (from 3.03×10^{-6} M up to 9.3×10^{-4} M), with excitation at 530 nm. At this DOX concentration, in the absence of the polymer, 58 % of DOX is present in monomeric form. As we have already pointed out, the DOX dimer has an ultrashort lifetime and a very low emission quantum yield and does not practically contribute to the steady state fluorescence intensity.[41] Accordingly the fluorescence spectrum shows the characteristic features of the DOX monomer with vibronic bands at 590, 560 and 630 nm. [55]Addition of pγ–CyD at the lowest concentration drastically decreased the fluorescence intensity. This effect can be understood with the formation of non emissive multimolecular aggregated species of DOX associated to pγ–CyD. Further increase in the pγ–CyD concentration led to a progressive increment of the DOX fluorescence intensity, reasonably associated to

monomerization of the drug with increase of overall emission quantum yield. Inclusion in the pγ−CyD unit and/or the 3D frame of the polymer can be hypothesized.
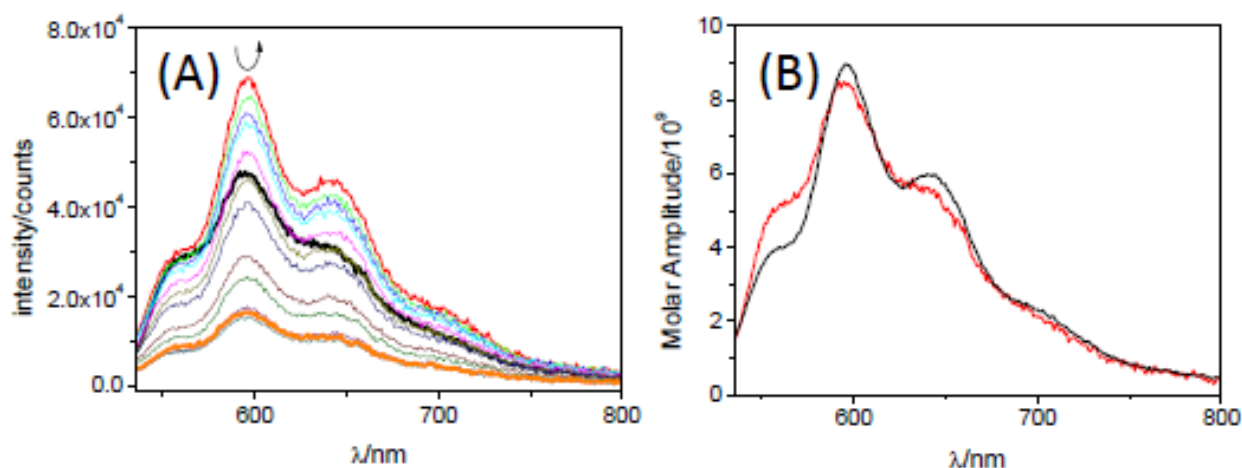
Figure 2.14 (**A**) Fluorescence titration of DOX 1×10^{-5}M in TRIS buffer (0.01M, pH 7.4) with pγ−CyD (concentration in pγ−CyD unit from 3.08×10^{-5} to 9.3×10^{-3}M). Excitation was at 530 nm, the spectra were corrected. (**B**) Molar amplitude of emission for DOX monomeric species extracted by global analysis (red-DOX monomer, black-1:1 pg-CyD unit:DOX complex) with log (K_{11}/M^{-1}) = 4.4, log (K_{12}/M^{-2}) = 11.1; the 1:2 complex was assumed as being not emissive.

The decay of DOX fluorescence was monitored at 590 nm with excitation at 465 nm on the nanosecond scale. In the DOX alone solution the lifetime, assigned to the monomer, was found to be 1.02 ns (χ^2 = 1.03). Addition of pγ−CyD at various concentrations tends to slow down a little the decay rate but a monoexponential law still applies. In the presence of the polymer pγ−CyD (7×10^{-3} M in pγ−CyD_units) the measured lifetime is τ = 1.3 ns (χ^2 = 1.0), assigned to the complexed monomer, the dominant species in solution according to the binding analysis described below.

2.4.4 Global analysis of spectroscopic data

Global analysis based on SPECFIT/32 was applied to CD titration data of **Figure 2.13B**. The host concentration was expressed as pγ−CyD_unit concentration, the excess of the latter over the DOX concentration being > 4 in the whole range. Moreover the analysis assumed the DOX dimerization equilibrium with fixed constant, log (K_d/M^{-1}) = 4.8, and absolute CD spectra of the free DOX monomer and dimer species as determined in aqueous neutral buffer. The best fit corresponds to a complexation model with 1:1 and 1:2 pγ−CyD unit:DOX complexes in equilibrium with free DOX monomer, free DOX dimer and free pγ−CyD_unit. The optimized association constants were derived as log (K_{11}/M^{-1})= 3.3±0.2 and log(K_{12}/M^{-2}) = 8.7±0.3 (Durbin-Watson factor = 1.6). The individual CD spectra of the complexes are reported in **Figure 2.15A** together with the

47

spectra of the free DOX components. The concentration profiles of all the DOX species in solution are reported in **Figure 2.15B**. In **Figure 2.16A** the agreement between calculated and experimental ellipticity at key wavelengths can be appreciated.
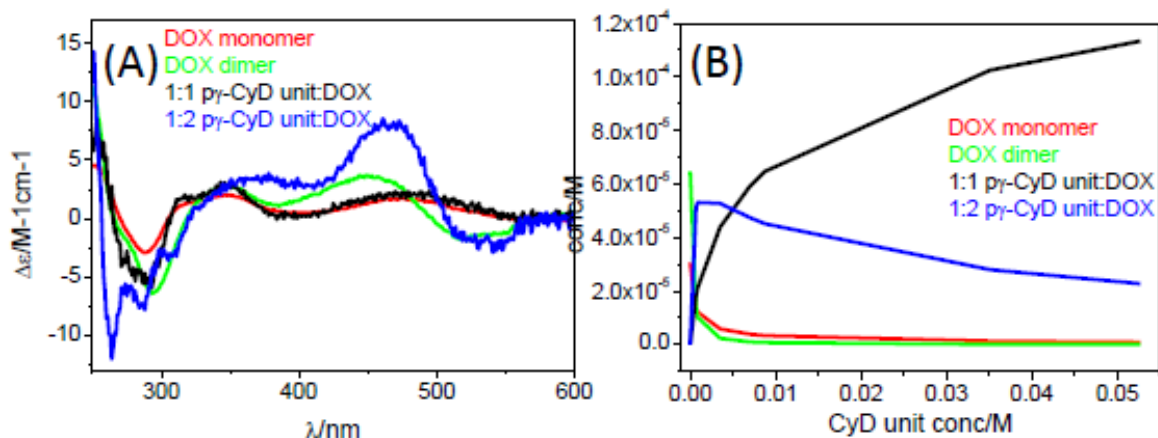
Figure 2.15 (**A**) CD absolute spectra of pγ−CyD unit:DOX complexes corresponding to log (K_{11}/M^{-1}) = 3.3 and log (K_{12}/M^{-2}) = 8.7 and of free species (**B**) concentration profiles of DOX species in solution.
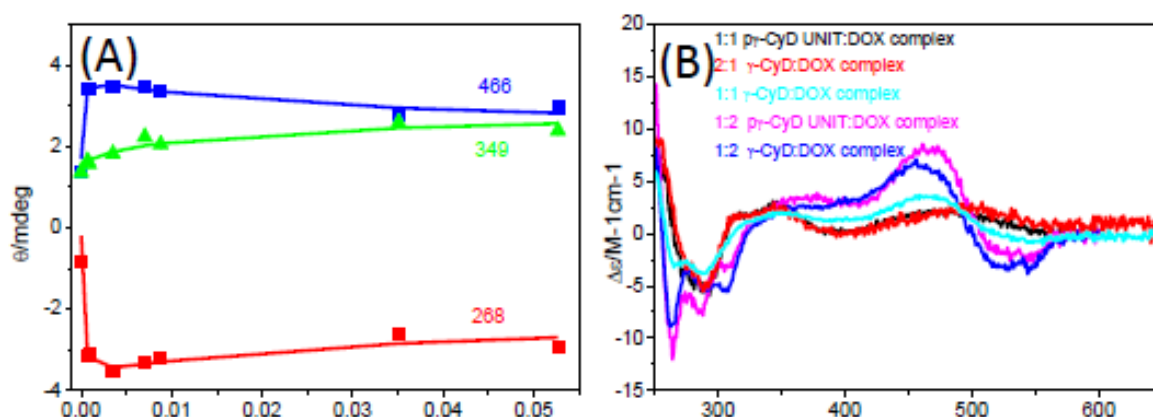
Figure 2.16 (**A**) Comparison of experimental (symbols) and calculated (line) data at representative wavelengths, corresponding to log (K_{11}/M^{-1}) = 3.3 and log (K_{12}/M^{-2}) = 8.7. (**B**) Comparison of spectra of pγ−CyD unit:DOX complexes with spectra of γ−CyD:DOX complexes.

A confirmation of the goodness of the binding model was obtained from global analysis of the fluorescence titration data in **Figure 2.14A**. We assumed that emission comes exclusively from monomeric DOX, either free or complexed, and again included the DOX dimerization equilibrium with fixed constant log K_d= 4.8. In the concentration range explored the excess of pγ−CyD unit over DOX is > 3. The association constants were optimized as log (K_{11}/M^{-1})= 4.4±0.1 and log(K_{12}/M^{-2}) = 11.1±0.1 (DW 1.1). The corresponding individual amplitudes for the free DOX monomer and the 1:1 pγ−CyD unit:DOX complex are shown in **Figure 2.14B**. In **Table 2.6** we

collect the association constants of DOX species with various CyD hosts, from this work and previous literature.

2.4.5 The binding process and the spectroscopic properties of the complexes.

With pγ−CyD unit/DOX molar ratios < 3-4 we evidenced a massive association of the hydrophobic drug   to the polymeric material to form multimolecular, possibly non specific, aggregates, characterized by "distorted" CD spectra (**Figure 2.13B, orange and cyano dashed spectra**) and no or very weak fluorescence (**Figure 2.14A, orange solid spectrum**). We omitted this phase of the binding process in our global analysis. At higher molar ratios   a more simple equilibrium model was shown to apply fairly well, with formation of pγ−CyD unit:DOX complexes of 1:1 and 1:2 stoichiometry, in equilibrium with free DOX monomer and dimer. The concentration profiles of all species in solution represented in **Figure 2.15B** indicate that DOX associates very efficiently to pγ−CyD both as monomer and as dimer. At increasing host concentrations a progressive decrease of the 1:2 complex concentration occurs, with the 1:1 complex becoming more and more favoured and finally resulting to be largely dominant (ca. 71% of DOX is associated as monomer and ca. 29% as dimer with pγ−CyD unit 5.3×10^{-2} M (pγ−CyD 3.6×10^{-3} M)). The locally high γ−CyD concentration and the polymer 3D organization likely play a role in this effect, as already observed in the epichlorohydrin crosslinked β-CyD polymer (pβ−CyD), where the three-dimensional nanoparticle structure proved to be able to disrupt the free DOX dimers present in solution converting them into polymer-bound monomers.

Note that of the natural CyDs, only γ−CyD forms inclusion complexes of significant stability with DOX. Consistently comparison of the association constants of the two polymeric hosts for monomeric DOX (**Table 2.6**) shows that the binding ability of the polymeric γ−CyD is larger than that of the polymeric β−CyD, reasonably due to inclusion of the bulky aglycone nucleus of DOX in the larger cavity. [32,56] Further, the electrostatic interactions between the positively charged DOX daunosamine moiety and the negatively charged carboxyl groups of the citric acid crosslinker may effectively contribute to the complex stability in the γ−CyD polymer. An informative comparison is also that with the association constants of the DOX complexes with natural γ−CyD. Clearly the polymeric structure considerably improves the binding ability of the pγ−CyD unit for both DOX monomer and dimer. Finally, for the pγ−CyD system it is worth comparing the association constants determined from CD and FL data. The values obtained with the latter technique are

higher by ca. 1-2 orders of magnitude. This result may be related to the lower DOX concentration used in the FL titration, resulting in higher monomer/dimer molar ratio in solution (19/81 in CD vs. 58/42 in FL). It may be reasonably hypothesized that the initial formation of the multimolecular polymer-DOX aggregates observed at low polymer concentrations makes the two experimental conditions to be not completely equivalent for the complexation equilibria to be further established.

Table 2.6 Association constants of DOX:CyD complexes in aqueous media at pH 7.4, at 22 °C, determined by global analysis of titration spectroscopic data with the SPCFIT/32 program, and relevant literature data .

DOX complexes	Log K	Units of K	Technique	Ref.
DOX$_2$ (DOX dimerization)	4.8 ± 0.1	M^{-1}	UV-vis	
pγ−CyD_unit:DOX 1:1	(3.3-3.4) ± 0.2 (4.0-4.4) ± 0.1	M^{-1}	CD FL	This work (Batch 1-batch 2)[a]
pγ−CyD_unit:DOX 1:2	(8.5-8.7) ± 0.3 (10.4-11.1) ± 0.1	M^{-2}	CD FL	This work (Batch 1-batch 2)[a]
pβ−CyD_unit:DOX 1:1	2.2 ± 0.1	M^{-1}	CD	
β−CD:DOX 1:1	2.1± 0.1 2.3 ± 0.1	M-1	UV-vis FL	32
γ−CyD:DOX 1:1	2.7 ± 0.2 2.3 ± 0.3	M^{-1}	CD FL	
γ−CyD:DOX 1:2	7.80± 0.04	M^{-2}	CD	
γ−CyD:DOX 2:1	4.4 ± 0.5 4.9 ± 0.1 4.9 ± 0.4	M^{-2}	CD FL UV-vis	
γ−CyD:DOX 2:2	10.48 ± 0.21	M^{-3}	CD	

[a] Range of values are relevant to different batches of the pγ−CyD host material.

The CD spectra of the pγ–CyD-DOX complexes are compared to those of the free species and the complexes with natural γ–CyD in **Figure 2.15A** and **2.16B**, respectively. The CD of the 1:2 pγ–CyD unit:DOX complex is qualitatively similar to that of the 1:2 γ-CyD:DOX complex in the visible region and exhibits common structure features at 265, 287 and 306 nm. The relative intensities of such UV negative bands are not the same in the two systems, possibly because of slightly different complexation mode of DOX within the two γ–CyD hosts. However it is worth observing that the binding model used to describe the association of DOX to the γ–CyD unit of the polymer neglects complexes higher order than 1:2, like for example the 2:2 complex which markedly shapes the CD in the UV region in the γ–CyD-DOX system. It is also interesting to notice that the CD spectrum of the 1:1 pγ–CyD unit:DOX complex is somewhat different from that of the DOX monomer in buffer and from that of the 1:1 γ–CyD:DOX complex, whereas is practically identical to the CD spectrum of the 2:1 γ–CyD:DOX complex. This suggests that DOX in the γ–CyD polymer is effectively protected from contact with bulk buffer at both the aglycone and the daunosamine moieties, similarly to the 2:1 γ–CyD:DOX species, which on the basis of Molecular Dynamics, was suggested to have both molecular moieties interacting with γ–CyD host units. It can be reasonably concluded that the 3D organization of the polymer provides a non aqueous character to the surroundings of most of the DOX units.

The fluorescence molar amplitudes (**Figure 2.14B**) give direct information on the environment experienced by DOX in the 1:1 complex. The 560 nm/595 nm intensity ratio probes the polarity of the environment of the emitting state. [42] The value decreases considerably from buffer (0.62) to the 1:1 complex (0.44), indicating the excited state of the drug in the polymer frame experiences a polarity similar to that of alcoholic media. As for the γ–CyD:DOX 1:1 complex, the proximity of the dihydroxyanthraquinone chromophore to the hydroxyl groups of the γ–CyD rim is inferred. As regards the emissive ability, the area under the molar amplitude profiles in **Figure 2.14B** is proportional to the emission quantum yield of the free (Φ_f) and complexed DOX monomer (Φ_b).

Free monomer and 1:1 complex appear to have quite similar emission quantum yield. Actually, using the value of Φ = 0.039 for DOX 1×10^{-5} M in neutral buffer at 22°C (see **chapter 5, Experimental)** and considering (i) the fractions of excitation light absorbed by the monomer and the dimer in buffer and the negligible contribution of the dimer to the steady state emission,[41] we calculated a value Φ_f = 0.058 for the free DOX monomer and Φ_b = 0.054 for the 1:1

pγ−CyD_unit:DOX complex. In **Table 2.7** the photophysical parameters of DOX species in various CyD media are resumed. We observe that neither k_r nor k_{nr} substantially change in any of the γ−CyD complexes compared to buffer ($k_r \approx$ 3-4×10^7 s^{-1} and $k_{nr} \approx$ 7-10×10^8 s^{-1}).

Table 2.7 Photophysical parameters of DOX in various media at pH 7.4, 22 °C

Samples	τ_f/10^{-9} S	Φ_f	k_r/10^7 S^{-1}	k_{nr}/10^8 S^{-1}
DOX 1×10^{-5} M in neutral buffer	1.0^a	0.039	3.9	9.6
γ−CyD:DOX 1:1 complex	~1.1^a	0.032	~2.9	~8.8
pβ−CyD_unit:DOX 1:1 complex	~1.5^b	0.13	~8.7	~5.8
pγ−CyD_unit:DOX 1:1 complex	~1.3^a	0.054	~4.1	~7.3

^{a}Mono-exponential decay. ^{b}Second lifetime component in a biexponential decay.

2.4.6 Uptake and distribution of DOX-pγ−CyD complex within MCF-7 tumor cells

Cell uptake of pγ-CyD-DOX complexes has been studied with time-resolved fluorescence confocal microscopy. The autofluorescence of DOX was used for this scope. **Figure 2.17A** and **2.17B** shows an intensity-based image for a MCF-7 cell line incubated for 1 hour with DOX 10 μM alone and with pγ-CyD (1.4 mg/ml, 98% DOX is associated to the polymer) in buffer. In the images obtained collecting fluorescence in the 500-550 nm range we can envisage the entire cell while in the orange and red image we only observe the nucleus. The confocal spectra (**Figure 2.17C**) obtained in correspondence of ROI located in the nucleus clearly evidence the presence of DOX in the nucleus, while in the cytoplasm autofluorescence mixes with DOX fluorescence. It can be concluded that in both conditions DOX enters the cell nuclei, where the spectral features of the drug emission are clearly recognizable. [55] This fact indicates preservation of the DOX molecular structure during both the uptake and the monitoring processes, irrespectively of the incubation conditions. For the sake of comparison we registered the fluorescence spectrum of a DOX aqueous solution on the confocal system (**Figure 2.17C**) . Even though there seems to be a more pronounced vibrational structure for DOX in cellular context, the differences are too small to draw conclusions on the location of DOX in the nucleus. We also performed time-resolved fluorescence

imaging exciting the DOX and DOX/ pγ-CyD incubated cells at 405 nm, the only pulsed laser source available on the system. We have to consider that in these conditions we cannot avoid excitation of intrinsic cell fluorophores. Time-resolved fluorescence detection was performed in the 565-605 nm range corresponding to the DOX maximum intensity in the fluorescence spectrum. Careful analysis started from the fit of the fluorescence decay of a ROI located in the nucleus with a biexponential function and yielded in all cases two lifetimes of 1.0 (25%) and 2.4 ns (75%) with χ^2 values of ca 1.0. We then calculated the histogram for the complete image and a four-exponential function was necessary to fit the decay with good χ^2 values fixing the 1.0 and 2.4 ns lifetimes (**Figure 2.17D**). Two more lifetimes of less importance were found, one shorter (ca. 250 ps) and one longer, both with negligible weight in the nucleus. The lifetime of 1 ns is the same as in buffer and can be ascribed to aqueous environments, whereas the lifetime of 2.4 ns is likely due to DOX associated to a biomolecule. The known mode of interaction of anthracyclines with DNA is intercalation of the dihydroxyanthraquinone moiety between two base pairs, with location of the sugar residue in minor groove.[57] This binding mode is associated to an hypochromic effect [55], decrease of the emission ability [24] and drastic shortening of the emission lifetime which becomes of a few ps. [21] So the longer-lived emission component of 2.4 ns cannot be attributed to DOX intercalated on DNA. We suggest it may pertain to the drug located in a hydrophobic pocket of a nuclear protein, where the lifetime is expected to be longer than in water, according to data reported in **Table 2.7** for DOX incorporated in pβ-CyD nanoparticles.
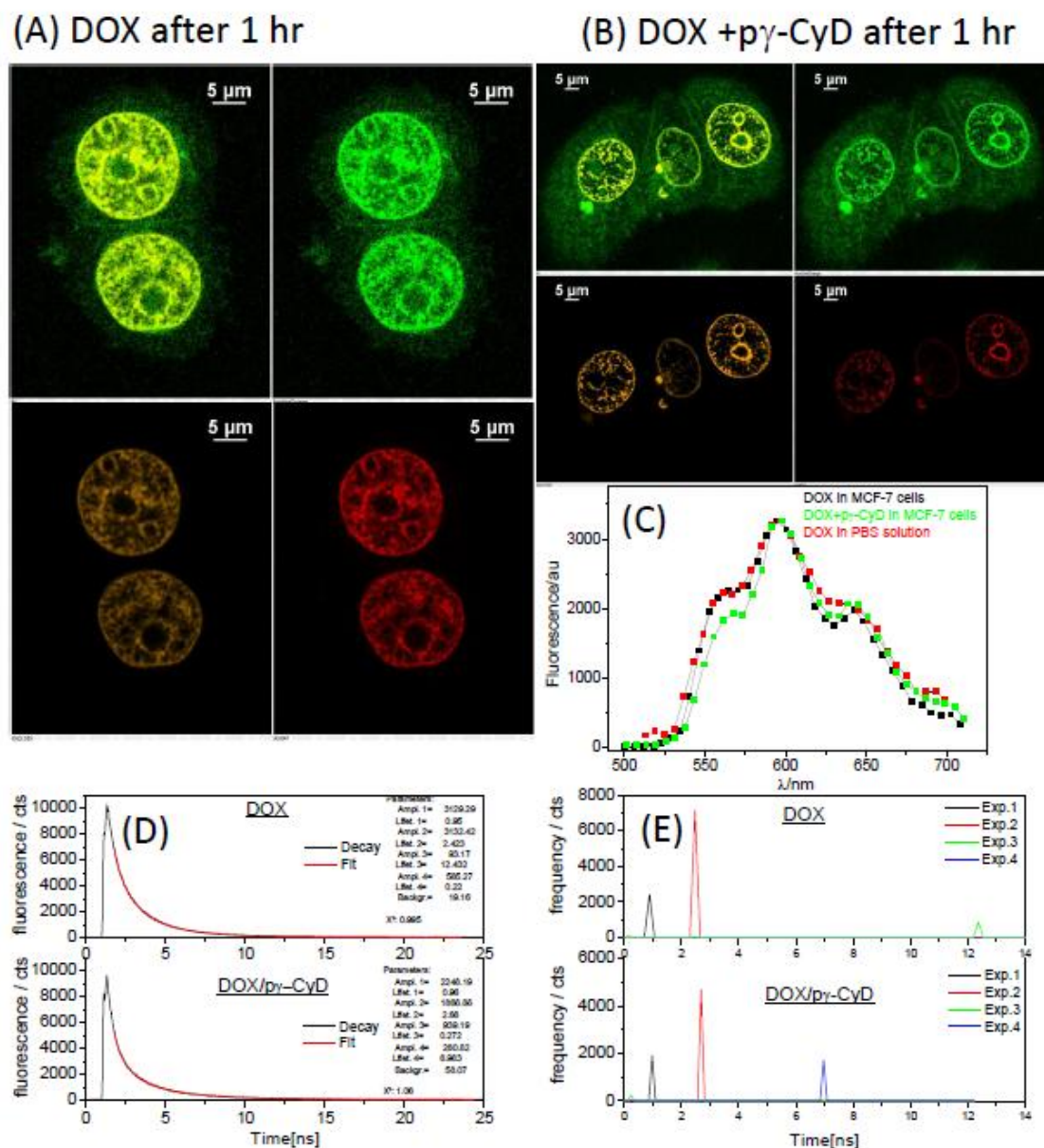
Figure 2.17 Confocal images of MCF-7 cells incubated for 1 h with (**A**) free DOX (10 μM) and (**B**) DOX (10 μM) + pγ-CyD (1.4 mg/ml);(top left) overlay of the images collecting fluorescence in the range 500-550, 570-620 and 665-735 nm. (**C**) Fluorescence spectra of DOX and pγ-CyD loaded DOX in MCF-7 cell line and DOX free in water, resolution of 6 nm per channel, DC2 used reflecting 488 nm. **D** and **E** are fitted decay and frequency histogram for the entire image in **A** and **B**.

2.4.7 Summary

In this study citric acid cross linked γ-cyclodextrin polymer (pγ–CyD) was successfully synthesized for the improved delivery of doxorubicin. Spectroscopic techniques of UV-Visible absorption, circular dichroism and fluorescence with multivariate global analysis of multiwavelength titration data revealed to be powerful tools to determine stability constants, ascertain the nature of the

interactions and probe the environment through the spectroscopic features of the bound drug. The complexation equilibria of pγ-CyD-DOX were analysed by taking into account of monomer-dimer equilibrium. The CD and fluorescence data clearly proved the formation of 1:1 and 1:2 pg-CyD unit:DOX complex with a very good association constants of $\log(K_{11}/M^{-1})$ from 3.3 to 4 and $\log(K_{12}/M^{-2})$ from 8.5 to 11. The concentration profiles provide evidence for the progressive monomerization of DOX at higher polymer concentrations. Confocal fluorescence imaging and spectral imaging of DOX-loaded pγ-CyD and free DOX, incubated in a MCF-7 cell line culture showed similar behaviour. In both cases DOX is uptaken into the nucleus without any degradation.

2.5 CONCLUSIONS

The results described in this chapter suggest that CyD-based polymeric systems hold great potential for the delivery of anthracycline anticancer drugs for enhanced therapeutic efficacy. These studies open up a new field of investigation aimed at adapting the synthetic strategies toward novel CyD polymers and/or copolymers endowed with suitable nanostructure for even more efficient interaction with DOX. In this context the application of spectroscopic techniques of UV-Visible absorption, circular dichroism and fluorescence with multivariate global analysis of multiwavelength titration data revealed to be powerful tools to determine stability constants, ascertain the nature of the interactions and probe the environment through the spectroscopic features of the bound drug.

REFERENCES

1. Weiss, R. B. The Anthracyclines - Will We Ever Find a Better Doxorubicin. *Seminars in Oncology* **1992,** *19*, 670-686.

2. Octavia, Y.; Tocchetti, C. G.; Gabrielson, K. L.; Janssens, S.; Crijns, H. J.; Moens, A. L. Doxorubicin-Induced Cardiomyopathy: From Molecular Mechanisms to Therapeutic Strategies. *J. Mol. Cell. Cardiol.* **2012,** *52*, 1213-1225.

3. Nitiss, J. L. Targeting DNA Topoisomerase Ii in Cancer Chemotherapy. *Nat. Rev. Cancer* **2009,** *9*, 338-350.

4. Pommier, Y.; Leo, E.; Zhang, H. L.; Marchand, C. DNA Topoisomerases and Their Poisoning by Anticancer and Antibacterial Drugs. *Chem. Biol.* **2010,** *17*, 421-433.

5. Tyleckova, J.; Hrabakova, R.; Mairychova, K.; Halada, P.; Radova, L.; Dzubak, P.; Hajduch, M.; Gadher, S. J.; Kovarova, H. Cancer Cell Response to Anthracyclines Effects: Mysteries of the Hidden

Proteins Associated with These Drugs. *International Journal of Molecular Sciences* **2012,** *13*, 15536-15564.

6. Senkus, E.; Jassem, J. Cardiovascular Effects of Systemic Cancer Treatment. *Cancer Treatment Reviews* **2011,** *37*, 300-311.

7. Khasraw, M.; Bell, R.; Dang, C. Epirubicin: Is It Like Doxorubicin in Breast Cancer? A Clinical Review. *Breast* **2012,** *21*, 142-149.

8. Minotti, G.; Menna, P.; Salvatorelli, E.; Cairo, G.; Gianni, L. Anthracyclines: Molecular Advances and Pharmacologic Developments in Antitumor Activity and Cardiotoxicity. *Pharmacological Reviews* **2004,** *56*, 185-229.

9. Cukierman, E.; Khan, D. R. The Benefits and Challenges Associated with the Use of Drug Delivery Systems in Cancer Therapy. *Biochem. Pharmacol.* **2010,** *80*, 762-770.

10. Yokoyama, M. Polymeric Micelles as a New Drug Carrier System and Their Required Considerations for Clinical Trials. *Expert Opinion on Drug Delivery* **2010,** *7*, 145-158.

11. Lammers, T. Improving the Efficacy of Combined Modality Anticancer Therapy Using Hpma Copolymer-Based Nanomedicine Formulations. *Adv. Drug Delivery Rev.* **2010,** *62*, 203-230.

12. Haag, R. Supramolecular Drug-Delivery Systems Based on Polymeric Core-Shell Architectures. *Angew. Chem. Int. Ed.* **2004,** *43*, 278-282.

13. Yallapu, M. M.; Foy, S. P.; Jain, T. K.; Labhasetwar, V. Peg-Functionalized Magnetic Nanoparticles for Drug Delivery and Magnetic Resonance Imaging Applications. *Pharm. Res.* **2010,** *27*, 2283-2295.

14. Horcajada, P.; Chalati, T.; Serre, C.; Gillet, B.; Sebrie, C.; Baati, T.; Eubank, J. F.; Heurtaux, D.; Clayette, P.; Kreuz, C.; Chang, J. S.; Hwang, Y. K.; Marsaud, V.; Bories, P. N.; Cynober, L.; Gil, S.; Ferey, G.; Couvreur, P.; Gref, R. Porous Metal-Organic-Framework Nanoscale Carriers as a Potential Platform for Drug Delivery and Imaging. *Nat. Mater.* **2010,** *9*, 172-178.

15. Davis, M. E.; Chen, Z.; Shin, D. M. Nanoparticle Therapeutics: An Emerging Treatment Modality for Cancer. *Nat. Rev. Drug Discovery* **2008,** *7*, 771-782.

16. Betancourt, T.; Brown, B.; Brannon-Peppas, L. Doxorubicin-Loaded Plga Nanoparticles by Nanoprecipitation: Preparation, Characterization and in Vitro Evaluation. *Nanomedicine* **2007,** *2*, 219-232.

17. Gordon, A. N.; Tonda, M.; Sun, S.; Rackoff, W.; Investigators, D. S.-.; Long-Term Survival Advantage for Women Treated with Pegylated Liposomal Doxorubicin Compared with Topotecan in a Phase 3 Randomized Study of Recurrent and Refractory Epithelial Ovarian Cancer. *Gynecologic Oncology* **2004,** *95*, 1-8.

18. Agrawal, P.; Barthwal, S. K.; Barthwal, R. Studies on Self-Aggregation of Anthracycline Drugs by Restrained Molecular Dynamics Approach Using Nuclear Magnetic Resonance Spectroscopy

Supported by Absorption, Fluorescence, Diffusion Ordered Spectroscopy and Mass Spectrometry. *Eur. J. Med. Chem.* **2009,** *44*, 1437-1451.

19. Nakanishi, T.; Fukushima, S.; Okamoto, K.; Suzuki, M.; Matsumura, Y.; Yokoyama, M.; Okano, T.; Sakurai, Y.; Kataoka, K. Development of the Polymer Micelle Carrier System for Doxorubicin. *J. Controlled Release* **2001,** *74*, 295-302.

20. Menozzi, M.; Valentini, L.; Vannini, E.; Arcamone, F. Self-Association of Doxorubicin and Related-Compounds in Aqueous-Solution. *J. Pharm. Sci.* **1984,** *73*, 766-770.

21. Fiallo, M. M. L.; Tayeb, H.; Suarato, A.; Garnier-Suillerot, A. Circular Dichroism Studies on Anthracycline Antitumor Compounds. Relationship between the Molecular Structure and the Spectroscopic Data. *J. Pharm. Sci.* **1998,** *87*, 967-975.

22. Gallois, L.; Fiallo, M.; Garnier-Suillerot, A. Comparison of the Interaction of Doxorubicin, Daunorubicin, Idarubicin and Idarubicinol with Large Unilamellar Vesicles - Circular Dichroism Study. *Biochimica Et Biophysica Acta-Biomembranes* **1998,** *1370*, 31-40.

23. Samori, B.; Rossi, A.; Pellerano, I. D.; Marconi, G.; Valentini, L.; Gioia, B.; Vigevani, A. Interactions between Drugs and Nucleic-Acids .1. Dichroic Studies of Doxorubicin, Daunorubicin, and Their Basic Chromophore, Quinizarin. *Journal of the Chemical Society-Perkin Transactions 2* **1987**, 1419-1426.

24. Rizzo, V.; Battistini, C.; Vigevani, A.; Sacchi, N.; Razzano, G.; Arcamone, F.; Garbesi, A.; Colonna, F.; Capobianco, M. L.; Tondelli, L. Association of Anthracyclines and Synthetic Hexanucleotides. Structural Factors Influencing Sequence Specificity. *J. Mol. Recognit.* **1989,** *2*, 132-141.

25. Walter, A.; Schutz, H.; Stutter, E. Interaction of Anthracycline Antibiotics with Bio-Polymers .7. Equilibrium Binding-Studies on the Interaction of Iremycin and DNA. *Int. J. Biol. Macromol.* **1983,** *5*, 351-355.

26. Cheng, J.; Khin, K. T.; Davis, M. E. Antitumor Activity of Beta-Cyclodextrin Polymer - Camptothecin Conjugates. *Mol. Pharm.* **2004,** *1*, 183-193.

27. Al-Omar, A.; Abdou, S.; De Robertis, L.; Marsura, A.; Finance, C. Complexation Study and Anticellular Activity Enhancement by Doxorubicin-Cyclodextrin Complexes on a Multidrug-Resistant Adenocarcinoma Cell Line. *Bioorg. Med. Chem. Lett.* **1999,** *9*, 1115-1120.

28. Grosse, P. Y.; Bressolle, F.; Pinguet, F. In Vitro Modulation of Doxorubicin and Docetaxel Antitumoral Activity by Methyl-Beta-Cyclodextrin. *European Journal of Cancer* **1998,** *34*, 168-174.

29. Grosse, P. Y.; Bressolle, F.; Pinguet, F. Antiproliferative Effect of Methyl-Beta-Cyclodextrin in Vitro and in Human Tumour Xenografted Athymic Nude Mice. *Br. J. Cancer* **1998,** *78*, 1165-1169.

30. Grosse, P. Y.; Bressolle, F.; Vago, P.; Simony-Lafontaine, J.; Radal, M.; Pinguet, F. Tumor Cell Membrane as a Potential Target for Methyl-Beta-Cyclodextrin. *Anticancer Res.* **1998,** *18*, 379-384.

31. Grosse, P. Y.; Bressolle, F.; Pinguet, F. Methyl-Beta-Cyclodextrin in Hl-60 Parental and Multidrug-Resistant Cancer Cell Lines: Effect on the Cytotoxic Activity and Intracellular Accumulation of Doxorubicin. *Cancer Chemotherapy and Pharmacology* **1997,** *40*, 489-494.

32. Husain, N.; Ndou, T. T.; Delapena, A. M.; Warner, I. M. Complexation of Doxorubicin with Beta-Cyclodextrins and Gamma-Cyclodextrins. *Appl. Spectrosc.* **1992,** *46*, 652-658.

33. Bekers, O.; Kettenesvandenbosch, J. J.; Vanhelden, S. P.; Seijkens, D.; Beijnen, J. H.; Bult, A.; Underberg, W. J. M. Inclusion Complex-Formation of Anthracycline Antibiotics with Cyclodextrins - a Proton Nuclear-Magnetic-Resonance and Molecular Modeling Study. *J. Inclusion Phenom.* **1991,** *11*, 185-193.

34. Bekers, O.; Beijnen, J. H.; Vis, B. J.; Suenaga, A.; Otagiri, M.; Bult, A.; Underberg, W. J. M. Effect of Cyclodextrin Complexation on the Chemical-Stability of Doxorubicin and Daunorubicin in Aqueous-Solutions. *Int. J. Pharm.* **1991,** *72*, 123-130.

35. Bekers, O.; Beijnen, J. H.; Otagiri, M.; Bult, A.; Underberg, W. J. M. Inclusion Complexation of Doxorubicin and Daunorubicin with Cyclodextrins. *J. Pharm. Biomed. Anal.* **1990,** *8*, 671-674.

36. Monnaert, V.; Betbeder, D.; Fenart, L.; Bricout, H.; Lenfant, A. M.; Landry, C.; Cecchelli, R.; Monflier, E.; Tilloy, S. Effects of Gamma- and Hydroxypropyl-Gamma-Cyclodextrins on the Transport of Doxorubicin across an in Vitro Model of Blood-Brain Barrier. *J. Pharmacol. Exp. Ther.* **2004,** *311*, 1115-1120.

37. Manet, I.; Manoli, F.; Zambelli, B.; Andreano, G.; Masi, A.; Cellai, L.; Monti, S. Affinity of the Anthracycline Antitumor Drugs Doxorubicin and Sabarubicin for Human Telomeric G-Quadruplex Structures. *Phys. Chem. Chem. Phys.* **2011,** *13*, 540-551.

38. Job, P. *Ann. Chim.* **1928,** *9*, 113-203.

39. Messori, L.; Temperini, C.; Piccioli, F.; Animati, F.; Di Bugno, C.; Orioli, P. Solution Chemistry and DNA Binding Properties of Men 10755, a Novel Disaccharide Analogue of Doxorubicin. *Bioorg. Med. Chem.* **2001,** *9*, 1815-1825.

40. Kiraly, R.; Martin, R. B. Metal-Ion Binding to Daunorubicin and Quinizarin. *Inorganica Chimica Acta-Bioinorganic Chemistry* **1982,** *67*, 13-18.

41. Changenet-Barret, P.; Gustavsson, T.; Markovitsi, D.; Manet, I.; Monti, S. Unravelling Molecular Mechanisms in the Fluorescence Spectra of Doxorubicin in Aqueous Solution by Femtosecond Fluorescence Spectroscopy. *Phys. Chem. Chem. Phys.* **2013,** *15*, 2937-2944.

42. Karukstis, K. K.; Thompson, E. H. Z.; Whiles, J. A.; Rosenfeld, R. J. Deciphering the Fluorescence Signature of Daunomycin and Doxorubicin. *Biophys. Chem.* **1998,** *73*, 249-263.

43. Similar lifetimes were also found with DOX 1.6E-4 M in both absence and presence of g-CyD 1.6E-2 M (DOX > 96% complexed in 2:2 stoichiometry)

44.   Monti, S.; Sortino, S. Photoprocesses of Photosensitizing Drugs within Cyclodextrin Cavities. *Chem. Soc. Rev.* **2002,** *31*, 287-300.

45.   Andreoni, A.; Land, E. J.; Malatesta, V.; McLean, A. J.; Truscott, T. G. Triplet-State Characteristics and Singlet Oxygen Generation Properties of Anthracyclines. *Biochim. Biophys. Acta* **1989,** *990*, 190-197.

46.   The spectra of the complexes are characterized by positive bands in the visible, as expected for monomeric DOX.   However in the 1:1 species a slightly negative CD at 550 nm is likely due to some 1:2 complex, not considered in the analysis neglecting the DOX dimer fraction present in solution.

47.   Daoud-Mahammed, S.; Agnihotri, S. A.; Bouchemal, K.; Kloeters, S.; Couvreur, P.; Gref, R. Efficient Loading and Controlled Release of Benzophenone-3 Entrapped into Self-Assembling Nanogels. *Current Nanoscience* **2010,** *6*, 654-665.

48.   Daoud-Mahammed, S.; Couvreur, P.; Amiel, C.; Besnard, M.; Appel, M.; Gref, R. Original Tamoxifen-Loaded Gels Containing Cyclodextrins: In Situ Self-Assembling Systems for Cancer Treatment. *Journal of Drug Delivery Science and Technology* **2004,** *14*, 51-55.

49.   Bouchemal, K.; Couvreur, P.; Daoud-Mahammed, S.; Poupaert, J.; Gref, R. A Comprehensive Study on the Inclusion Mechanism of Benzophenone into Supramolecular Nanoassemblies Prepared Using Two Water-Soluble Associative Polymers. *J. Therm. Anal. Calorim.* **2009,** *98*, 57-64.

50.   Daoud-Mahammed, S.; Couvreur, P.; Gref, R. Novel Self-Assembling Nanogels: Stability and Lyophilisation Studies. *Int. J. Pharm.* **2007,** *332*, 185-191.

51.   Daoud-Mahammed, S.; Grossiord, J. L.; Bergua, T.; Amiel, C.; Couvreur, P.; Gref, R. Self-Assembling Cyclodextrin Based Hydrogels for the Sustained Delivery of Hydrophobic Drugs. *Journal of Biomedical Materials Research Part A* **2008,** *86A*, 736-748.

52.   Renard, E.; Deratani, A.; Volet, G.; Sebille, B. Preparation and Characterization of Water Soluble High Molecular Weight Beta-Cyclodextrin-Epichlorohydrin Polymers. *Eur. Polym. J.* **1997,** *33*, 49-57.

53.   Gref, R.; Amiel, C.; Molinard, K.; Daoud-Mahammed, S.; Sebille, B.; Gillet, B.; Beloeil, J. C.; Ringard, C.; Rosilio, V.; Poupaert, J.; Couvreur, P. New Self-Assembled Nanogels Based on Host-Guest Interactions: Characterization and Drug Loading. *J. Controlled Release* **2006,** *111*, 316-324.

54.   Zhu, S. H.; Yan, L. M.; Ji, X. B.; Lu, W. C. Conformational Diversity of Anthracycline Anticancer Antibiotics: A Density Functional Theory Calculation. *Journal of Molecular Structure-Theochem* **2010,** *951*, 60-68.

55.   Angeloni, L.; Smulevich, G.; Marzocchi, M. P. Absorption, Fluorescence and Resonance Raman-Spectra of Adriamycin and Its Complex with DNA. *Spectrochimica Acta Part a-Molecular and Biomolecular Spectroscopy* **1982,** *38*, 213-217.

56.   Swiech, O.; Mieczkowska, A.; Chmurski, K.; Bilewicz, R. Intermolecular Interactions between Doxorubicin and Beta-Cyclodextrin 4-Methoxyphenol Conjugates *Journal of Physical Chemistry B* **2012,** *116*, 1765-1771

57.   Wang, A. H. J.; Ughetto, G.; Quigley, G. J.; Rich, A. Interactions between an Anthracycline Antibiotic and DNA - Molecular-Structure of Daunomycin Complexed to D(Cpgptpapcpg) at 1.2-a Resolution *Biochemistry* **1987,** *26*, 1152-1163.

SPECTROSCOPIC STUDIES ON DRUG ASSOCIATION TO METAL ORGANIC FRAMEWORK BASED SYSTEMS

As we have outlined in the introductory **Chapter 1** nanocarrier-drug combinations represent nowadays a promising approach to overcome pharmacological drawbacks of drugs, like low target specificity, rapid clearance, poor pharmacokinetics, severe side effects, low target susceptibility at the origin of multidrug resistance phenomena. A large variety of systems has been investigated, including polymeric nanoparticles, micelles, liposomes and various metal-based nanoassemblies.[1,2] This strategy has received particular attention for the delivery of anticancer drugs.[3,4]

Among the metal-based nanoassemblies, an innovative class of hybrid porous materials is represented by Metal Organic Frameworks (MOFs).[5] They are composed of metal ions or clusters (1D, 2D, or 3D) connected by multidendate organic ligands to form one-, two-, or three-dimensional arrays (See **Chapter 1, Figure 1.5**) and exhibit a crystalline structure with very high porosity and an enormous surface area. MOFs are highly tunable in terms of chemical composition eventually determining their crystal structure and dimensions of the pores as well as their physicochemical properties.[6] Because of their unique properties they found applications in a large variety of scientific and technological areas, mainly relevant to catalysis, separation, gas storage, imaging, sensing and magnetic and electrooptical materials.[7-10]

MOFs are presently receiving great attention also for biomedical applications.[8,11-16] In this frame, a new family of biodegradable and non cytotoxic materials, based on Fe(III) clusters and polycarboxylate ligands, has recently been synthesized with a "green" technology.[11,13,16-18] Thanks to their crystalline organization with large pores, these materials act as efficient "molecular sponges", rapidly soaking important amounts of hydrophilic and hydrophobic drugs directly from aqueous solution. Outstanding loading capability for a wide range of challenging drugs were

observed for some of them potentially opening the way to application in drug transport and delivery.[3]

3.1 INTERACTION OF DOXORUBICIN WITH MIL-100(Fe) NANOPARTICLES

Development of nanosized carriers for DOX (**Chapter 2, Scheme 2.1**) has attracted a lot of interest in the last decade as an approach to overcome the problems related to cardiotoxicity, cytotoxicity, selfaggregation and cell resistance. Cardiotoxicity is one the most serious side effects of anthracyclines in their clinical application.[19-22] Although the mechanisms of the toxic effects on cardiomyocytes are not fully understood, they are not the result of inhibition of DNA synthesis, because these cells do not replicate. A number of observations suggest that the interaction of anthracyclines with iron ions is of great importance. The redox state of iron ions can be converted between iron (II) and iron (III), with consequent generation of toxic reactive oxygen species (ROS) (**Scheme 3.1**), which cause DNA damage and induce apoptosis.
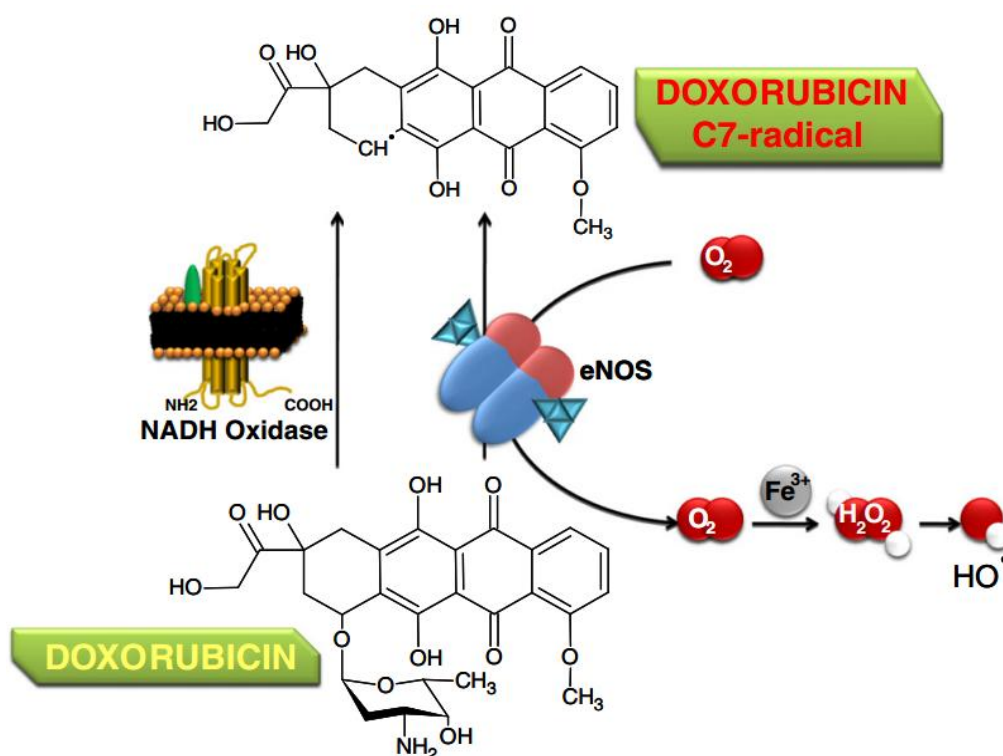
Scheme 3.1. Schematic illustration of molecular transformation of doxorubicin (adapted from ref [25]) .

Cardiac tissue is vulnerable to free radical damage because of the low activity of antioxidant enzyme systems in cardiomyocytes.[23] A strategy which has been proposed to decrease the redox

activity of anthracyclines is the delivery of them as metal complexes, especially as Fe(III) complexes.[24] In this context and, in general, for development of optimized carrier systems for anthracyclines, DOX has been successfully entrapped in MIL-100(Fe) (see **Scheme 3.2**). This hybrid material in aqueous medium is dispersed in particles of ca. 200 nm diameter (nanoMOFs). DOX was shown to be incorporated within the nanoMOF pores up to ca. 9 wt%. Release of the drug occurs over several days. [3]

In order to gain insights into the molecular recognition process that is at the basis of the DOX entrapment within the MIL-100(Fe) matrix, a characterization of nanoMOF-DOX complexes in aqueous medium via UV-Vis absorption, circular dichroism and fluorescence was performed.

3.1.1 Synthesis of MIL-100(Fe)

MIL-100 (Fe) was obtained by microwave-assisted hydrothermal synthesis from a mixture of iron chloride (8.97 mmol) and 1,3,5-benzenetricarboxylic acid (4.02 mmol) in 20 mL of deionized water, heating 6 min at 130°C under stirring. The power applied was 400 Watt (Mars-5, CEM, US: Power maximum output 1600 ± 240 Watts, Frequency at full power 2450 MHz). The as-synthesized nanoparticles were recovered by centrifugation (10 min, 10000 g). To remove the residual non reacted organic acid, they were washed in 50 mL of absolute ethanol and recovered by centrifugation (10 min, 10000 g). This activation step was repeated 6 times.

The obtained nano MOF architecture is as follows: the oxocentered trimers of Fe(III) octahedra is linked by benzene-1,3,5-tricarboxylate ligands (1,3,5 BTC) to form a hybrid supertetrahedra (ST) which assemble in a zeotype architecture (**Scheme 3.2**). This frame delimits very large pores (free diameters of 25 and 29 Å) accessible through pentagonal and hexagonal microporous windows (of ca. 5.5 and 8.6 Å). The mesoporous cages exhibit large surface area and pore volume (SBET up to 2400 m^{2}g^{-1} and Vp~1.2 cm^{3}g^{-1}). Fe(III) trimers in MIL-100 possess accessible coordinatively unsaturated sites (CUS), up to two per trimer (see **Scheme 3.3**), able to coordinate a wide range of polar species and drugs. [3,26] Molar absorption coefficients and binding constants in the present work are referred to the trimeric Fe(III) unit of MIL-100 (Fe) with structure formula Fe_3O (OH) $(H_2O)_2$ $[(CO_2)_3 (C_6H_3)]_3$ (in the dehydrated form).
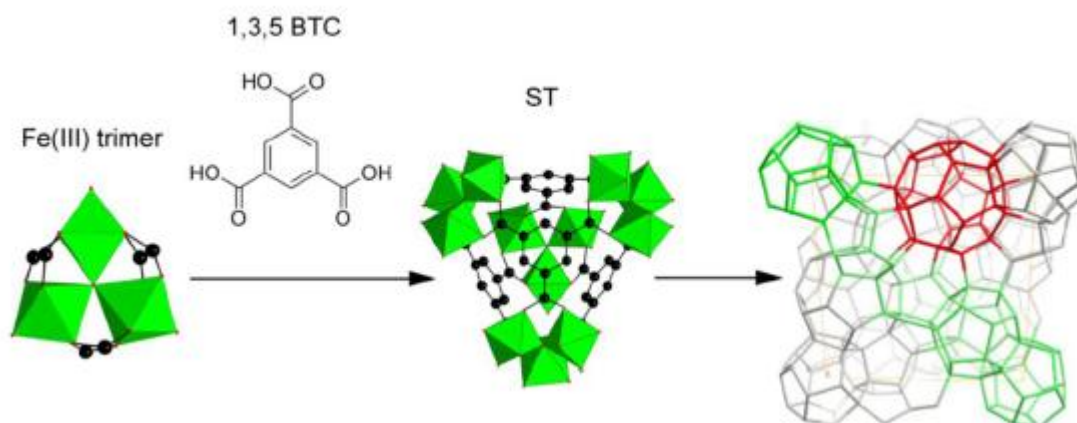
Scheme 3.2 Coordination between Fe(III) trimers and benzene-1,3,5-tricarboxylate ligands (1,3,5 BTC) leads to the formation of hybrid supertetrahedra (ST) that further assemble into a zeotypic architecture provided with two types of mesoporous cages with free diameters of 25 and 29 Å, accessible through pentagonal and hexagonal microporous windows of ca. 5.5 and 8.6 Å. From ref. [18]

3.1.2 Preparation of MIL-100(Fe) stock solution

MIL-100 (Fe) was stored in the dark at room temperature as EtOH wet material. An aliquot of it was dispersed in a few milliliters of ethanol. The suspension was centrifuged (10 min, 10000 rpm) and washed two times with tridistilled water and one time with TRIS buffer (10^{-2} M, pH 7.4) to remove traces of ethanol. Aliquots of the resulting centrifugate was suitably dispersed in TRIS buffer and used for the preparation of individual samples. MOF alone suspensions and mixtures with DOX were gently stirred for 30 min to attain a steady condition before use and were kept under stirring during the time span of all the experiments.

3.1.3 UV-Visible absorption

 The absorption spectra of the MIL-100 (Fe) MOF suspensions at various concentrations in TRIS buffer 0.01 M at pH 7.4 are shown in **Figure 3.1A**. The Fe-trimesate coordination band appears in the region 300-400 nm. An apparent molar absorption coefficient of 2900 $M^{-1}cm^{-1}$ was calculated at 330 nm from the linear dependence of the absorbance on the Fe(III) trimer content (mw 653). This value is in agreement with reported absorption coefficients of Fe-carboxylate LMCT absorption bands.[27] **Figure 3.1B** shows the absorption changes observed in a solution of DOX 1×10^{-4} M in TRIS buffer upon titration with the MOFs. On increasing the MOF content the absorbances increase in the 300-430 nm region and decrease at 430-520 nm shifting to the red, while a structured band arises in the 520-750 nm region.
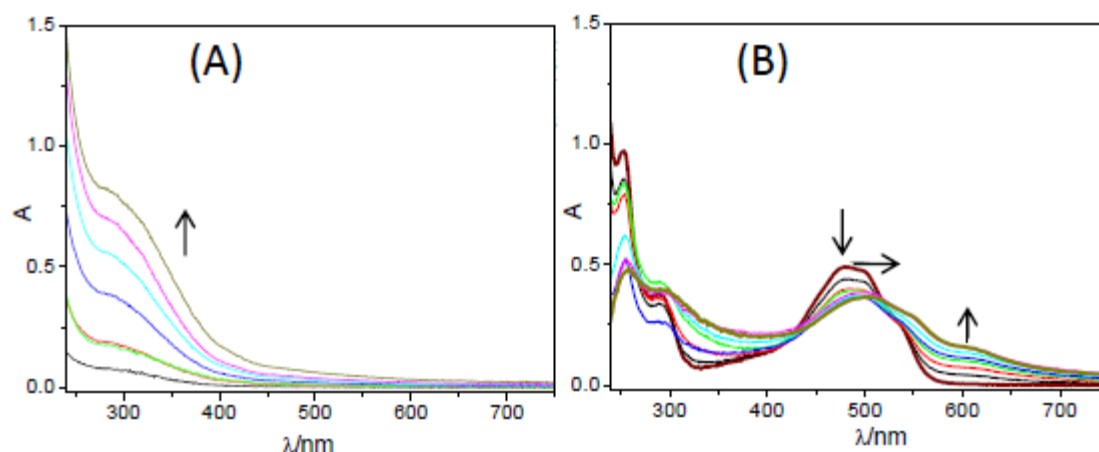
Figure 3.1 Absorption spectra of (**A**) MIL-100 (Fe), conc. 0.02-0.3 mg/ml(**B**) and MIL-100(Fe) in presence of DOX 1x10^{-4}M, in TRIS buffer, cell path length 0.5 cm and reference is TRIS buffer for MOF free and DOX free, MOF of same concentration for DOX-MOF mixture. Temperature 22 °C

In order to properly interpret these spectral changes it is worth recalling the spectrum of DOX alone in buffer (From **Chapter 2.1**). DOX displays bands at 288 and 480-500 nm, relevant to the two allowed $^{1}A \rightarrow {}^{1}L_a$ and $^{1}A \rightarrow {}^{1}L_b$ π-π* transitions polarized along the short and long axis of the dihydroxyanthraquinone moiety, respectively. The shoulder around 320-380 nm is associated to n-π* transitions of the three C=O groups in the molecule, partially forbidden by electric dipole. At neutral pH the aglycone part is neutral, whereas the daunosamine moiety is protonated.[28] Deprotonation of the phenolic OH groups of the aglycone ring B upon pH increase (pK values of ca. 10 for C_{11}-OH and >13 for C_6-OH),[29] produces changes in the UV-visible absorption quite similar to those of **Figure 3.1B**. Thus the spectral changes suggest that DOX incorporation into the MOF frame likely involves deprotonation of the drug molecule at the dihydroxyanthraquinone moiety. The absorption features of the DOX-MOF complexes are in complete agreement with those of DOX complexes and free Fe(III) ions, which bind to the dihydroxyanthraquinone moiety with release of one proton per bound molecule.[5,24] Another site for Fe(III) binding to DOX is the α-ketol group of the drug, suggested on basis of molecular modelling and the chemical degradation of the system.[30-32] On basis of the spectroscopic features and findings on the complex stability (see below) we safely conclude that most likely DOX coordinates to the Fe(III) centers of MOFs at the oxygen atoms in the positions 11 and 12 and/or 5 and 6 of the C and B rings (see **Chapter 2.1, Scheme 2.1**). Close inspection of **Figure 3.1B** evidences the presence of isosbestic points at 420 and 530 nm that are lost at MOF content > 0.1 mg/ml. This points to an incorporation process involving formation of more than one type of complexes.

Determination of the association constant. In order to estimate an apparent association constant (K_{ass}), we centrifuged several DOX-MOF mixtures for 20 min at 10000 rpm. Upon centrifugation free and complexed MOFs precipitated, whereas free DOX remained in the supernatant and was quantified by UV-Vis absorption using a molar absorption coefficient of 10800 M^{-1} cm^{-1} at 480 nm. A 1:1 stoichiometry was assumed and **Eqn 3.1** was used to calculate the dissociation constant K_{diss} = $1/K_{ass}$,

$$\text{[bound DOX]} = \tfrac{1}{2} \left(K_{diss} + x + c - ((K_{diss} + x + c)^2 - 4\, x\, c)^{1/2} \right) \qquad \textbf{(3.1)}$$

where and x and c are the total concentrations of Fe(III) trimeric unit and DOX, respectively. The experiment was carried out for DOX 1×10^{-4} M keeping the Fe(III) trimer concentration below 1.1×10^{-3} M (various MOF contents < 0.7 mg/ml, **Figure 3.2A**) . Quantification of the free DOX in the supernatant was performed (see **Figure 3.2B**). From the plot in the inset a value K_{ass} = (1.8$\pm$ 0.1)$\times 10^4$ M^{-1} was extracted. The quality of the best fit and the small error indicates that the assumed 1:1 model (one DOX molecule bound on average to one Fe(III) trimer) fairly well applies in the conditions of the experiment. The association constant is by 6-7 orders of magnitude lower than those reported for binding of free Fe(III) ions to DOX.[5] This is reasonably due to reduced DOX accessibility to Fe(III) trimers inside MOF pores considering the small dimension of 5.5 or 8.6 Å of the pore windows.
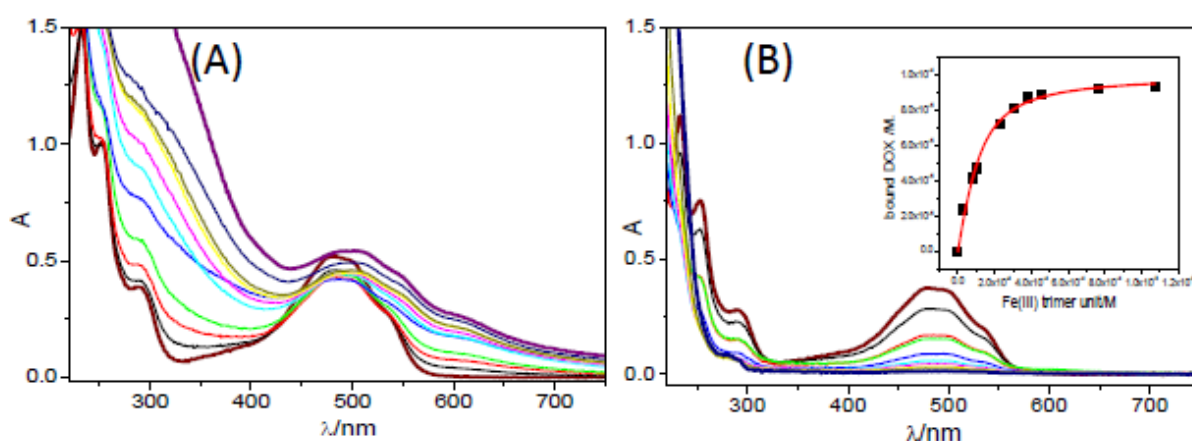
Figure 3.2 UV-vis absorption spectra of DOX (1×10^{-4}M) - MOF (0.02 to 0.7 mg/ml) mixtures in TRIS buffer (**A**) before centrifugation (**B**) after centrifugation (20 min, 10000 rpm), cell path length 0.5 cm, reference TRIS buffer, Temperature 22 °C. Inset of (B) is the plot for binding constant analysis with Eqn 3.1.

3.1.4 Circular dichroism

Circular dichroism further supports the described mode of DOX binding. The asymmetric carbon centers C7 and C9 configurations are of particular importance for the electronic transitions in the UV-Vis region (**Chapter 2, Scheme 2.1**).[28] The CD spectrum of DOX 1.0×10^{-4} M solution in neutral TRIS buffer is characterized by negative bands at ca. 290 nm and 500-550 nm and positive bands at ca. 250 nm, 350 nm and 450 nm. A positive-negative splitting of the dichroic signal in the 400-600 nm region is due to the presence of DOX in dimeric form. The negative component is weaker than the positive one and is barely observable in the present experimental conditions, despite dimer-like DOX should be predominant (a pK_d/M^{-1} = 4.8 was measured in neutral phosphate buffer, see **Chapter 2, section 2.1.1**).

The formation of the DOX-MOF complexes modifies the CD spectrum (**Figure 3.3**). On increasing the MOF content the bands at 250 nm and 350 nm decrease in intensity and a new positive, broad CD band arises at ca. 600-630 nm; the positive band at 450 nm shifts to red while the signal at 500-550 nm clearly becomes positive. These changes are similar to those observed for the association of DOX to free Fe (III) ions in aqueous medium[5] and confirm the formation of coordination bonds between the Fe(III) trimer and C and B rings of DOX. Since in the conditions of the experiments DOX is predominantly dimeric, the binding process can be represented according to **Scheme 3.3**, where the DOX_2 dimer dissociates and up to two monomer molecules access CUS of Fe(III) centers, replacing previously coordinated water molecules. This result is somehow expected since the DOX dimer is likely too large to pass the pore windows with the 5.5 and 8.6 Å dimensions.
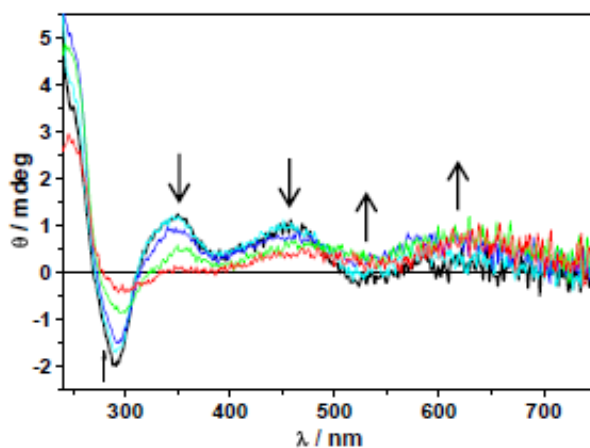
Figure 3.3 Circular dichroism spectra of DOX $(1 \times 10^{-4}M)$-MOF(0.03-0.7 mg/ml) mixtures inTRIS buffer, cell path length 0.2cm, Temperature 22 °C.
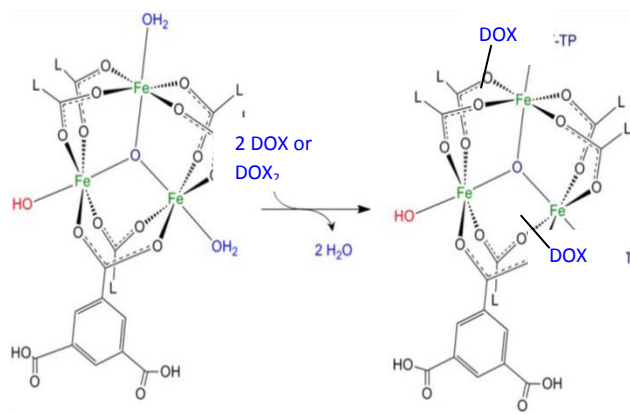
Scheme 3.3 Schematic representation of the MIL-100(Fe) structure and the DOX interaction. DOX_2 dimer dissociates and up to two monomeric molecules efficiently interact with the matrix by coordination to CUS, replacing the previously coordinated water molecules.

3.1.5 Fluorescence

The binding of DOX to MOFs was also studied by fluorescence. A DOX 2.0×10^{-5} M solution in TRIS buffer at pH 7.4 exhibits a structured fluorescence spectrum with λ_{max} = 590 nm (**Figure 3.4**). As we have previously mentioned, the emission comes from the DOX monomer and the decay is monoexponential with τ_1 = 1.0 ns (χ^2 = 1.02) and. Addition of increasing amounts of MOFs determines a progressive decrease of the fluorescence intensity with no change in either spectral shape or decay kinetics and points to a quenching process due to ground state complex formation. These findings are consistent with existing literature on the non fluorescent nature of Fe(III)-DOX conjugates, where DOX is in an essentially basic form, and further support that binding occurs on deprotonation of the hydroxyanthraquinone moiety. The operative mechanism for the DOX fluorescence quenching might in principle involve an electron transfer with formation of radicals in the system or efficient intersystem crossing to the triplet manifold in the excited complex. These hypotheses were not supported by nanosecond laser flash photolysis at λ_{exc} = 532 nm, which did not reveal any transient in the MIL-100 (Fe) suspension either alone or in mixtures with DOX. Back electron transfer on a subnanosecond time scale or population of an intrinsically non fluorescent excited state may be at the basis of the observed behaviour.

The decrease of the DOX fluorescence intensity on titration with the nanoMOFs can be used to determine an association constant. By applying **Eqn 3.2** to the data of **Figure 3.4**, corrected for the variation of the DOX absorbance at the non isosbestic excitation wavelength of 480 nm (plot of **Figure 3.4B**), a value $K_{ass}=1/K_{diss}$ = $(1.1\pm 0.1)\times10^{4}$ M^{-1} was extracted. This value is in

a reasonably good agreement with that obtained by the direct method based on UV-Visible absorption data, described in **Figure 3.4**

$$\Delta F/F_0 = (\Delta F/F_0)_{max}\, x\, /\, (K_d + x) \qquad\qquad\qquad (3.2)$$
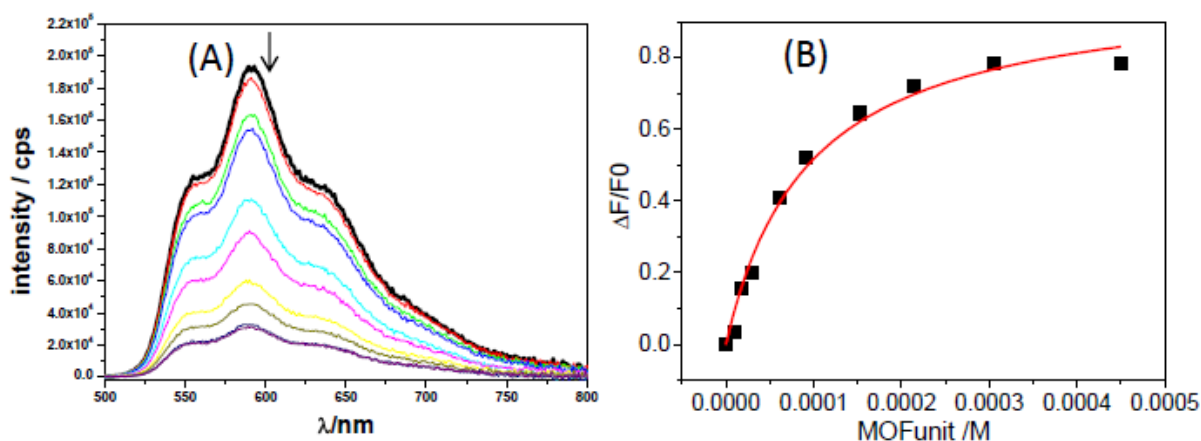
Figure 3.4 (**A**) Fluorescence spectra of DOX (2x10^{-6}M) in absence and presence of MOF (0.06 - 0.3mg/ml) in TRIS buffer, excitation at 480nm, cell path length 1cm, temperature 22 °C(**B**) Determination of binding constant by using **Eqn.3.2**.

3.1.6 Chemical stability of the MOF-DOX complexes.

The chemical stability of the MIL-100(Fe)-DOX complexes was checked by inspecting at the spectroscopic features after 24 h. Both the UV-Vis absorption and the CD spectra remained essentially unchanged, indicating absence of any appreciable degradation. Controversial data exist in literature on the stability of Fe(III)-DOX complexes in aqueous media. A selfreduction process resulting in a Fe(II)-DOX$^+$ species was proposed to occur at the α-ketol group with a rate constant of 0.076 min^{-1} in experimental conditions similar to those adopted in our experiments. This reaction was suggested to mediate mutagenic and cytotoxic effects in living cells through Fe based free radical-induced oxidative stress.[30-32] Although the importance of Fe(III) binding and related chemistry for DOX under pharmacological conditions was questioned,[5] Fe(III) complexes bearing three DOX molecules were shown to undergo chemical modification of one bound drug molecule out of three.[33] The fact that the MIL-100(Fe) matrix does not compromise the chemical stability of DOX represents a positive premise for the use of these MOFs as DOX carriers. Actually literatures on DOX release from the MOFs indicated that it occurs over several days by diffusion of the drug out of the pores.[3]

3.1.7 Summary

The spectroscopic data provided evidence for DOX entrapment upon disruption of drug selfassociated species, shed light on the binding mechanism and afforded the association constants for the formation of MOF unit-DOX 1:1 complex. The establishment of highly stable coordination bonds to Fe(III) at the hydroxyanthraquinone DOX sites was demonstrated. The present findings support positive perspectives for the use of porous Fe(III)-carboxylate MOFs as nanocarriers for DOX delivery.

3.2 INTERACTION OF AZIDOTHYMIDINE DERIVATIVES WITH MIL-100(Fe) NANOPARTICLES

3'-azido-3'-deoxythymidine (AZT, zidovudine, **Scheme 3.4**) is the first antiretroviral agent approved for the treatment of HIV/AIDS. It belongs to the class of the Nucleoside Reverse Transcriptase Inhibitors, prodrugs that convert into their pharmacologically active triphosphate form[34] by the action of cellular kinases and inhibit reverse transcriptase (RT), the key enzyme of HIV, responsible for the synthesis of proviral DNA.[35] One of the main problems of these drugs is their inefficient intracellular conversion, which limits their therapeutic efficacy and leads to the development of drug resistance and systemic toxicity.[36-38] Besides, direct administration of active triphosphorylated nucleoside analogs (NAs) is hampered by their poor stability and very low cellular uptake due to their highly hydrophilic character.[5,37,39] Over the past years, intensive research has been carried out to circumvent these drawbacks using nanocarriers to protect the active NAs triphosphate towards degradation and deliver them inside cells.[40-47]
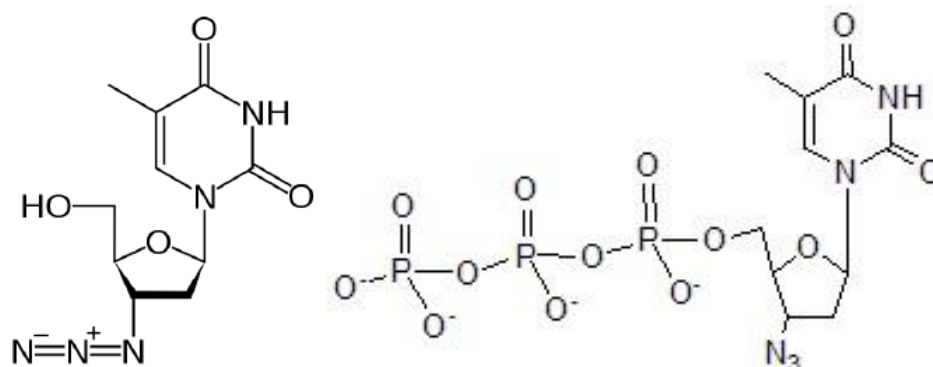
Scheme 3.4 Chemical structure of 3'-azido-3´- deoxythymidine (AZT) and 3´-azido-3´- deoxythymidine-5´-triphosphate (AZT-TP)

More recently, the nanoscale iron-trimesate MOF material MIL-100(Fe) showed very high azidothymidine triphosphate (AZT-TP) loading capability (up to 24 wt%) together with controlled release abilities.[3] In this chapter, we studied the mechanism of the complex interactions between AZT and its phosphate derivatives (azidothymidine monophosphate (AZT-MP) and azidothymidine triphospate (AZT-TP)) with MIL-100(Fe) nanoparticles (indicated in the following as "nanoMOFs", see also section 3.1) by using various spectroscopic techniques such as UV-vis absorption, circular dichroism (CD) and asymmetric flow field flow fractionation with multiangle light scattering (AF4-MALS).

3.2.1 UV-visible absorption

The UV-Vis absorption spectra of nanoMOFs (0.15 mg/mL, see section 3.1.2 for preparation of the suspensions), azidothymidine drugs (AZT, AZT-MP and AZT-TP (1 $\times 10^{-4}$ M)) and MOF-drug conjugated systems in water and in TRIS buffer, taken within one hour after preparation of the mixtures, are presented in **Figure 3.5A** and **3.5B**. In water, the absorption spectrum of empty nanoMOFs exhibited a maximum centered at ca. 240 nm, ascribed to $\pi,\pi*$ transitions of the trimesate ligands, whereas the broad absorption band at ca. 330 nm, extending into the visible region, is relevant to ligand-to-metal charge transfer transitions (LMCT) from trimesate ions to Fe(III) centres (**Figure 3.5A**).[48,49] In TRIS buffer at pH 7.4, the LMCT band of MOF appears to be red-shifted and weaker in intensity, features that may be due to change in polarity and/or specific interaction with the coordinating buffer molecules (**Figure 3.5B**). The azidothymidine derivatives, in both water and TRIS buffer, display an absorption band with maximum at 267 nm, assigned to the B_{2u} transition of the base conjugated ring.[50]

The interaction of the AZT derivatives with nanoMOFs can be understood by comparing the sum of the UV spectra of the individual components with the spectrum of the mixtures. The possible sites available for MOF binding are predominantly the carbonyl groups of the thymine moiety and the phosphate groups. Their role can be appreciated in the absorption bands of the mixtures at 267 nm and 330 nm, respectively. In the AZT-MOF system, both in water and in TRIS buffer, the sum of the individual spectra exactly matches the spectrum of the mixture. This fact points to a very weak interaction between AZT and MOF in both media as mentioned above. In contrast, the AZT phosphate derivatives in presence of MOFs exhibit non additive spectra with different features in water and in TRIS buffer. In water, the AZT-MP/MOF system shows an

absorption at 267 nm weaker than that of the sum of individual spectra, whereas no such difference is observed at 330 nm, in agreement with prevailing interaction of the azidothymidine moiety with MOF; on the other hand the AZT-TP/MOF system shows an intensified absorbance at 330 nm, but no change at 267 nm, consistent with a preferential interaction of the phosphate group with MOF.
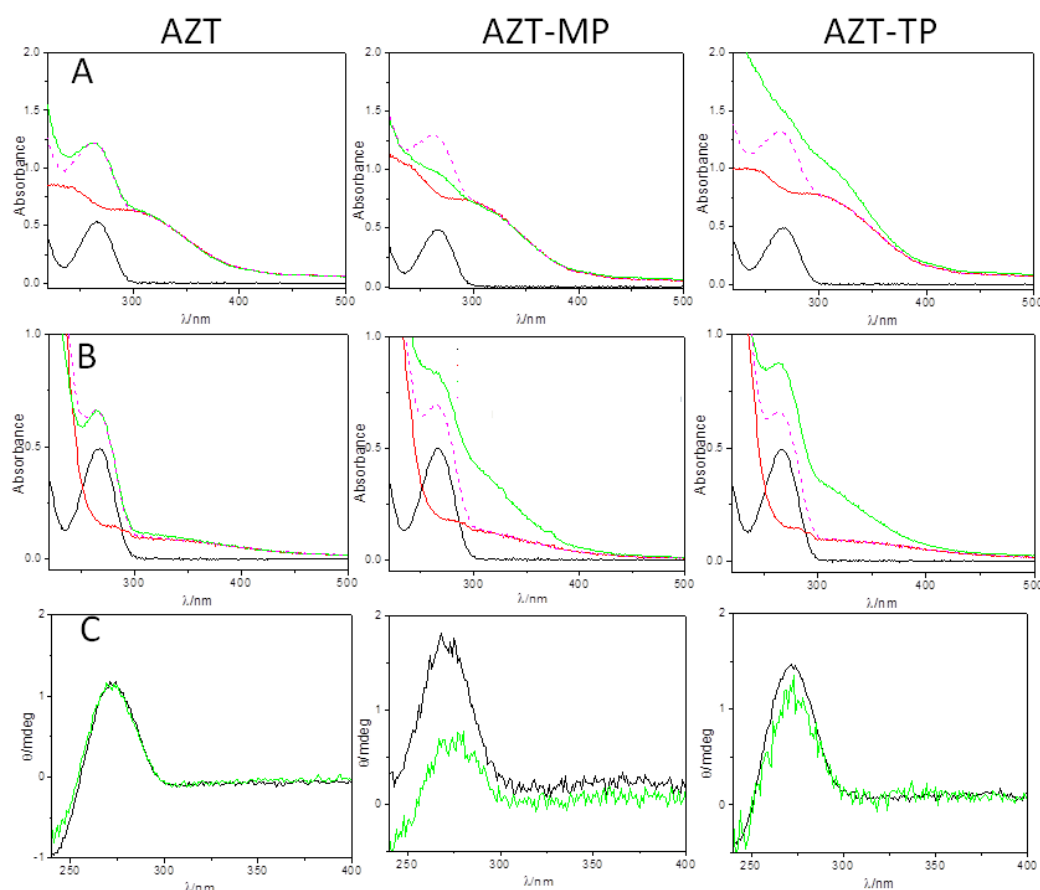
Figure 3.5 UV- vis absorption of MOF alone (0.15 mg/ml), drugs (AZT, AZT-MP and AZT-TP (1×10^{-4}M)) alone and in the mixtures with MOF (within 1hr from preparation), cell pathlength 0.5 cm: (**A**) in water; (**B**) in TRIS buffer (10^{-2} M, pH 7.4). (**C**) Circular dichroism spectra of drug (AZT, AZT-MP and AZT-TP (1×10^{-4}M) alone and in the mixtures with MOF in TRIS buffer (10^{-2}M, pH 7.4), cell pathlength 0.2 cm. Temp 22 °C.

Both AZT-MP and AZT-TP replace one water molecule to interact with the iron CUS. Our results show that the exchange is more favourable in the case of AZT-TP than for AZT-MP. In TRIS buffer, both the AZT-MP-MOF and the AZT-TP-MOF systems exhibit intensified absorption at 267 nm and at 330 nm, suggesting the interaction with MOF occurs via both the azidothymidine moiety and the phosphate groups. The differences in the binding mode observed in water between the two phosphorylated drugs tend to reduce with elapsing time, as shown by the absorption spectra of AZT-MP/MOF and AZT-TP/MOF systems after 24 hours in **Figure 3.6**.

Possibly, the displacement of one water molecule bound to iron CUS by AZT-TP and AZT-MP molecules is a kinetically controlled phenomenon.
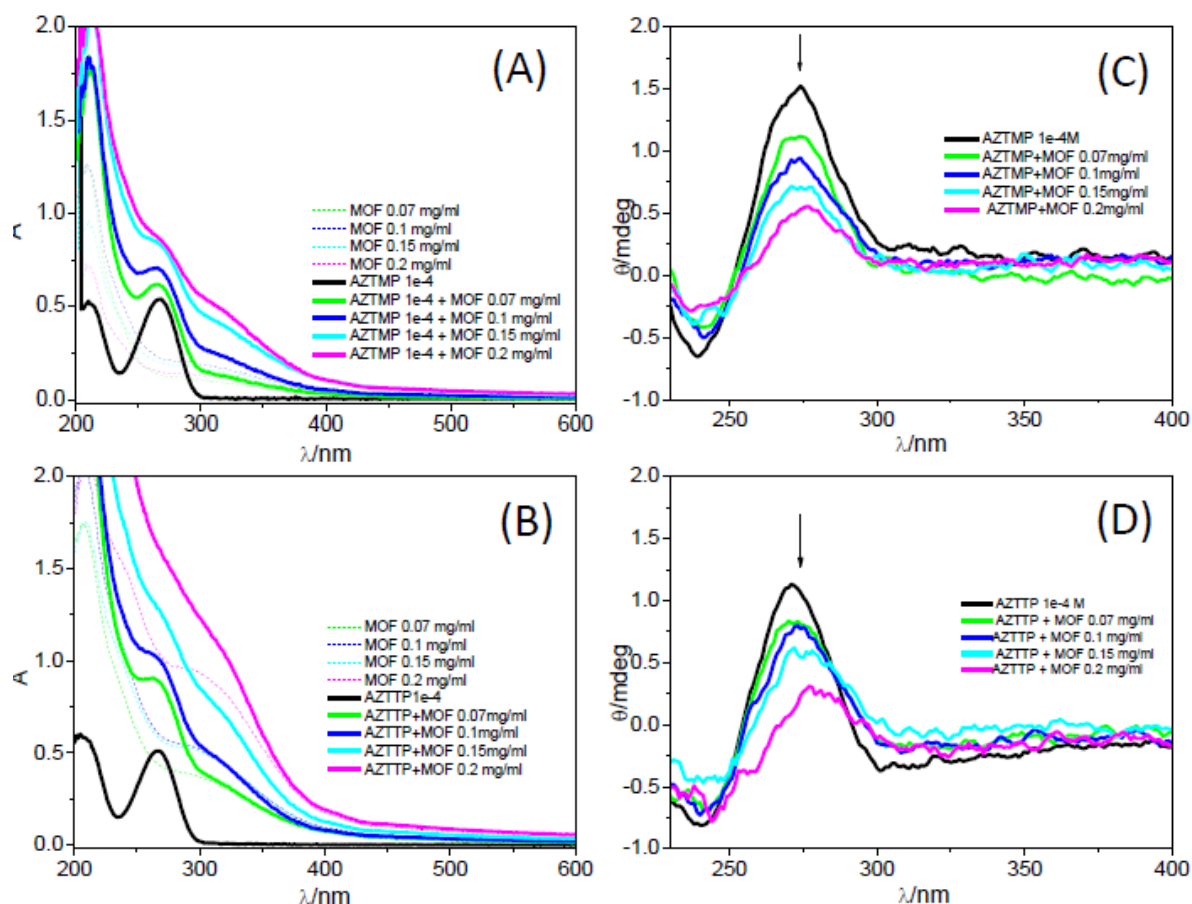
Figure 3.6 UV- vis absorption titration of (**A**) AZT-MP and (**B**) AZT-TP with MOF 0.07-0.2 mg/ml, in water, cell pathlength 0.5 cm; circular dichroism titration of (**C**) AZT-MP and (**D**) AZT-TP with MOF 0.07-0.2 mg/ml in water, cell pathlength 0.2 cm. T= 22 °C, after 24 hr from preparation. CD spectra have been smoothed.

3.2.2 Circular dichroism

The CD spectra of AZT, AZT-MP and AZT-TP (1 $\times 10^{-4}$ M) in TRIS buffer, are presented in **Figure 3.5C**. The ellipticity profiles of the free drugs are all characterized by a positive band at ca. 270 nm, assigned to the B_{2u} transition of the pyrimidine nucleoside moiety. In the presence of 0.15 mg/mL nanoMOFs the intensity of this band is markedly lower in the case of AZT-MP and only slightly lower in the case of AZT-TP, whereas it does not modify in the case of AZT. These findings can be understood by considering the dominant mechanism operative in the generation of the CD, i.e. the coupled oscillator mechanism, in which there is electric dipole-dipole coupling of the transition moments of the base chromophore with those of the ribose unit.   Both the sign and the

magnitude of a CD band depend on the nature and orientation of the sugar moieties relative to the transition dipole moment which pertains to the optical transition under consideration.[51,52] It is the overall conformation of the nucleoside to be responsible of the observed signal. In the case of the pyrimidine nucleosides the CD signal in the region of 270 nm   depends on the ratio between the of *syn* and *anti* conformations of the thymine base in the nucleoside at the equilibrium: a positive signal demonstrates the prevalence of the *anti* conformation, a negative band the prevalence of the *syn* conformation.[51]   The CD spectra of the free azidothymidine derivatives in **Figure 3.5C** demonstrate the prevalence of an *anti* conformation. The changes observed when they are complexed with nanoMOFs   can be explained by a modification in the ratio of *syn* and *anti* populations. Upon binding of AZT-MP and AZT-TP to nanoMOF the conformation of the sugar unit and, more likely, the torsion angle between the sugar and the thymine base may change favouring *syn* conformations. In the case of the AZT-MOF system, no change in the CD spectra was observed, in agreement with the lack of interaction between AZT and MOF revealed by the UV absorption spectra.

3.2.3 Determination of the association constant

Rough AZT-MP/AZT-TP-nanoMOF binding constants were estimated from UV absorption and CD titrations carried out at fixed concentration of the drug (1×10^{-4} M) varying the MOF solution content (from 0.02 mg/ml to 0.2 mg/ml). Expressing the MOF content in terms of Fe(III) trimer concentration (unit of mw 653) and assuming that there is only a 1:1 complex   involving AZT-MP/AZT-TP and the Fe (III) trimer in aqueous solutions, **Eqn 3.3** can be established.

drug + Fe(III) trimer $\rightleftharpoons$ drug: Fe(III) trimer   K   **(3.3)**
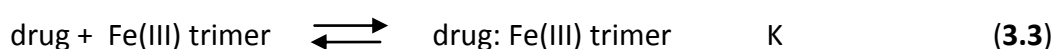
The association constant for the above equilibrium is represented by Eqn **3.4**

K = [drug : Fe(III) trimer]/[drug] [Fe(III) trimer]   **(3.4)**

According to the Benesi-Hildebrand method [53] a double reciprocal plot of $1/\Delta A_{330}$ vs. $1/$[Fe(III) trimer]$_{tot}$ is linear and the apparent binding constant can be obtained from the ratio of the intercept to the slope, in the hypothesis of excess of Fe(III) trimer over drug concentration.   This condition is not strictly fulfilled in the present case. However the double reciprocal plots always

have fairly good linearity (**Figure 3.7**), and, we believe, a rough estimation of the relative affinity of the two phosphorilated derivatives for the nanoMOF frame in water was obtained. A list of the apparent K values from different titration experiments are shown in **Table 3.1**. The values obtained from UV-visible absorption and circular dichroism data agree each other.
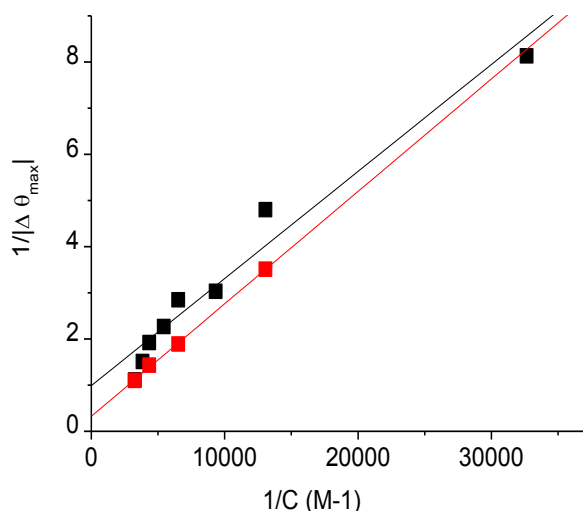
Figure 3.7 Plot of reciprocal $\Delta\theta$ at λ_{max} *vs.* reciprocal iron(III) trimer concentration after 24 h from preparation of the mixtures of AZT-TP (black) or AZT-MP (red) 1×10^{-4} M and MIL-100 nanoMOFs from 0.02 to 0.20 mg/mL, in water, cell path 0.2 cm, T = 22°C.

Table 3.1 Apparent binding constants (K, M^{-1}) for MOF-AZT-MP/AZT-TP complexes measured in water at 22°C.

Samples	K in water, after 24 hours (M^{-1})
AZT-TP	3100 [a]
	2930 [b]
AZT-MP	1340 [b]

[a] From UV-visible absorption data.
[b] From circular dichroism data.

3.2.4 Asymmetric Flow Field Flow Fractionation with Multi Angle Light Scattering (AF4-MALS)

Asymmetric Flow Field Flow Fractionation (AF4, See **chapter 5, Experimental**) is a promising technique for the size-separation of macromolecular solutions and particle suspensions over a broad dynamic range (1 nm-50 μm). The principle of this technique is based on the simultaneous

action of a flow stream of dispersing medium along a capillary channel and of a hydrodynamic field generated by a second stream of dispersing medium across the channel. In an AF4 run, scattered light from size separated nanoparticles is on-line delivered to the Multi Angle Light Scattering (MALS) detector, which records the signal at 18° different angles as a function of elution time. From the angular dependence of scattered light, the Root Mean Square (rms) radius (r_g) is then calculated. This quantity is defined as the average mean distance of the particle mass units from the center of gravity of the particle itself and represents the mass distribution of the particle from its center of gravity:

$$r_g{}^2 = \frac{\sum m_i r_i{}^2}{\sum m_i}$$

(3.5)

Data are reported as fractograms, i.e. the signal intensity at 90° with respect to the laser beam source plotted as a function of elution time. Small particles are eluted first, big particles are eluted last. The scattered dots represent the rms radius distribution, expressed in nm (right axis). A void peak due to unretained species, such as small molecules or very large (micron) particles can usually be observed (Figure 3.8) . This is an ideal methodology for the size-separation and characterization of complex nanoparticle samples.[54]
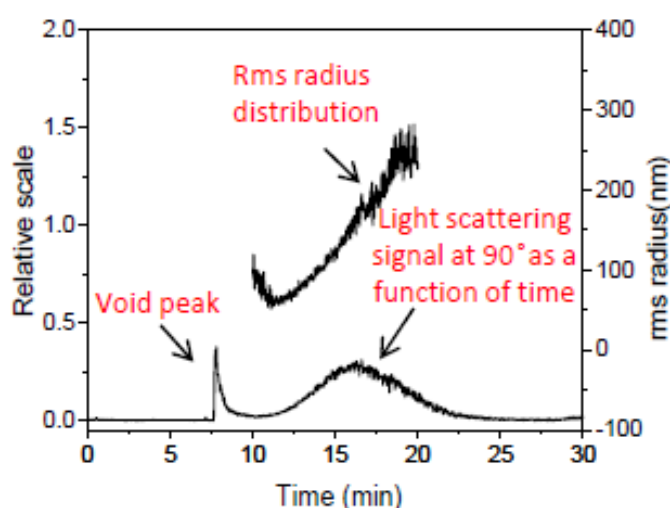
Figure 3.8 Schematic output of an AF4-MALS experiment

The AF4-MALS technique was applied to nanoMOFs alone (0.15mg/ml) and nanoMOF-drug conjugates (MOF 0.15 mg/ml+AZT/AZT-MP/AZT-TP $1x10^{-4}$M) both after one hour (fractogram

in **Figure 3.9**) and after 24 hours from preparation. The resulting particle size distribution is reported in **Table 3.2**. In the table the Zeta-potential of the nanoparticles is also reported. It can be noticed that the rms radius is the same both in absence and presence of AZT confirming this drug does not interact appreciably with the nanoMOF frame. With AZT-MP and AZT-TP there is increase of the rms radius with respect to the nude nanoMOF, indicating that binding of these drugs to the nanoMOFs occurs. With AZT-TP the increase of the rms radius is larger than with AZT-MP (ca. 16 nm vs. 10 nm). After 24 hours the rms radius of the drug loaded nanoMOFs remains constant indicating the loaded nanoparticles possess good stability over time and do not appreciably release the bound drugs.

From the AF4 fractogram (**Figure 3.9**), it can be noticed that, the retention behaviour is inverted, the bigger particles (nanoMOF/AZT-TP) eluted first. This could be attributed to the change in the Zeta potential of the loaded nanoMOFs due to drug binding (**Table 3.2**). NanoMOF/AZT-MP and nanoMOF/AZT-TP have a higher negative charge compared to nude nanoMOF and nanoMOF/AZT.   Because the channel membrane has a negative charge, nanoMOF/AZT-TP and nanoMOF/AZT-MP particles experienced more repulsion from the membrane and travelled closer to the centre of the parabolic flow, compared to nanoMOF and nanoMOF/AZT systems.
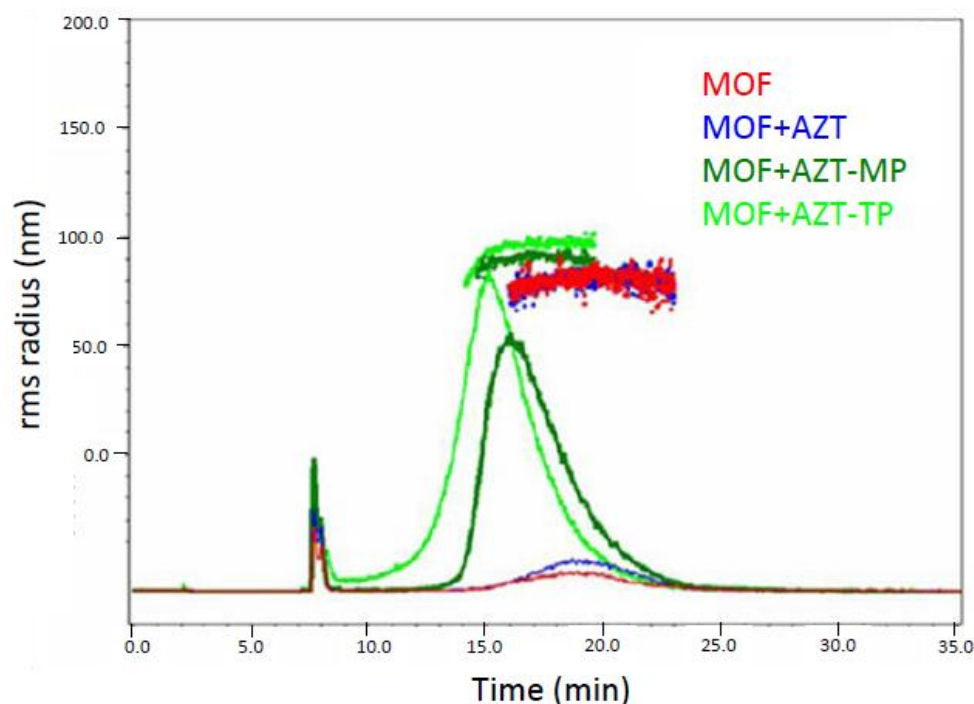
Figure 3.9 AF4-MALS fractogram of nude nanoMOF and nano MOF/drug conjugated systems within one hour from preparation.

Table 3.2 Root mean square radius distribution and zeta potential of nanoMOF free and nanoMOF/drug conjugates

Sample	rms (nm)		Zeta potential (mV)
	1 hour	24 hours	
MOF	80.79 ± 2.16	85.59 ± 2.22	+10
MOF/AZT	80.78 ± 2.19	80.37 ± 3.11	-
MOF/AZT-MP	90.19 ± 2.03	89.75 ± 2.22	-15
MOF/AZT-TP	96.78 ± 2.38	96.37 ± 2.21	-40

3.2.5 Summary

This study clearly evidenced the key role of the phosphate groups of nucleoside analogues for their effective encapsulation within MIL-100 (Fe). Indeed, in the absence of phosphate groups, as in the case of AZT, no significant interaction takes place with the MOF nanoparticles. After incubation with AZT-MP and AZT-TP in aqueous solutions an intensified absorption is observed in the system at around 330 nm, relevant to LMCT transitions. However, AZT-MP, bearing a single phosphate groups, showed lower nanoMOFs binding affinity as compared to the triphosphorylated AZT compound (K =1340 M^{-1} vs 2930 M^{-1}). The interaction with the nanoMOFs was ensured in both cases by the formation of iono-covalent bonds between the drugs phosphate groups and the nanoparticles available iron sites. AF4-MALS experiments provided information about homogeneity and stability of the system. An increased rms radius distribution is observed in drug-loaded nanoparticles keeping stable over 24 hours.

REFERENCES

1.   Brigger, I.; Dubernet, C.; Couvreur, P. Nanoparticles in Cancer Therapy and Diagnosis. *Adv. Drug Delivery Rev.* **2002,** *54*, 631-651.

2.   Riehemann, K.; Schneider, S. W.; Luger, T. A.; Godin, B.; Ferrari, M.; Fuchs, H. Nanomedicine-Challenge and Perspectives. *Angew. Chem. Int. Ed.* **2009,** *48*, 872-897.

3.   Horcajada, P.; Chalati, T.; Serre, C.; Gillet, B.; Sebrie, C.; Baati, T.; Eubank, J. F.; Heurtaux, D.; Clayette, P.; Kreuz, C.; Chang, J.-S.; Hwang, Y. K.; Marsaud, V.; Bories, P.-N.; Cynober, L.; Gil, S.;

Ferey, G.; Couvreur, P.; Gref, R. Porous Metal-Organic-Framework Nanoscale Carriers as a Potential Platform for Drug Delivery and Imaging. *Nat. Mater.* **2010,** *9*, 172-178.

4.   Cho, K.; Wang, X.; Nie, S.; Chen, Z.; Shin, D. M. Therapeutic Nanoparticles for Drug Delivery in Cancer. *Clinical Cancer Research* **2008,** *14*, 1310-1316.

5.   Fiallo, M. M. L.; Drechsel, H.; Garnier-Suillerot, A.; Matzanke, B. F.; Kozlowski, H. Solution Structure of Iron(Iii)-Anthracycline Complexes. *J. Med. Chem.* **1999,** *42*, 2844-2851.

6.   Meek, S. T.; Greathouse, J. A.; Allendorf, M. D. Metal-Organic Frameworks: A Rapidly Growing Class of Versatile Nanoporous Materials. *Adv. Mater.* **2011,** *23*, 249-267.

7.   Sanchez, C.; Julian, B.; Belleville, P.; Popall, M. Applications of Hybrid Organic-Inorganic Nanocomposites. *J. Mater. Chem.* **2005,** *15*, 3559-3592.

8.   Allendorf, M. D.; Bauer, C. A.; Bhakta, R. K.; Houk, R. J. T. Luminescent Metal-Organic Frameworks. *Chem. Soc. Rev.* **2009,** *38*, 1330-1352.

9.   Lee, J.; Farha, O. K.; Roberts, J.; Scheidt, K. A.; Nguyen, S. T.; Hupp, J. T. Metal-Organic Framework Materials as Catalysts. *Chem. Soc. Rev.* **2009,** *38*, 1450-1459.

10.   Zhou, H. C.; Long, J. R.; Yaghi, O. M. Introduction to Metal-Organic Frameworks. *Chem. Rev.* **2012,** *112*, 673-674.

11.   Hinks, N. J.; McKinlay, A. C.; Xiao, B.; Wheatley, P. S.; Morris, R. E. Metal Organic Frameworks as No Delivery Materials for Biological Applications. *Microporous Mesoporous Mater.* **2008,** *129*, 330-334.

12.   McKinlay, A. C.; Morris, R. E.; Horcajada, P.; Ferey, G.; Gref, R.; Couvreur, P.; Serre, C. Biomofs: Metal-Organic Frameworks for Biological and Medical Applications. *Angew. Chem. Int. Ed.* **2010,** *49*, 6260-6266.

13.   Miller, S. R.; Heurtaux, D.; Baati, T.; Horcajada, P.; Greneche, J.-M.; Serre, C. Biodegradable Therapeutic Mofs for the Delivery of Bioactive Molecules. *Chem. Commun.* **2010,** *46*, 4526-4528.

14.   Chen, B.; Xiang, S.; Qian, G. Metal-Organic Frameworks with Functional Pores for Recognition of Small Molecules. *Acc. Chem. Res* **2010,** *43*, 1115-1124.

15.   Huxford, R. C.; Della Rocca, J.; Lin, W. Metal-Organic Frameworks as Potential Drug Carriers. *Curr. Opin. Chem. Biol.* **2010,** *14*, 262-268.

16.   Horcajada, P.; Gref, R.; Baati, T.; Allan, P. K.; Maurin, G.; Couvreur, P.; Ferey, G.; Morris, R. E.; Serre, C. Metal-Organic Frameworks in Biomedicine. *Chem. Rev.* **2012,** *112*, 1232-1268.

17.   Horcajada, P.; Serre, C.; Vallet-Regi, M.; Sebban, M.; Taulelle, F.; Ferey, G. Metal-Organic Frameworks as Efficient Materials for Drug Delivery. *Angew. Chem. Int. Ed.* **2006,** *45*, 5974-5978.

18.   Horcajada, P.; Surble, S.; Serre, C.; Hong, D.-Y.; Seo, Y.-K.; Chang, J.-S.; Greneche, J.-M.; Margiolaki, I.; Ferey, G. Synthesis and Catalytic Properties of Mil-100(Fe), an Iron(Iii) Carboxylate with Large Pores. *Chem. Commun.* **2007**, 2820-2822.

19.   Beretta, G. L.; Zunino, F., Molecular Mechanisms of Anthracycline Activity. In *Anthracycline Chemistry and Biology Ii: Mode of Action, Clinical Aspects and New Drugs*, Springer-Verlag Berlin: Berlin, 2008; Vol. 283, pp 1-19.

20.   Dalmark, M.; Storm, H. H. A Fickian Diffusion Transport Process with Features of Transport Catalysis-Doxorubicin Transport in Human Red-Blood-Cells *Journal of General Physiology* **1981,** *78*, 349-364.

21.   Krishna, R.; Mayer, L. D. Multidrug Resistance (Mdr) in Cancer - Mechanisms, Reversal Using Modulators of Mdr and the Role of Mdr Modulators in Influencing the Pharmacokinetics of Anticancer Drugs. *Eur. J. Pharm. Sci.* **2000,** *11*, 265-283.

22.   Minotti, G.; Menna, P.; Salvatorelli, E.; Cairo, G.; Gianni, L. Anthracyclines: Molecular Advances and Pharmacologic Developments in Antitumor Activity and Cardiotoxicity. *Pharmacological Reviews* **2004,** *56*, 185-229.

23.   Kizek, R.; Adam, V.; Hrabeta, J.; Eckschlager, T.; Smutny, S.; Burda, J. V.; Frei, E.; Stiborova, M. Anthracyclines and Ellipticines as DNA-Damaging Anticancer Drugs: Recent Advances. *Pharmacol. Ther.* **2012,** *133*, 26-39.

24.   Beraldo, H.; Garnier-Suillerot, A.; Tosi, L.; Lavelle, F. Iron(Iii) Adriamycin and Iron(Iii) Daunorubicin Complexes - Physicochemical Characteristics, Interaction with DNA, and Antitumor-Activity. *Biochemistry* **1985,** *24*, 284-289.

25.   Octavia, Y.; Tocchetti, C. G.; Gabrielson, K. L.; Janssens, S.; Crijns, H. J.; Moens, A. L. Doxorubicin-Induced Cardiomyopathy: From Molecular Mechanisms to Therapeutic Strategies. *J. Mol. Cell. Cardiol.* **2012,** *52*, 1213-1225.

26.   Canioni, R.; Roch-Marchal, C.; Secheresse, F.; Horcajada, P.; Serre, C.; Hardi-Dan, M.; Ferey, G.; Greneche, J.-M.; Lefebvre, F.; Chang, J.-S.; Hwang, Y.-K.; Lebedev, O.; Turner, S.; Van Tendeloo, G. Stable Polyoxometalate Insertion within the Mesoporous Metal Organic Framework Mil-100(Fe). *J. Mater. Chem.* **2011,** *21*, 1226-1233.

27.   Glebov, E. M.; Pozdnyakov, I. P.; Grivin, V. P.; Plyusnin, V. F.; Zhang, X.; Wu, F.; Deng, N. Intermediates in Photochemistry of Fe(Iii) Complexes with Carboxylic Acids in Aqueous Solutions. *Photochem. Photobiol. Sci.* **2011,** *10*, 425-430.

28.   Gallois, L.; Fiallo, M.; Garnier-Suillerot, A. Comparison of the Interaction of Doxorubicin, Daunorubicin, Idarubicin and Idarubicinol with Large Unilamellar Vesicles - Circular Dichroism Study. *Biochimica Et Biophysica Acta-Biomembranes* **1998,** *1370*, 31-40.

29.   Kiraly, R.; Martin, R. B. Metal-Ion Binding to Daunorubicin and Quinizarin. *Inorganica Chimica Acta-Bioinorganic Chemistry* **1982,** *67*, 13-18.

30.   Hasinoff, B. B. Self-Reduction of the Iron(Iii)-Doxorubicin Complex. *Free Radical Biology and Medicine* **1989,** *7*, 583-593.

31.   Malisza, K. L.; Hasinoff, B. B. Production of Hydroxyl Radical by Iron(Iii)-Anthraquinone Complexes through Self-Reduction and through Reductive Activation by the Xanthine-Oxidase Hypoxanthine System. *Arch. Biochem. Biophys.* **1995,** *321*, 51-60.

32.   Eizaguirre, A.; Yanez, M.; Eriksson, L. A. Stability and Iron Coordination in DNA Adducts of Anthracycline Based Anti-Cancer Drugs. *Phys. Chem. Chem. Phys.* **2012,** *14*, 12505-12514.

33.   Fiallo, M.; Laigle, A.; Borrel, M. N.; Garnier-Suillerot, A. Accumulation of Degradation Products of Doxorubicin and Pirarubicin Formed in Cell Culture Medium within Sensitive and Resistant Cells. *Biochemistry* **1993,** *45*, 659-665.

34.   Furman, P. A.; Fyfe, J. A.; St Clair, M. H.; Weinhold, K.; Rideout, J. L.; Freeman, G. A.; Lehrman, S. N.; Bolognesi, D. P.; Broder, S.; Mitsuya, H. Phosphorylation of 3'-Azido-3'-Deoxythymidine and Selective Interaction of the 5'-Triphosphate with Human Immunodeficiency Virus Reverse Transcriptase. *P. Natl. Acad. Sci. U. S. A.* **1986,** *83*, 8333-8337.

35.   Cihlar, T.; Ray, A. S. Nucleoside and Nucleotide Hiv Reverse Transcriptase Inhibitors: 25 Years after Zidovudine. *Antiviral Res.* **2010,** *85*, 39-58.

36.   Balzarini, J.; Herdewijn, P.; De Clercq, E. Differential Patterns of Intracellular Metabolism of 2',3'-Didehydro-2',3'-Dideoxythymidine and 3'-Azido-2',3'-Dideoxythymidine, Two Potent Anti-Human Immunodeficiency Virus Compounds. *J. Biol. Chem.* **1989,** *264*, 6127-6133.

37.   Kukhanova, M.; Krayevsky, A.; Prusoff, W.; Cheng, Y. C. Design of Anti-Hiv Compounds from Nucleoside to Nucleoside 5-Triphosphate Analogs. Problems and Perspectives. *Curr. Pharm. Des.* **2000,** *6*, 585-598.

38.   Törnevik, Y.; Ullman, B.; Balzarini, J.; Wahren, B.; Eriksson, S. Cytotoxicity of 3'-Azido-3'-Deoxythymidine Correlates with 3'-Azidothymidine-5'-Monophosphate (Aztmp) Levels, Whereas Antihuman Immunodeficiency Virus (Hiv) Activity Correlates with 3'-Azidothymidine-5'-Triphosphate (Azttp) Levels in Cultured Cem T-Lymphoblastoid Cells. *Biochem. Pharmacol.* **1995,** *49*, 829-837.

39.   Loke, S. L.; Stein, C. A.; Zhang, X. H.; Mori, K.; Nakanishi, M.; Subasinghe, C.; Cohen, J. S.; Neckers, L. M. Characterization of Oligonucleotide Transport into Living Cells. *Proc. Natl. Acad. Sci. U.S.A.* **1989,** *86*, 3474-3478.

40.   Hillaireau, H.; Couvreur, P. Nanoencapsulation of Antiviral Nucleotide Analogs. *Journal of Drug Delivery Science and Technology* **2009,** *19*, 385-390.

41.   Hillaireau, H.; Le Doan, T.; Appel, M.; Couvreur, P. Hybrid Polymer Nanocapsules Enhance in Vitro Delivery of Azidothymidine-Triphosphate to Macrophages. *J. Controlled Release* **2006,** *116*, 346-352.

42. Hillaireau, H.; Le Doan, T.; Chacun, H.; Janin, J.; Couvreur, P. Encapsulation of Mono-and Oligo-Nucleotides into Aqueous-Core Nanocapsules in Presence of Various Water-Soluble Polymers. *Int. J. Pharm.* **2007,** *331*, 148-152.

43. Kohli, E.; Han, H. Y.; Zeman, A. D.; Vinogradov, S. V. Formulations of Biodegradable Nanogel Carriers with 5'-Triphosphates of Nucleoside Analogs That Display a Reduced Cytotoxicity and Enhanced Drug Activity. *J. Controlled Release* **2007,** *121*, 19-27.

44. Saiyed, Z. M.; Gandhi, N. H.; Nair, M. P. N. Azt 5'-Triphosphate Nanoformulation Suppresses Human Immunodeficiency Virus Type 1 Replication in Peripheral Blood Mononuclear Cells. *Journal of Neurovirology* **2009,** *15*, 343-347.

45. Saiyed, Z. M.; Gandhi, N. H.; Nair, M. P. N. Magnetic Nanoformulation of Azidothymidine 5'-Triphosphate for Targeted Delivery across the Blood–Brain Barrier. *International journal of nanomedicine* **2010,** *5*, 157.

46. Vinogradov, S. V.; Kabanov, A. V. In *Synthesis of Nanogel Carriers for Delivery of Active Phosphorylated Nucleoside Analogues*, 2004; NIH Public Access: 2004; p 296.

47. Vinogradov, S. V.; Poluektova, L. Y.; Makarov, E.; Gerson, T.; Senanayake, M. T. Nano-Nrtis: Efficient Inhibitors of Hiv Type-1 in Macrophages with a Reduced Mitochondrial Toxicity. *Antiviral Chem. Chemother.* **2010,** *21*, 1.

48. S. Bordiga, C. L., G. Ricchiardi, L. Regli, F. Bonino, A. Damin, K.-P. Lillerud,; Zecchina, M. B. a. A. Electronic and Vibrational Properties of a Mof-5 Metal-Organic Framework: Zno Quantum Dot Behaviour. *Chem. Commun.* **2004**, 2300-2301.

49. Jing-Jing Du, Y.-P. Y., Jia-Xin Sun, Fu-Min Peng, Xia Jiang, Ling-Guang Qiu,; An-Jian Xie, Y.-H. S., Jun-Fa Zhu New Photocatalysts Based on Mil-53 Metal–Organic Frameworks for the Decolorization of Methylene Blue Dye. *J. Hazard. Mater.* **2011**, 945-951.

50. Shirokova, E. A.; Jasko, M. V.; Khandazhinskaya, A. L.; Ivanov, A. V.; Yanvarev, D. V.; Skoblov, Y. S.; Mitkevich, V. A.; Bocharov, E. V.; Pronyaeva, T. R.; Fedyuk, N. V.; Kukhanova, M. K.; Pokrovsky, A. G. Uncharged Azt and D4t Derivatives of Phosphonoformic and Phosphonoacetic Acids as Anti-Hiv Pronucleosides. *J. Med. Chem.* **2004,** *47*, 3606-3614.

51. Daniel W. Miles, W. H. I., Morris J. Robins, Michael W. Winkley,Roland K. Robins, and Henry Eyring Circular Dichroism of Nucleoside Derivatives. Ix. Vicinal Effects on the Circular Dichroism of Pyrimidine Nucleosides. *J. Am. Chem. Soc.* **1970,** *92*, 3872-3881.

52. Miles, D. W.; Robins, M. J.; Robins, R. K.; Winkley, M. W.; Eyring, H. Circular Dichroism of Nucleoside Derivatives. V. Cytosine Derivatives. *J. Am. Chem. Soc.* **1969,** *91*, 831-838.

53. Benesi, H. A., Hildebrand, J. H. A Spectrophotometric Investigation of the Interaction of Iodine with Aromatic Hydrocarbons. *J. Am. Chem. Soc.* **1949,** *71*, 2703-2707.

54. Zattoni, A.; Rambaldi, D. C.; Reschiglian, P.; Melucci, M.; Krol, S.; Garcia, A. M. C.; Sanz-Medel, A.; Roessner, D.; Johann, C. Asymmetrical Flow Field-Flow Fractionation with Multi-Angle Light Scattering Detection for the Analysis of Structured Nanoparticles. *Journal of Chromatography A* **2009,** *1216*, 9106-9112.

SPECTROSCOPIC STUDIES ON ARTEMISININ ASSOCIATION TO CYCLODEXTRIN BASED SYSTEMS

Artemisinin (ART, **Scheme 4.1**), the parent term of the trioxane drug family, is the most effective antimalarial drug currently available to treat multidrug resistant forms of *Plasmodium falciparum*.[1-3] For this drug an anticancer activity has also been documented.[2] Besides its promising results such as high efficacy and rapid action, ART suffers a lot of technological and biopharmaceutical issues, mainly poor bioavailability and low solubility both in aqueous media and oils. In addition, this drug has short half-life and it easily decomposes, most probably by the opening of the lactone ring. One of the strategies to avoid these problems is the development of a suitable carrier system.[4-7] Different reports have shown an increase in the solubility of ART by using using CyD as carrier.[4-7] Moreover, a study of the interaction of ART with β-CyD by circular dichroism has shown the peroxidic group keeps well outside the cavity in the complex, thus the CyD may be believed not to interfere with the pharmacological action related to this molecular functionality.[8] This chapter deals with the interaction of ART with the pβ-CyD-epichlorohydrin crosslinked polymer (see also **Chapter 2**). In addition, a study of photocontrolled guest binding to a bis(β-CyD) bearing an azobenzene as the linker was carried out with ART as model system.
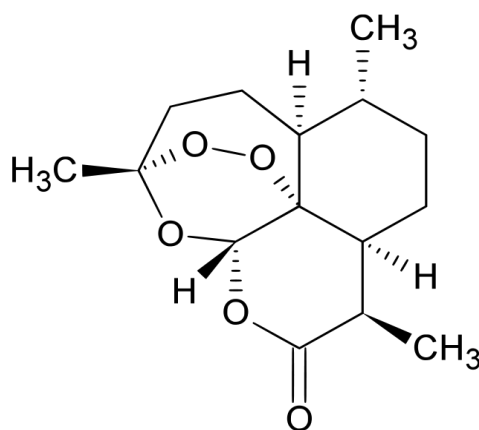
Scheme 4.1 Chemical structure of artemisinin (ART)

Chapter 4

4.1 BINDING OF ARTEMISININ TO A β–CYCLODEXTRIN POLYMER (pβ–CyD)

Synthesis of the pβ-CyD-epichlorohydrin crosslinked polymer (pβ-CyD) is briefly explained in **Chapter 2**. The β-CyD content of the polymer is 77 % w/w and the average molecular weight is 2.1×10^5 g/mol. This material is highly soluble in water (more than 100 mg/mL) where it exists in the form of nanoparticles of < 15 nm diameter (see Chapter 2 for literature relevant to polymer synthesis and characterization).

For the evaluation of pβ-CyD as delivery platform for ART we have investigated the incorporation of the drug within the polymer nanoparticles, performing accurate UV-vis absorption and circular dichroism (CD) titrations. We have evidenced association of ART to the β-CyD units of the polymer network and determined apparent binding constants by global analysis of multiwavelength CD data. In the discussion of the present results previous data by G. Marconi et al. were considered.[8]

4.1.1 UV-Visible absorption and Circular dichroism

The absorption spectrum of ART 1×10^{-5} M in aqueous solution (5% MeOH) is characterized by an intense absorption band with maximum below 200 nm (not accessible) and a long tail extending beyond 300 nm, with shoulders at ca. 230 (log $\varepsilon \sim 2.3$) and ca. 260 nm (log $\varepsilon \sim 2$).

The intrinsic circular dichroism (CD) spectrum of ART is very weak and is characterized by two bands, one positive with a maximum at 260 nm ($\Delta\varepsilon \sim 0.2$ M^{-1}cm^{-1}) and one negative with λ_{max} = 230 nm ($\Delta\varepsilon \sim 0.4$ M^{-1}cm^{-1}). Noticeably the presence of pβ-CyD in water makes ART able to solubilise easily up to concentrations of ca. 10^{-3} M. **Figure 4.1A** shows the CD spectra obtained from a series of samples corresponding to different ART concentrations in presence of 25 mg/mL pβ-CyD, corresponding to a maximum concentration 1.55×10^{-2} M in β-CyD units. Global analysis based on SPECFIT/32 was applied. A formal 1:1 stoichiometry with the β-CyD unit of the polymer was assumed and an association constant log $(K_{11}/M^{-1}) \cong 2$ (DW factor 1.7) was derived. The absolute CD spectrum of the complex is reported in **Figure 4.1B** together with the spectra reported by Marconi et al. for ART in some alcoholic solvents and in the β-CyD complex.[8] It is worth noticing that the shape of the CD spectra of ART in pβ-CyD is not qualitatively different from those in homogeneous solvents. This effect was observed also with β–CyD and was attributed to an induced chirality just superposed to the intrinsic one without negative interferences; it was also shown[8] that the intensity of the 230 nm CD band is in fair linear correlation with the

Reichardt's $E_T(30)$ parameter[9] (a measure of the ionising power of a solvent) of the medium.   The

size of $\Delta\varepsilon$ at 230 nm in the pβ-CyD complex (see **Figure 4.1C**) formally corresponds to a medium of

$E_T(30) \cong 51.2$, very different from water ($E_T(30) = 63.1$) and the β-CyD complex ($E_T (30) \cong 60$)[8] and

similar to ethanol ($E_T(30) = 51.9$), methanol ($E_T(30) = 55.4$) and *n*-butanol ($E_T(30) = 49.7$). It can be

therefore concluded that ART penetrates in the interior of the pβ-CyD nanoparticle, where it

experiences an alcohol-like environment, considerably less hydrophilic than in the β-CyD complex,

where ART accomodates close to the secondary rim of the macrocycle and is largely exposed to

water.[8]
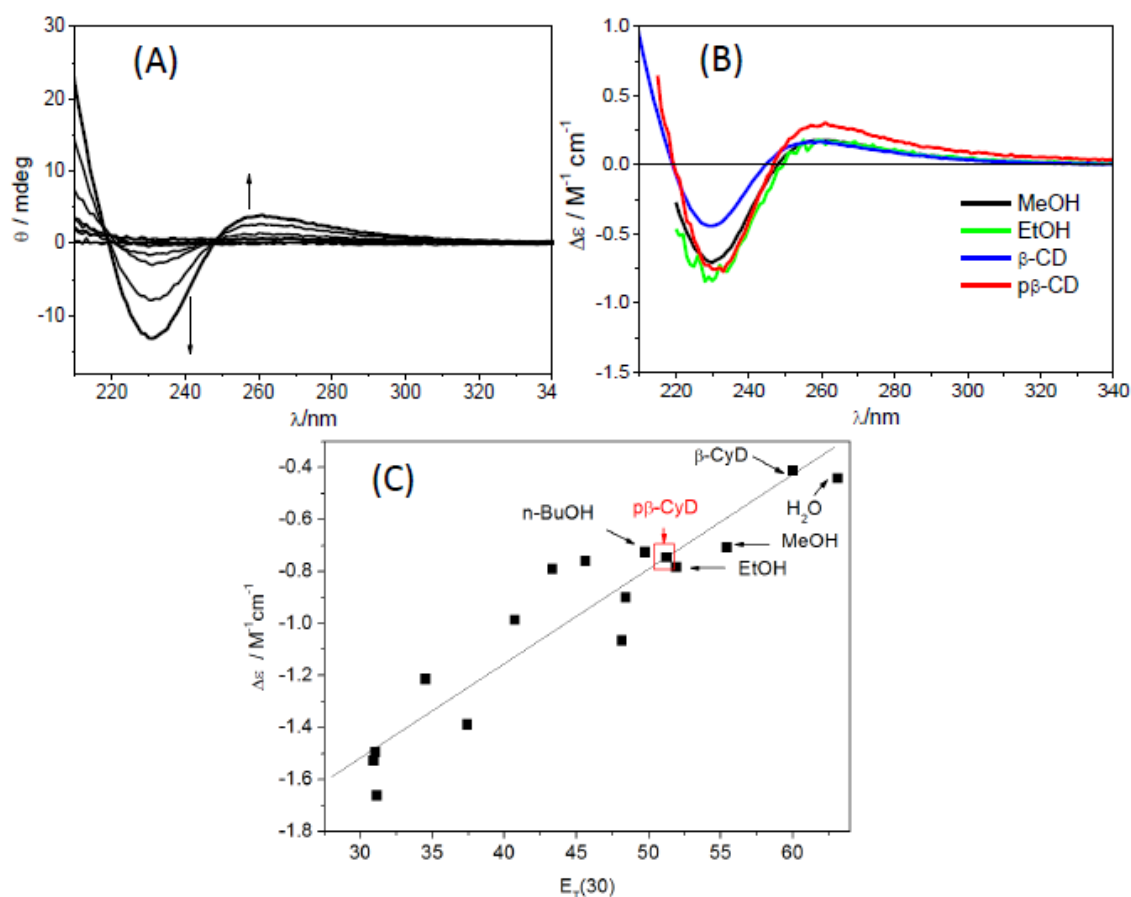
Figure 4.1 (**A**) Induced circular dichroism of ART 5×10^{-6}, 1×10^{-5}, 2×10^{-5}, 5×10^{-5}, 1×10^{-4}, 2×10^{-4}, 5×10^{-4}, 8×10^{-4} in presence of 25 mg/mL pβ-CyD in water at 22 °C. Cell pathlength 1 cm, reference is the pβ-CyD solution. (**B**) Absolute CD spectrum of the ART: pβ-CyD complex (red) compared to those in other media, taken from ref. [6] (**C**) Circular dichroism signal at 230 nm of ART vs. $E_T(30)$ of various media at 22 °C. Data for homogeneous solvents and β−CyD complex are taken from ref. [8]

4.1.2 Summary

The polymeric β−CyD-based nanoparticles revealed to be able to load the strongly hydrophobic

and bulky ART, which was likely incorporated deeply into the nanoparticle frame. The apparent

binding constants with pβ–CyD determined for ART is rather low, but this is most likely a consequence of the assumption of a simplified model for the structure of the host in the analysis of the equilibrium, neglecting its nanostructured organization. In spite of this approximation, multivariate global analysis of multiwavelength CD titration data revealed to be a powerful tool to extract the spectroscopic features of the bound drug and probe the environment. Spectroscopic and photophysical data with ART consistently indicated an alcohol-like character for the interior of the polymer nanoparticles.

4.2 PHOTOCONTROLLED BINDING OF ARTEMISININ TO A BIS(β–CYCLODEXTRIN) BEARING AZOBENZENE ON THE PRIMARY FACE

In the drug delivery field the achievement of efficient encapsulation of drugs into a stable carrier and release under control is still a challenge. The possibility to control guest association and release from a supramolecular device is also of large interest for other nanotechnological applications. Among the external stimuli which can be employed to drive these systems, light is one of the most useful. Thus photoswitchable hosts are expected to find application in light driven functional materials and, possibly, become part of photocontrolled drug delivery vehicles.

Azobenzene is extensively used in photoresponsive supramolecular devices because of its high chemical stability, absorption in the visible wavelength region and efficient reversible *cis-trans* photoisomerisation. bis(β-CyD) derivatives bearing a covalently linked azobenzene moiety have been recently prepared. [10]   Gaining insight into the modes of guest association in these systems and checking for the possibility of light control of guest release appears to be of significance.

In this section, we present a study of the association of artemisinin (ART) to a bis(β-CyD) derivative with an azobenzene 6-6' linker in aqueous solution (CyD$_2$-AB, **Scheme 4.2**)[10] by circular dichroism (CD) and discuss about the effect of light irradiation on this process. ART does not absorb significantly above 300 nm, thus the choice of it as guest in the present study allowed selective optical monitoring of the bis(CyD) host in the 300-600 nm absorption range of the linker. The use of CD spectroscopy also revealed to be particularly useful for detecting the light induced conformational changes   in the host, at low concentrations, because the asymmetric CyD environment is able to induce an optical activity in the azobenzene linker, that is not chiral itself, and the induced CD signal is sensitive to the *trans* or *cis* configuration of the chromophore.
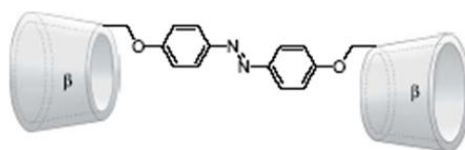
Scheme 4.2 Schematic structure of 4,4'-bis(6'-O-cyclomaltoheptaosyl)azobenzene (CyD$_2$-AB, received from Prof. Antonio Vargas-Berenguel, University of Almeria, Spain.)

4.2.1 UV-visible absorption and Circular dichroism

Spectroscopic measurements were recorded at constant CyD$_2$-AB host concentration and varying the ART concentration. The solubility of ART in pure water is rather poor (solubility limit is 4.3 x 10^{-3}M at 37 ^{o}C).[11] In order to study the CyD$_2$-AB complexation equilibrium in TRIS buffer, we performed CD titration experiments by varying the ART concentration in the range 1×10^{-4} - 1×10^{-3}M and keeping the CyD$_2$-AB concentration fixed at 10^{-4}M or 10^{-3}M.   A concentrated solution of ART in ethanol was prepared and known aliquots were introduced in suitable flasks, the solvent was removed by evaporation, then a known volume of the CyD$_2$-AB aqueous solution was added to each flask to obtain the required ART concentration.

Figure 4.2A shows the absorption spectrum of the CyD$_2$-AB host 10^{-4} M in TRIS buffer 0.01 M pH 7.4. The n,π* S$_0$→S$_1$ band, formally forbidden and due to promotion of lone pair electrons of the *trans*-azobenzene linker, appears as a shoulder at ca. 430 nm (log $\varepsilon \approx$ 3.3-3.5), the π,π* band relevant to the allowed S$_0$→S$_2$ transition is the most intense and has λ_{max} = 360 nm (log ε = 4.2), whereas a lower intensity band is present at 244 nm (log ε = 3.9). A reasonable model for CyD$_2$-AB is *trans*-4,4'-dimethoxyazobenzene whose spectral features have been reported to be similar,[12] although somewhat higher molar absorption coefficients in the π,π* S$_0$→S$_2$ band have also been reported for the same molecule. [13] For this reason we cannot exclude to have some *cis* form in solution and safely consider the given molar absorption coefficients (**Figure 4.2A**) as *apparent* values for the *trans* form. The CD spectrum of CyD$_2$-AB is (**Figure 4.2A**) characterized by positive peaks at 252 and 364 nm and negative peaks at 320 and 416 nm. They are approximately located in correspondence of maxima/shoulders in the absorption spectrum and are assigned to the azobenzene linker. The two CyD moieties themselves may contribute somewhat below 230 nm.
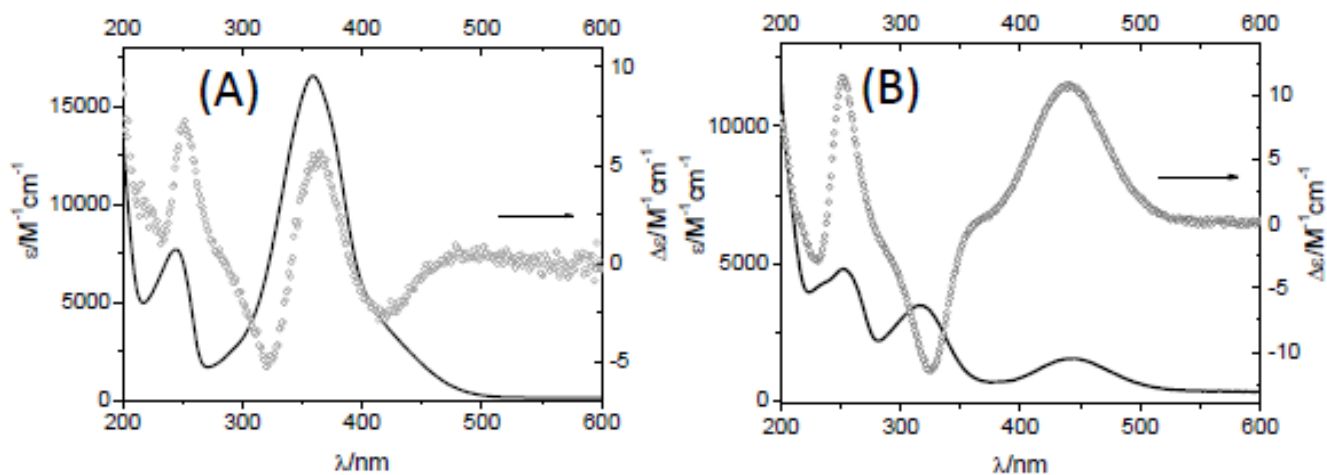
Figure 4.2 Apparent molar absorption coefficients (ε, solid line) and CD ($\Delta\varepsilon$, symbol) calculated for the CyD$_2$-AB host in TRIS buffer 0.01M at pH 7.4: **(A)** for a 10^{-4} M solution prepared in the dark (mainly *trans*). (**B**) for the same solution irradiated at 363 nm up to the photostationary state (mainly *cis*).The reference was TRIS buffer.

The spectroscopic features of CyD$_2$-AB in the *cis* configuration can be qualitatively appreciated upon photoirradiation of a solution of the *trans* form at 363 nm, until the establishment of the stationary state for the *trans-cis* photochemical equilibrium. It is well known that in azobenzenes the photostationary state (pss) for irradiation at λ_{irr} close to the absorption λ_{max} of the π,π^* S$_0\to$S$_2$ band of the *trans* isomer, contains the *cis* isomer as largely predominant form. For example, for azobenzene the pss for irradiation at 317 nm in aqueous medium is [cis]/[trans] $\cong$ 5.[14,15] Because methoxysubstituted azobenzenes are not expected to behave much differently from azobenzene, we can safely assume to have the *cis*-CyD$_2$-AB as the predominant form in the irradiated solution. Thus we attribute the absorption and CD spectra in **Figure 4.2B** mainly to the azobenzene linker in *cis* configuration, with an intense positive band at 440 nm, due to the n,π^* S$_0\to$S$_1$ electronic transition, an intense 324 nm negative band, due to the S$_0\to$S$_2$ π,π^* transition, and a positive band peaked at 252 nm. In this case the coincidence between the maxima/minima of the CD and the maxima of the absorption bands is very good.

Figure 4.3A shows the CD spectra obtained from a series of samples corresponding to different ART concentrations from 5×10^{-5} M to 1×10^{-3} M in presence of a constant 10^{-4} M concentration of *trans* CyD$_2$-AB. Analysis of the complexation equilibrium was performed in the 300-600 nm range using the whole set of CD spectra with a multivariate, multiwavelength, global fitting procedure based on SPECFIT/32 (see **chapter 5, Experimental**). In this spectral window guest binding can be followed selectively inspecting at the linker CD modifications. The best fit was found for formation of a 1:1 stoichiometry complex with log (K_{11}/M^{-1}) = 4.1 $\pm$ 0.1 (DW 1.5). The absolute CD spectrum of the complex was also retrieved from the analysis (**Figure 4.3B**).

Compared to that of the free host it appears much more intense both in the positive peak at 363 nm (π,π^* transition) and in the negative peak at 426 nm (n,π^* transition). The latter is red shifted by ~10 nm.

Figure 4.3C shows a titration experiment in which the 10^{-4} M *trans* CyD_2-AB solution was previously irradiated at 363 nm up to the pss, in order to obtain the *cis* CyD_2-AB as predominant host form in solution (see spectra in **Figure 4.2B**); then titration with ART was carried out. In this case the CD spectra did not change on increasing the ART concentration, clearly showing that the *cis* CyD_2-AB host does not appreciably interact with the drug. ART displays complete selectivity for the *trans* host configuration. The latter, interestingly, is not affected by ART association as regards the efficiency of photoconversion to the *cis* form. Indeed the same CD intensity is measured upon irradiation of *trans* host followed by addition of ART or irradiation of the *trans* host-ART mixture (**Figure 4.3D**).

The irradiated CyD_2-AB-ART mixtures stored in the dark at 22°C (for 2 days) showed partial recovery of the absorption at 363 nm and CD evolution, consistent with thermal conversion of the *cis* host back to the *trans* configuration. The process can be accelerated by visible light, using a λ_{irr} at which the absorption coefficients of the *cis* are higher than those of the *trans* host. These results suggest that control of ART uptake/release in solution is feasible through the *trans-cis* isomerization of the azobenzene linker.

Comparing the association constant of ART to *trans* CyD_2-AB with that to natural β-CyD in 1:1 stoichiometry (log (K_{11}/M^{-1})= 2.4)[8] we see the affinity is much higher for the present host. ART is not able to penetrate deeply into the β-CyD cavity but, as shown by molecular modelling[8], locates close to the secondary rim. In the present case ART reasonably locates in the inner space between the primary rims of the two CyD moieties, where cooperative effects between the two CyD macrocycles and a direct interaction with the azobenzene linker, in particular with the N=N bond lone pairs, may take place. Consistently the CD bands corresponding to the electronic transitions of the azobenzene chromophore acquire an important induced contribution from the chiral ART centers in close proximity (**Figure 4.3B**). The observation that CyD_2-AB in the *cis* configuration is not capable of binding ART suggests a large scale change in the conformation, leading to loss of cooperativity between the two CyD moieties.
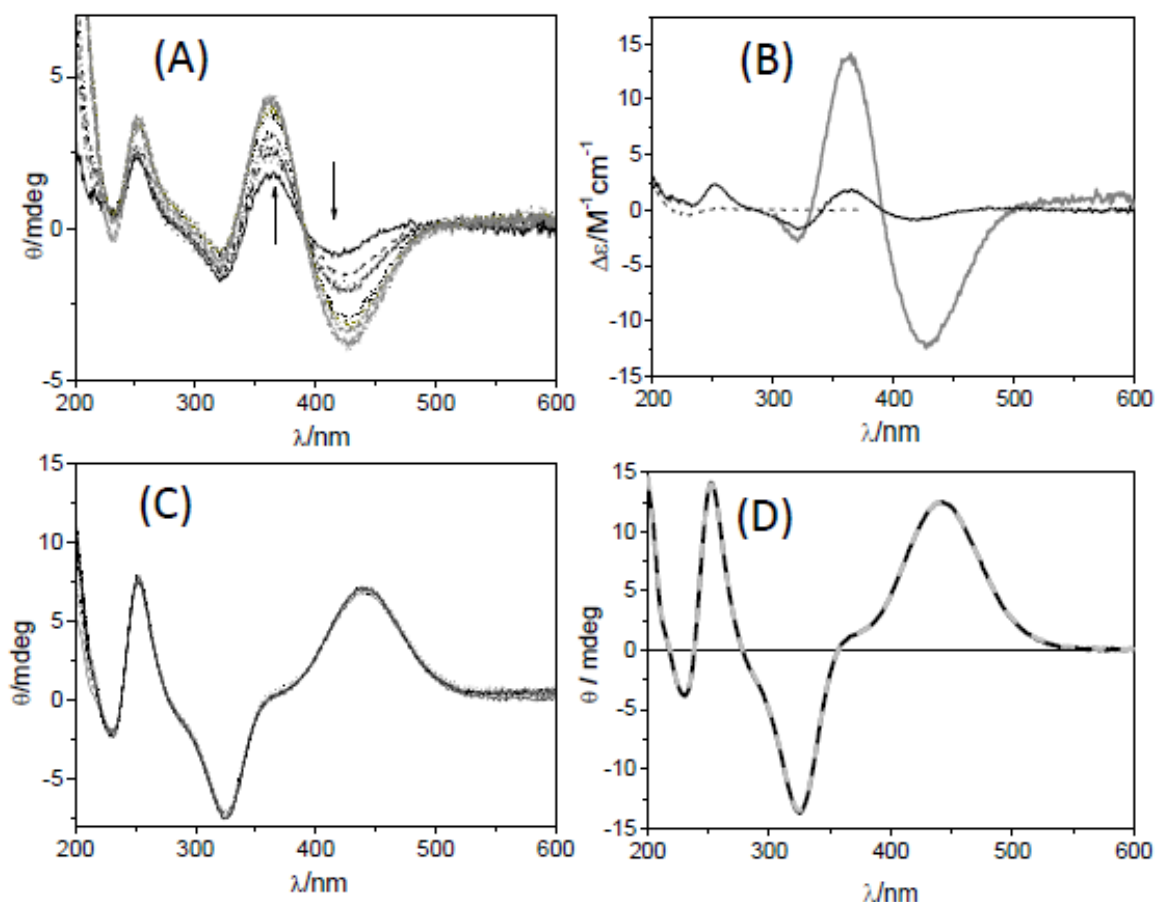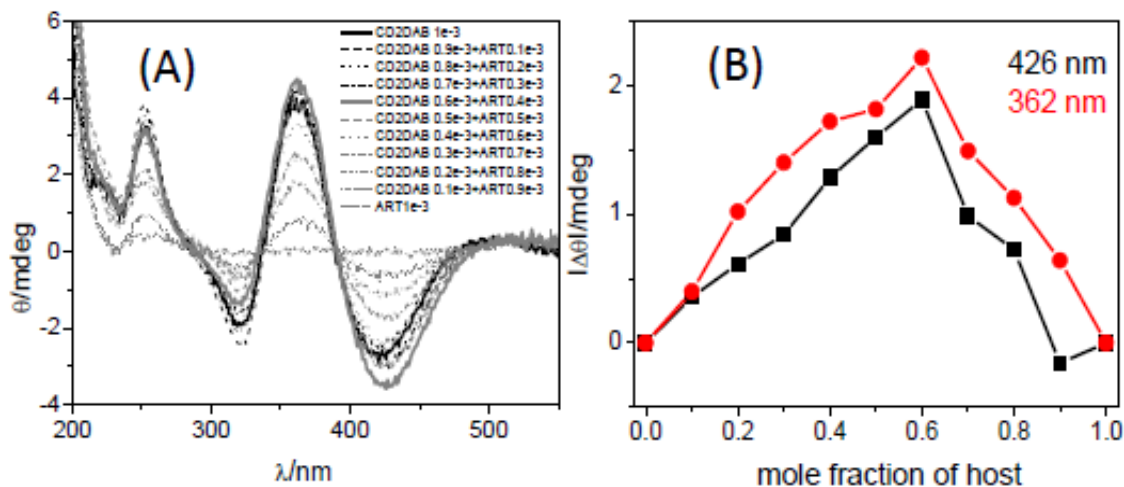
Figure 4.3 (A) Ellipticity changes of *trans* CyD_2-AB 1.0×10^{-4} M in Tris buffer 0.01M at pH 7.4, titrated with ART in the concentration range 5.0×10^{-5} M - 1.0×10^{-3} M, cell pathlength 0.1 cm; (**B**) Absolute CD spectra of ART (dashed line, from ref.8, free *trans* CyD_2-AB (black solid line), 1:1 complex (grey solid line). (**C**) In the same conditions, ellipticity changes of *cis*-enriched CyD_2-AB 1.0×10^{-4} M solution irradiated at 363 nm and then titrated with ART, cell pathlength 0.2 cm. (**D**) *trans* CyD_2-AB 2.0×10^{-4} M, ART 2.0×10^{-4} M, cell pathlength 0.2 cm: mixture prepared in the dark then irradiated with light at $\lambda > 295$ nm up to pss (black solid line); *trans* CyD_2-AB alone irradiated similarly and then mixed with ART. Temperature was 22 °C in all experiments.

The system shows a more complex binding behaviour at higher host concentrations. A CD titration of 10^{-3} M *trans* CyD_2-AB with ART (data not shown) indicated formation of a complex with 2:1 CyD_2-AB:ART stoichiometry and $\log (K_{21}/M^{-2}) = 6.7 \pm 0.3$ (DW 1.98). The existence of such complex was also confirmed by a continuous variation experiment (**Figure 4.4A**),[16] performed at 10^{-3} M total CyD_2-AB+ART concentration. The absolute value of the ellipticity at 426 and 362 nm, associated to the complexation progression, was corrected subtracting the CyD_2-AB intrinsic signaland $|\Delta\theta|$ was plotted *vs.* the host molar fraction. The plots are characterized by a broad asymmetric bell-shape profile with maximum at ca. 0.6 molar fraction of host. This indicates a significant presence of 2:1 complexes in the equilibrium mixture. Work is in progress to study the

ART complexation process in *cis*-enriched CyD$_2$-AB concentrated solutions and check for the possibility of photocontrolled ART release from the 2:1 complex.

Figure 4.4 (**A**) Ellipticity changes in a continous variation experiment for [*trs* CyD$_2$-AB + ART] = 1.0×10^{-3} M, cell pathlength 0.1 cm, 22°C; (**B**) Modified Job plot of absolute value of ellipticity change at 426 and 362 nm, after subtraction of the signal of host alone.

4.2.2 Summary

We have shown that a light responsive bis(β-CyD) derivative with an azobenzene 6-6' linker (CyD$_2$-AB, **Scheme 4.2**) has a binding affinity controllable by light. This host is able to form a strong 1:1 complex with artemisinin (ART) when the Azobenzene bridge is in the *trans* configuration. Irradiation with light at 363 nm switches the linker from the *trans* to the *cis* configuration and the latter shows a complete loss of affinity for ART. The difference in the binding ability between the two geometrical isomers of CyD$_2$-AB suggests that light induced uptake/release of ART in aqueous solution is feasible through the photoisomerization reaction.

This model system demonstrates that azobenzene linked bis(β-CyD)s carriers may represent useful tools for photocontrolled capture and release of guests.

REFERENCES

1. Li, J.; Zhou, B. Biological Actions of Artemisinin: Insights from Medicinal Chemistry Studies. *Molecules* **2010,** *15*, 1378-1397.
2. Chaturvedi, D.; Goswami, A.; Saikia, P. P.; Barua, N. C.; Rao, P. G. Artemisinin and Its Derivatives: A Novel Class of Anti-Malarial and Anti-Cancer Agents. *Chem. Soc. Rev.* **2010,** *39*, 435-454.

3. Kumar, N.; Sharma, M.; Rawat, D. S. Medicinal Chemistry Perspectives of Trioxanes and Tetraoxanes. *Curr. Med. Chem.* **2011,** *18*, 3889-3928.

4. Wong, J. W.; Yuen, K. H. Improved Oral Bioavailability of Artemisinin through Inclusion Complexation with Beta- and Gamma-Cyclodextrins. *Int. J. Pharm.* **2001,** *227*, 177-185.

5. Zime-Diawara, H.; Dive, G.; Piel, G.; Moudachirou, M.; Frederich, M.; Quetin-Leclercq, J.; Evrard, B. Understanding the Interactions between Artemisinin and Cyclodextrins: Spectroscopic Studies and Molecular Modeling. *J. Inclusion Phenom. Macrocyclic Chem.* **2012,** *74*, 305-315.

6. Marconi, G.; Monti, S.; Manoli, F.; Degli Esposti, A.; Guerrini, A. Circular-Dichroism Studies on Artemisinin and Epiartemisinin and Their Beta-Cyclodextrin Complexes in Solution. *Helv. Chim. Acta* **2004,** *87*, 2368-2377.

7. Isacchi, B.; Bergonzi, M. C.; Grazioso, M.; Righeschi, C.; Pietretti, A.; Severini, C.; Bilia, A. R. Artemisinin and Artemisinin Plus Curcumin Liposomal Formulations: Enhanced Antimalarial Efficacy against Plasmodium Berghei-Infected Mice. *European Journal of Pharmaceutics and Biopharmaceutics* **2012,** *80*, 528-534.

8. Marconi, G.; Monti, S.; Manoli, F.; Degli Esposti, A.; Mayer, B. A Circular Dichroism and Structural Study of the Inclusion Complex Artemisinin-Beta-Cyclodextrin. *Chem. Phys. Lett.* **2004,** *383*, 566-571.

9. Reichardt, C. Solvatochromic Dyes as Solvent Polarity Indicators. *Chem. Rev.* **1994,** *94*, 2319-2358.

10. Casas-Solvas, J. M.; Martos-Maldonado, M. C.; Vargas-Berenguel, A. Synthesis of Beta-Cydodextrin Derivatives Functionalized with Azobenzene. *Tetrahedron* **2008,** *64*, 10919-10923.

11. Jung, M. K.; Lee, K.; Kendrick, H.; Robinson, B. L.; Croft, S. L. Synthesis, Stability, and Antimalarial Activity of New Hydrolytically Stable and Water-Soluble (+)-Deoxoartelinic Acid. *J. Med. Chem.* **2002,** *45*, 4940-4944.

12. Gore, P. H.; Wheeler, O. H. Absorption Spectra of Aromatic Azo and Related Compounds. Iii. Substituted Azobenzenes. *J. Org. Chem.* **1961,** *26*, 3295-3298.

13. Fabian, J.; Hartmann, H., *Light Absorption of Organic Colorants*. Springer Verlag: Berlin - Heidelberg, 1980; Vol. 12.

14. Bortolus, P.; Monti, S. Cis-Trans Photoisomerization of Azobenzene - Solvent and Triplet Donor Effects. *J. Phys. Chem.* **1979,** *83*, 648-652.

15. Siampiringue, N.; Guyot, G.; Monti, S.; Bortolus, P. The Cis-]Trans Photoisomerization of Azobenzene - an Experimental Reexamination. *J. Photochem.* **1987,** *37*, 185-188.

16. Job, P. Formation and Stability of Inorganic Complexes in Solution. *Ann. Chim.* **1928,** *9*, 113-203.

EXPERIMENTAL SECTION

5.1 MATERIALS

Doxorubicin (DOX, ALEXIS Biochemicals), γ-Cyclodextrin (γ-CyD, Fluka), Artemisinin (ART, Aldrich), Azido 3'-deoxythymidine (AZT, Moravek), Azido-3'-deoxythymidine-5'-monophosphate (AZT-MP, Carbosynth) and Azido-3´-deoxythymidine-5´-triphosphate (AZT-TP, TriLink) were used without further purification. Water was purified by passage through a Millipore MilliQ system. PBS buffer (0.01M, pH 7.4) and TRIS buffer (0.01M, pH 7.4) were prepared in the laboratory.

Several materials for my studies were obtained from CYCLON community network program. The epichlorohydrin-β-CyD copolymer (pβ-CyD) and iron trimasate nano MOF were prepared by the group of Dr. Ruxandra Gref, UMR-CNRS,France and some detail of preparation is in **Chapter2** and **Chapter3.** The citric-acid-γ-CyD polymer was prepared by Milo Malanga (CYCLOLAB) in collaboration with the group of Prof. Antonio Vargas-Berenguel and some detail of preparation is in **Chapter2.**The azobenzene-linked bis β-cyclodextrin (CyD$_2$-AB) was given byProf. Antonio Vargas-Berenguel and details of preparation are in ref.10 of Chapter4

5.2 MIL-100(Fe) SAMPLE PREPARATION

MIL-100 (Fe) was stored in the dark at room temperature as ethanol wet material. An aliquot of it was dispersed in a few milliliters of ethanol. The suspension was centrifuged (10 min, 10000 rpm) and washed two times with tridistilled water and one time with TRIS buffer (10^{-2} M, pH 7.4) to remove traces of ethanol. Aliquots of the resulting centrifugate was suitably dispersed in TRIS buffer and used for the preparation of individual samples. MOF alone suspensions and mixtures with DOX and azidothymidine derivatives were gently stirred for 30 min to attain a steady condition before use and were kept under stirring during the time span of all the experiments.

5.3 INSTRUMENTATION

5.3.1 UV-visible absorption spectroscopy

UV-Visible absorption spectra of CyD's and CyD-drug samples were recorded on Perkin-Elmer Lambda 650 or Lambda 950 spectrophotometers. All the measuremets were done in 1 cm, 0.5 cm or 0.2 cm pathlength cells at intervals of 1nm using water, TRIS, PBS or CyD as the reference

UV-visible absorption spectra of nano MOF and nano MOF-drug mixtures were measured on Perkin-Elmer Lambda 9 spectrophotometer equipped with an integrating sphere to measure the true absorption spectra free from light scattering contribution of nano MOFs. All the measurements were done in 0.5 cm path length cell at intervals of 1 nm, using water, TRIS buffer or nano MOF as the reference.

5.3.2 Circular dichroism spectroscopy

The circular dichroism (CD) spectropolarimeter measures the differential absorption of left and right circularly polarized light ($\Delta A = A_L - A_R$) and generally reports it in terms of ellipticity.[1]
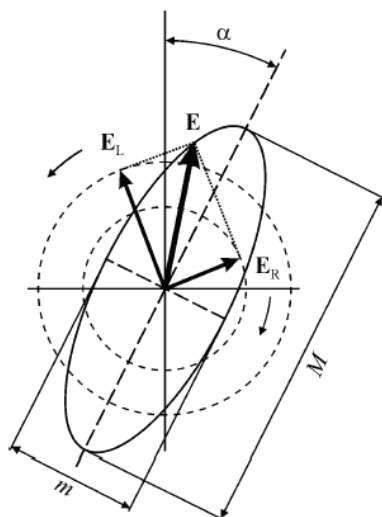
Scheme 5.1 Schematic representation of differential absorption of left-and right hand polarized components leads to ellipticity

When circular dichroism occurs, the two circularly polarized components emerging from the sample possess not only a phase difference but also different amplitudes. The polarization of the radiation corresponding to their composition is no longer circular but elliptical, the tip of the electric field vector, projected in a plane perpendicular to the travelling direction of the wave,

describes an ellipse. The different absorption experienced by the two circularly polarized components is expressed by means of the ellipticity θ, defined as the angle whose tangent is equal to the ratio between the minor (*m*) and the major (*M*) axes of the ellipse

$$\tanθ = m/M \qquad\qquad \textbf{(5.1)}$$

A CD signal will be observed when the chromophore is optically active due to intrinsic chirality or is placed in an asymmetric environment.

The CD spectra of the drug-host mixture were measured by means of a Jasco J-715 dichrograph. The spectra were registered in 0.5 or 0.2 cm pathlength quartz cuvettes, with 3-5 accumulations at a scan speed of 50 nm/min to improve signal to noise ratio. The signal of the medium (TRIS buffer 0.01 M, pH 7.4 for drug free, CyD or MOF solutions of same concentrations for drug-host mixtures), were subtracted.

5.3.3 Fluorescence spectroscopy

Steady state fluorescence experiments of γ-CyD and MOF-drug samples were registered in air-equilibrated solutions in 1 cm standard cells on a SPEX Fluorolog 111 spectrofluorimeter.

The pβ-CyD-DOX and pγ-CyD-DOX samples were registered in cells with triangular section. The excitation beam was incident at 45 °C onto the "diagonal" cell surface and the emission was collected at a right angle; suitable filters were used to cut the excitation light. No polarizers were used. Fluorescence quantum yields were measured with excitation at 550 nm in solutions with absorbance of 0.09 for 1 cm pathlength. A fluorescence quantum yield of 0.039 was determined for DOX 1×10^{-5} M in neutral phosphate buffer at 22 °C with $Ru(bpy)_3Cl_2$ as reference(Φ = 0.028, in air equilibrated solution). The quantum yields of DOX emission in the various complexes or in different environments were determined using the quantum yield of DOX 1×10^{-5} M in buffer as reference.

5.3.4 Time resolved emission measurements

Fluorescence lifetimes in air-saturated solutions were measured with a time correlated single photon counting system (IBH Consultants Ltd.). A nanosecond LED at 465 nm was used as the excitation source and the emission was collected at a right angle at 590 nm. The software package

for analysis of emission decays was provided by IBH Consultants Ltd. Decay profiles were fitted using a multiexponential function and deconvolution of the instrumental response.

$$I(t) = \sum_i a_i \times \exp(-t/\tau_i) \qquad\qquad \textbf{(5.2)}$$

$$f_i = (a_i \times \tau_i)/ \sum_j (a_j \times \tau_j) \qquad\qquad \textbf{(5.3)}$$

5.3.5 Nanosecond laser flash photolysis

The pulse of a Nd-YAG laser, operating at 532 or 266 nm (20 ns FWHM, 2 Hz), was suitably shaped passing through a rectangular, 3 mm high and 10 mm wide window, and providing a fairly uniform energy density, incident onto the sample cell (a pulse of 3.5 mJ at 266 nm corresponds to 12 mJ/cm^2). A front portion of 2 mm of the excited solution was probed at right angle, the useful optical path for analyzing light being 10 mm. A_{266} was ~ 0.5-1 over 1 cm. Ar-saturated solutions were used. The sample was renewed after few laser shots. Temperature was 295 K.

5.3.6 Confocal microscopy

Confocal fluorescence imaging was performed on an inverted Nikon A1 laser scanning confocal microscope equipped with a CW argon ion laser for excitation at 457, 488 and 514 nm (Melles Griot, 40 mW), and a diode laser for excitation at 405 nm (LDH-D-C-405 of Picoquant GmbH Berlin, Germany) operating both in continuous mode (50 mW) and pulsed at 40 MHz (1.0 mW average power for pulse FWHM of 70 ps). Confocal fluorescence imaging was carried out on the samples at room temperature. The images were collected using a Nikon PLAN APO VC 60× NA 1.40 oil immersion objective. Images of 512 X 512 or 1024 X 1024 pixels have been acquired applying scan speed of 1 frame in 2-8 s and pixel dimension of the xy plane falls in the range 0.1-0.4 μm. Hexagonal pinhole dimension was set to 0.8-1.0 au corresponding to 25-38 μm and optical thickness of 330-440 nm. Two dichroic mirrors reflecting either 405, 488, 541 and 640 nm or 457 and 514 nm were used. Bandpass filters in front of the PMT selected fluorescence in the ranges 425-475 nm, 500-550 nm and 570-615 nm. Spectral imaging was done with Nikon 32-PMT array detector with resolution varying from 6 to 10 nm per channel and a 20/80 beam splitter instead of dichroic mirror. For fluorescence lifetime imaging a time-correlated single photon counting (TCSPC) system of Picoquant GmbH Berlin was used exciting at 405 nm. Photons were detected in

TTTR mode with two Single Photon Avalanche Diodes manufactured by Micro Photon Devices (MPD), Bolzano, Italy. Fluorescence was filtered with the opportune fluorescence SEMROCK bandpass filters 520/40 nm, and 585/40 nm. PicoHarp 300 photon processor completes the TCSPC system. SymPhoTime v. 5.1 analysis software was used for image processing and lifetime fitting. A tail fit with multi-exponential functions was performed to analyze fluorescence decays of selected ROI. The system allowed measurement of fluorescence lifetimes from 300 ps up to several nanoseconds.

5.3.7 Asymmetric Flow Field Flow Fractionation with Multi Angle Light Scattering (AF4-MALS)

AF4-MALS is an effective technique for the size separation and detection of nano sized analytes. The separation system consists of two plates, separated by a spacer foil and the plates are bolted together. The upper channel plate is impermeable and the bottom plate is permeable and is made of a porous frit material. An ultrafiltration membrane with a typical size barrier of 10 kD, covers the bottom plate to prevent the sample from penetrating the channel. First, the sample is introduced into a solvent stream which is injected into the channel and is focused in the channel region near the injection port. This is achieved by splitting the channel flow into two components, each of which enters the channel from opposite ends. The flows are adjusted so that they meet close to the injection port and at this point the flow direction is perpendicular towards the porous bottom of the channel. The sample is driven towards the bottom wall and concentrated close to the membrane. Diffusion associated with Brownian motion creates a counteracting motion. Within a couple of minutes a stationary equilibrium is established, in which the two forces balance out for each particle size at a different distance from the bottom wall. Smaller particles, which have higher diffusion rates and are subject to lower friction force, reach an equilibrium position further away from the bottom wall. Bigger particles or molecules will be driven closer to the bottom wall.[2] This is exactly the opposite of a size exclusion (SEC) separation in which the large molecules elute first.[2]
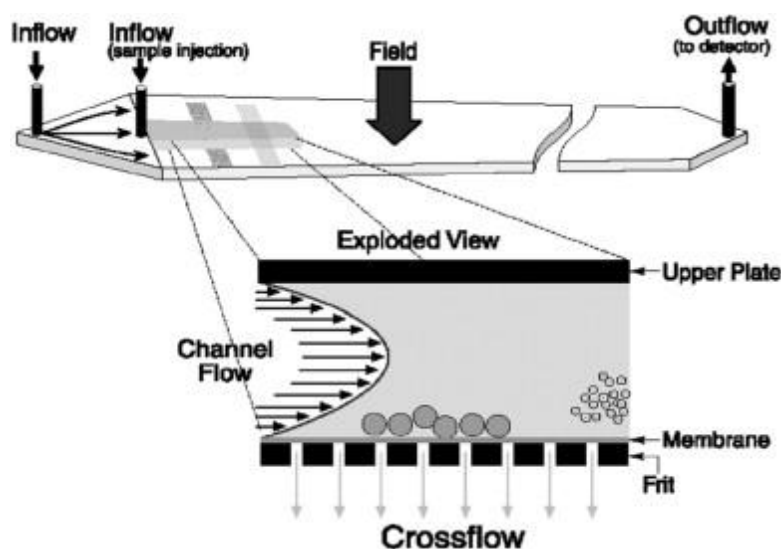
Scheme 5.2 Schematic representation of AF4 (*Adapted from Ref [3]*)

AF4 measurement was performed using an Agilent 1100 liquid chromatography system (Agilent Technologies, Palo Alto, CA) equipped with an Eclipse 3 separation system (Wyatt Technology, Europe, Dernbach, Germany). Polyethersulfone (PES) membranes with 10 KDa molarmass cut-off were used as accumulation wall. Online detection of the eluted species was performed with DAWN HELEOS MALS (Wyatt technology Corporation, Santa Barbara, CA) and an Optilab rEX RI detector (Wyatt Technology Corporation). The software package Wyatt Eclipse @ ChemStation Version B.03.01 (Wyatt Technology Europe) was used to set and control the flow rate values and the PDA detectors.[4] All the measurements were performed using water as dispersant medium for nano MOF and as carrier liquid.

5.4 GLOBAL ANALYSIS OF EQUILIBRIUM SPECTROSCOPIC DATA BY USING SPECFIT/32

The receptor-ligand complexation equilibria were investigated by performing spectroscopic titrations. The best complexation model and the association constants were determined by multivariate global analysis of multiwavelength data from a series of 9-11 spectra (UV-vis absorption, CD or FL titration data) corresponding to different mixtures, using the commercial SPECFIT/32 (v.3.0.40, TgK Scientific) program.[5,6] Multiwavelength spectroscopic data sets (absorbances, ellipticities, fluorescence intensities) are arranged in matrix form **Y**, where a number Nw of wavelengths and a number Nm of corresponding measured spectroscopic signals are ordered in columns, whereas ligand and receptor concentrations are inserted in rows. Thus each element of the data matrix Y_{ij} corresponds to a wavelength j and an experimental quantity

Chapter 6

(absorbance, circular dichroism, fluorescence intensity) for a given couple of concentrations i of ligand and receptor (typically in our experiments one of them is kept constant). A least square best estimator **Y'** of the original data **Y** is reconstructed as the eigenvector representation **Y' = U×S×V**, where **S** is a vector that contains the relative weights of the significant eigenvectors (Ne, number of significant eigenvectors), **U** is a matrix (Nm×Ne) of concentration eigenvectors ($U^T×U=1$, orthonormal) and **V** (Ne×Nw) is a matrix of spectroscopic eigenvectors ($V×V^T$, orthonormal). This **Y'** matrix contains less noise than **Y** because the SVD procedure can factor random noise from the principal components. This reconstructed data matrix **Y'** is utilized in the global fitting instead of the original data matrix **Y**. Complexation equilibria are solved assuming a complexation model (i.e. contemporary presence of a number of complexes of given stoichiometries in equilibrium with free species in solution) and optimizing the numeric combination of all the spectroscopic contributions to best reproduce the **Y'** signals. The analysis relies mainly to absorption data, but also CD and fluorescence data may be analysed, in the latter case provided they are relevant to optically thin samples (linear dependence of fluorescence signal on concentration for all the species involved). Given the direct linearity between experimental signal and concentration and the relation that must exist between the concentrations of the various species in the postulated simultaneous equilibria, the program calculates the conditional association constants and the spectra of the complexes based on a non linear least square fit, using the Levenberg-Marquardt algorithm,   to best reproduce the experimental data for all the explored wavelengths and ligand-receptor concentration couples. The quality of the fits was evaluated on the basis of their Durbin-Watson (DW) factor and the relative error of fit. The DW test is very useful to check for the presence of auto-correlation in the residuals. This method is recommended for systematic misfit errors that can arise in titration experiments. It examines the tendency of successive residual errors to be correlated. The Durbin-Watson statistics ranges from 0.0 to 4.0, with an optimal mid-point value of 2.0 for uncorrelated residuals (i.e. no systematic misfit). In contrast to the χ^2 (Chi-squared) statistics, which requires the noise in the experimental data is random and normally distributed, the DW factor is meaningful even when the noise level in the data set is low. Since the factorized data usually have a significantly lower noise level than the original data, DW test is ideal for the present type of data.

We applied this method to analyze UV-visible absorption, CD and FL titration experiments. Below as an example we describe the analysis of the titration of DOX with pβ-CyD with CD

monitoring in the region 250-600 nm (Figure 2.11B). In the calculation the dimerization constant of DOX has been fixed as $\log(K_{dim}/M^{-1})$= 4.84 and the formation of a 1:1 complex was assumed.

```
 [FACTOR ANALYSIS]
```

Tolerance = 1.000E-09

Max.Factors = 10

Num.Factors = 5

Significant = 2

Eigen Noise = 3.220E-01

Exp't Noise = 1.610E-01

#	Eigenvalue	Square Sum	Residual	Prediction
1	1.383E+05	3.115E+03	1.217E+00	Data Vector
2	2.897E+03	2.181E+02	3.220E-01	Data Vector
3	1.532E+02	6.488E+01	1.756E-01	Possibly Data
4	3.258E+01	3.230E+01	1.240E-01	Probably Noise
5	1.741E+01	1.489E+01	8.418E-02	Probably Noise

[MODEL]

Species = 4

Parameters = 4

[SPECIES]	[COLORED]	[FIXED]	[SPECTRUM]	Notes
1 0 0	False	False		CyD unit
0 1 0	True	True	FIXED	DOX monomer
1 1 0	True	False		1:1 complex
0 2 0	True	False		DOX Dimer

[SPECIES]	[FIXED]	[PARAMETER]		[ERROR]
1 0 0	True	0.00000E+00	+/-	0.00000E+00
0 1 0	True	0.00000E+00	+/-	0.00000E+00
1 1 0	False	2.25747E+00	+/-	1.54188E-01
0 2 0	True	4.84000E+00	+/-	0.00000E+00

[CONVERGENCE]

Iterations = 3

Sum(Y-y)^2 Residuals = 1.71089E+01

Std. Deviation of Fit(Y) = 9.01540E-02

[STATISTICS]

Experimental Noise = 9.754E-02

Relative Error of Fit = 2.7188%

Durbin-Watson Factor = 2.7187

Goodness of Fit, Chi^2 = 8.542E-01

[COVARIANCE]

1.817E-01

[CORRELATION]

1.000E+00

REFERENCES

1. Rodger, A.; Norden, B. Circular dichroism and linear dichroism. *Oxford University Press, Oxford* **1997**.

2. Johann, C.; Ramage, P.; Hemmig, R. Asymmetric Flow Field-Flow Fractionation (Af4) with Multi-Angle Light Scattering (Mals) for High-Throughput Protein Refolding. *Lc Gc Europe* **2005,** *18*, 532.

3. Chiaramonte, E.; Rhazi, L.; Aussenac, T.; White, D. R. Amylose and Amylopectin in Starch by Asymmetric Flow Field-Flow Fractionation with Multi-Angle Light Scattering and Refractive Index Detection (Af4-Mals-Ri). *Journal of Cereal Science* **2012,** *56*, 457-463.

4. Zattoni, A.; Rambaldi, D. C.; Reschiglian, P.; Melucci, M.; Krol, S.; Garcia, A. M. C.; Sanz-Medel, A.; Roessner, D.; Johann, C. Asymmetrical Flow Field-Flow Fractionation with Multi-Angle Light Scattering Detection for the Analysis of Structured Nanoparticles. *Journal of Chromatography A* **2009,** *1216*, 9106-9112.

5. Gampp, H.; Maeder, M.; Meyer, C.J.; Zuberbühler, A.D. Calculation of Equilibrium Constants from Multiwavelength Spectroscopic Data - Ii. Specfit: Two User-Friendly Programs in Basic and Standard Fortran 77. *Talanta* **1985**, *32*, 257-264.

6. Gampp, H.; Maeder, M.; Meyer, C.J.; Zuberbühler, A.D. Calculation of Equilibrium Constants from Multiwavelength Spectroscopic Data - I. Mathematical Considerations. *Talanta* **1985,** *32*, 95-101.

CONCLUSIONS

This thesis work mainly deals with the application of electronic UV–vis absorption, circular dichroism and fluorescence to the study of the non covalent interaction between some drugs and some nanostructured hosts, to be evaluated as potential carriers in pharmacological applications. Two host systems have been examined in aqueous media, cyclodextrin-based polymers and nanoparticles of Metal Organic Frameworks (MOFs), provided by partners in the EU-ITN-CYCLON network. The drugs taken into consideration have been the anticancer doxorubicin and some anti-HIV phosporilated azidothymidine derivatives. Some attention has been also dedicated to artemisinin, an antimalarial and anticancer agent.

Equilibrium data from titration experiments, suitably analysed (when possible with global multivariate methods based on singular value decomposition and non linear regression modelling), have provided valuable information on the stoichiometry, apparent stability constants and spectral features of the most stable drug-nanocarrier complexes. In spite of the use of a rough description of the nanocarrier concentration in terms of the average concentration of the complexing units, i.e with disregard of the actual nanostructured organization, the nature of the interactions and the binding modes of the drugs to the 3D host frame could be elucidated. This information represent an important step in the evaluation and further optimization of the examined host systems as potential nanocarriers for drug delivery. In this respect it is important to notice that the spectroscopic characterization of the drug-nanocarrier systems has been carried out in parallel with the investigation of other properties, more closely related to the biomedical applications and performed by other EU-ITN-CYCLON network partners, such as morphology of the drug-loaded nano-objects, encapsulation and release kinetics, biodegradability and stability, cell uploading and intracellular distribution, in vitro activity.

Chapter 6

It has been shown that the water soluble cyclodextrin-based copolymers with epichlohydrin or citric acid crosslinkers are able to bind and monomerize doxorubicin, holding great potential for improved delivery of this drug. Moreover, the results obtained with artemisinin suggest further evaluation of CyD-based polymeric carriers for controlled release and improved bioavailability of artemisinin derivatives, able to contrast the tendency of this class of drugs to be rapidly eliminated from the body. Novel CyD polymers and/or copolymers endowed with suitable nanostructure, for more efficient interaction with anthracyclines and other drugs can be envisaged.

The nanoMOFs with MIL-100 structure, based on iron(III)-trimesate coordination, were shown to possess positive features for loading doxorubicin and phosphorilated nucleoside analogues by formation of strong ionocovalent bonds between the accessible Lewis acid unsaturated iron sites and the negatively charged sites of these drugs, confirming that nanoMOFs may represent an important and novel platform for drug delivery. In the case of doxorubicin further research work is in progress, such as nanoMOF surface modification, study of the degradation mechanism, cellular uptake and in *vivo* activity and pharmacokinetics of drug-loaded nanoMOFs. In the case of the anti-HIV active agents, i.e. the azidothymidine phosphorilated derivatives, the studies are in a more advanced state. New perspectives for HIV treatment can be envisaged, considering that AZT-TP loaded MOF nanoparticles are able to penetrate inside HIV-target cells and to intracellularly deliver the active AZT-TP form, overcoming drawbacks due to drug hydrophilicity, poor stability and low bioavailability (paper accepted for publication in Adv. Healthcare Mat.).

List of Publications

Anand, R.; Ottani, S.; Manoli, F.; Manet, I.; Monti, S. *"A close-up on doxorubicin binding to γ-cyclodextrin: an elucidating spectroscopic, photophysical and conformational study."* **RSC Adv**., 2012, 2, 2346-2357.

Anand, R.; Manoli, F.; Manet, I.; Daoud-Mahammed, S.; Agostoni, V.; Gref, R.; Monti, S. *"β-Cyclodextrin polymer nanoparticles as carriers for doxorubicin and artemisinin: a spectroscopic and photophysical study."* **Photochem.Photobiol.Sci**., 2012, 11, 1285-1292.

Anand, R.; Manoli, F.; Vargas-Berenguel, A.; Monti, S. *"Photocontrolled binding of artemisinin to a bis(b-cyclodextrin) bearing azobenzene on the primary face."* **J.Drug Del.Sci.Tech**., 2012, 22, 266-269.

Agostoni,V.; Chalati,T.; Horcajada, P.; Willaime, H.; Chacun, H.; Baati, T.; Hall, S.; Maurin, G.; Chacun, H.; Bouchemal, K.; Martineau, C.; Taulelle, F.; Couvreur, P.; Roger-Kreuz, C.; Clayette, P.; **Anand, R**.; Monti, S.; Serre, C.; Gref, R.; *"Towards an Improved anti-HIV Activity of NRTI via Metal Organic Framework nanoparticles."* **Adv.Healthcare Mater**. DOI:10.1002/adhm.201200454

Oral Presentation

Anand, R.; Manoli, F.; Ottani, S.; Manet, I.; Agostoni, V.; Gref, R.; Monti, S.; *"Association of doxorubicin to cyclodextrin nanocarriers: a spectroscopic, photophysical and structural study* "**Annual Italian Conference on Photochemistry**, Giardini Naxos (Me) Italy, June 10-12, 2011, *Abstract,* O19.

Poster Presentations

Anand, R.; Ottani, S.; Manoli, F.; Manet, I.; Agostoni, V.; Gref, R.; Monti, S.; *"*Study of Association of doxorubicin monomer and dimer to cyclodextrin nanocarriers by optical spectroscopic techniques and molecular modeling", **2nd European Conference on Cyclodextrins**, Asti (Italy) October 2-4, 2011*, Abstract, VII*-P1

Anand, R.; Manoli, F.; Agostoni, V.; Gref, R.; Monti, S.; "Host-guest interactions between Fe (III)-trimesate MOF and azidothymidine derivatives: a spectroscopic study" **CRS Nordic Chapter: Drug Delivery and Targeting**, Reykjavik (Island), June 3-5, 2012, Abstract P17, *(Best student poster award)*

Anand, R.; Manoli, F.; Manet, I.; Monti, S.; Donzello, M.P.; Viola, E.; Malanga, M.; Fenyvesi, E.; "Study of the association of a water soluble Zn^{II} porphyrazine octacation to fluorescent cyclodextrin derivatives by spectroscopic techniques" **NanoPDT-2013,** Gothenburg (Sweden), April 11-12, 2013. (Accepted for poster presentation)

Anand, R.; Manet, I.; Manoli, F.; Monti, S.; Malanga, M.; Fenyvesi, E.; Maksimenko, A.; Gref, R.; Aykac, A.; Vargas-Berenguel, A.; "Cyclodextrin polymers as carriers for anthracycline drug delivery?" **4th National Conference CD.TE.C,** Giardini-Naxos (Italy), May 8-9, 2013. (Abstract accepted)